INVESTIGATING ON-ORBIT SATELLITE FRAGMENTATION EVENTS
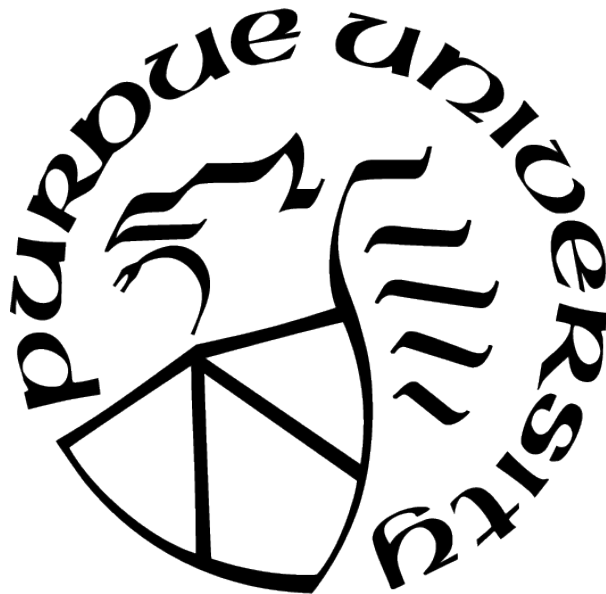
by

Pavithra Ravi

A Thesis

Submitted to the Faculty of Purdue University

In Partial Fulfillment of the Requirements for the degree of

Master of Science in Aeronautics and Astronautics

School of Aeronautics and Astronautics

West Lafayette, Indiana

August 2021

THE PURDUE UNIVERSITY GRADUATE SCHOOL
STATEMENT OF COMMITTEE APPROVAL

Dr. Carolin Frueh, Chair

Purdue School of Aeronautics and Astronautics

Dr. Kathleen Howell

Purdue School of Aeronautics and Astronautics

Dr. Thomas Schildknecht

Astronomical Institute of the University of Bern

Approved by:

Dr. Gregory Blaisdell

This work is dedicated to my parents for their
unconditional love and support through all my endeavors.

ACKNOWLEDGMENTS

First and foremost, I would like to thank my advisor, Prof. Carolin Frueh, for accepting me as a student in her research group and serving as an unforgettable mentor – from patiently equipping me with the background knowledge I needed, to sharing her infectious passion for all things SSA in our meetings, Prof. Frueh truly went above and beyond as an advisor. Her unwavering support and guidance throughout my graduate studies were instrumental in the completion of this thesis. I am grateful to have had the opportunity to grow as a researcher under her tutelage.

Additionally, I would like to thank my advisory committee members, Profs. Kathleen Howell and Thomas Schildknecht, for generously investing their time in both reading this work and attending my defense – their invaluable inputs have made this thesis stronger. This work would not have been possible without observational data from AIUB, courtesy of Prof. Schildknecht. Prof. Howell's Orbit Mechanics course was fundamental in contextualizing concepts in this thesis.

I am deeply grateful to have been funded by the Office of Professional Practice during my graduate studies. It was a pleasure sharing POTR 114 with my delightful coworkers – our conversations always proved to be the most fun study-breaks.

Lastly, I am beyond thankful for my friends at Purdue who have been by my side throughout this process. Our friendships have been an endless source of joy.

TABLE OF CONTENTS

LIST OF TABLES

LIST OF FIGURES

LIST OF SYMBOLS

m mass

v velocity

r position

μ gravitational parameter

a semimajor axis

e eccentricity

i inclination

Ω right ascension of the ascending node

ω argument of perigee

θ true anomaly

γ vernal equinox

ϕ geodedic latitude

λ geodedic longitude

ρ density

A cross-sectional area

C_D drag coefficient

ζ plane-change angle

ABBREVIATIONS

RSO   Resident Space Object

AMR   Area-to-Mass Ratio

18 SPCS   18th Space Control Squadron

RAAN   Right Ascension of the Ascending Node

SSA   Space Situational Awareness

USSTRATCOM   United States Strategic Command

TLE   Two-Line Element

NORAD   North American Aerospace Defense Command

SRP   Solar Radiation Pressure

JD   Julian Date

MJD   Modified Julian Date

ECI   Earth Centered Intertial

ECEF   Earth Centered Earth Fixed

SGP   Simplified General Perturbation

SDP   Simplified Deep Space Perturbations

ABSTRACT

The exponential growth of space debris poses a significant threat to humankind's activities in orbit. It is thus worthwhile to investigate debris-generating events and uncover their causes, consequently informing debris-mitigation guidelines and safer spacecraft design. This work sets out to examine three fragmentation events pertaining to Centaur upper stages which have yet to be fully understood. Critical breakup characteristics such as breakup epoch, fragment velocities, and angular distributions for the Centaur events, as well as select historic fragmentation events are presented. Subsequently, hypotheses regarding the causes of the events are postulated. The Centaur fragmentations stray from breakup patterns exhibited by 'typical' upper stage fragmentations such as those of the historic explosive Delta upper stage events. Only one of the three events, 2018-079B, appears to have fragmented due to the combustion of leftover propellant. 2009-047B, on the other hand, likely endured a structural failure – inferred from clustered fragments and low fragment spreading speeds. A torus-shaped fragment distribution is observed for the 2014-055B event, suggesting a collision with a small piece of debris may have taken place.

1. INTRODUCTION

The proliferation of human-made objects in orbit for scientific, defense, and commercial purposes has resulted in numerous fragmentation events. Since 1961, more than 560 in-orbit fragmentation events have taken place, most of which have been explosions of satellites and upper stages. Coupled with explosions, detonations and collisions have resulted in over 900,000 objects from 1-10 cm and over 34,000 objects larger than 10 cm crowding orbit [1]. This accumulation of debris has a cascading effect; the exponential growth of objects as a result of collisions in orbit was outlined by Kessler and Cour-Palais in [2] and is now termed as the *Kessler Syndrome*. Due to their high velocities (upwards of 7 km/s), debris can have catastrophic impacts on operational satellites and space stations. With the commercialization of space, the proliferation of objects in orbit is imminent, making frequent fragmentation risks a formidable reality. Figure 1.1 summarizes cataloged objects as of 2020 from European Space Agency's *Annual Space Environment Report.*
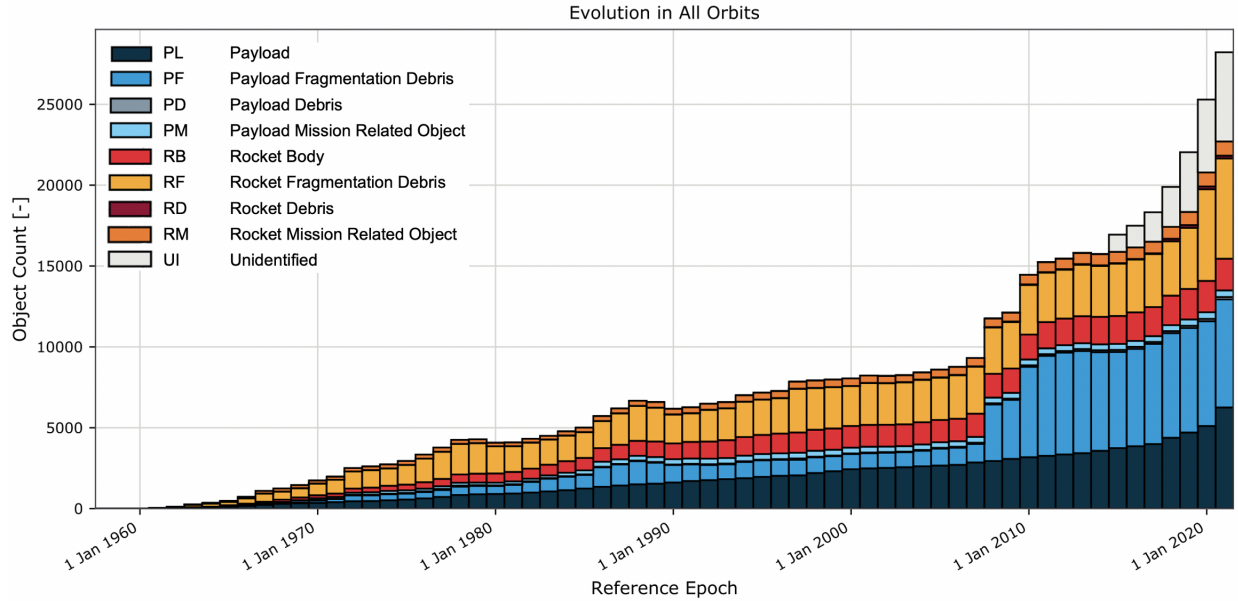
Figure 1.1. Number of cataloged objects in Earth orbit over the years. Image adapted from [3].

Considering the majority of objects in orbit arise from fragmentations, it is worthwhile to investigate what exactly causes them, so actions to mitigate their escalation can be taken. There are two main causes of fragmentation events: explosions and collisions. Explosive

fragmentations comprise three sub-categories: 1. deliberate detonation 2. combustion of leftover propellant (most frequent) 3. battery explosion. Collisions can also be grouped into two broad groups: 1. hypervelocity collision with (uncatalogued) debris or smaller anti-satellite vehicle 2. accidental collision between two satellites (such as the Iridium 33 and Cosmos 2251 event) [4]. These fragmentation events often result in outcomes unique to their causes – the number of fragments generated, their masses, spreading speeds and directions, all vary depending on the event cause. It is thus possible to work backwards and uncover information regarding a breakup by characterizing fragment properties in an event's aftermath. By uncovering breakup characteristics such as these, the cause of an event can be deduced; steps to mitigate such events from occurring can then be taken, securing long-term orbit sustainability for generations to come.

1.1 Developments in Fragmentation Research

A plethora of literature pertaining to the investigation of fragmentation events exists. Earlier works from the late 1980s and 1990s primarily focused on estimating the size, mass, and dispersion of debris clouds. [5] was a pioneering report in this field, which developed analytical models uncovering the shape, volume, and spacial density of debris clouds. Equations to determine masses, velocities, and orbital parameters of fragments, along with the risks they posed to Resident Space Objects (RSOs) were also put forth. These models were used for the subsequent development of DEBRIS (a computer program developed by The Aerospace Corporation) to assess the collision hazard posed by debris clouds on orbiting spacecraft. Along the tangent of estimating the number of fragments that would arise from an event, [6], outlined the effect of energy (both residual in the form of batteries or propellant, and kinetic) on debris generation for different orbital regimes. [7] determined the Area-to-Mass Ratio (AMR) for a collection of fragments using changes in their orbital elements due to atmospheric drag over time. [8] provided insight into the evolution of debris clouds — specifically outlining 'phases' debris clouds go through from an ellipse, spreading into a torus, and ultimately dispersing into a band enveloping a significant portion of orbit.

A more recent work (2019) [9] developed a measure which assessed the degree to which spreading speeds of fragments could be inferred from the spatial density of a debris cloud.

Current works have been dedicated to uncovering specific breakup characteristics, such as identification of the breakup epoch and parent object. [10] illustrated the work done by the 18th Space Control Squadron (18 SPCS) of the U.S. Strategic Command in predicting propulsion-based breakups through the detection of outgassing. The 18 SPCS' methods for sensor tasking, and correlating orbits of fragments to identify objects were also outlined. Techniques used to determine the breakup epoch, location, and parent object were discussed; the breakup time is found using conjunction assessment softwares such as SuperCOMBO (which employs Special Perturbations predictive modeling). The parent object is identified by comparing the ballistic coefficient and radiation pressure perturbations of candidate parent objects to the debris. [11] is another work which provided valuable insight into breakup epoch determination and part object identification — the effectiveness of different distance functions (to calculate inter-object distances, which would be minimized at the breakup point) in attaining the breakup time were compared. In contrast to [10], the parent object is identified by essentially sifting through the public space debris catalog to discern an object near the fragments at the breakup epoch. This paper is used as a key reference in the breakup epoch determination due to its ease of replicability (no external softwares are needed). Another technique for identifying the parent object was outlined in [12], using the PUZZLE software developed at Politecnico di Milano. Fragmentations are characterized by analyzing the evolution of osculating orbital elements of a set of objects and using clustering algorithms to identify which cataloged events were involved; information regarding the breakup epoch and subsequent dispersion of fragments is then obtained using propagation models.

Several works have also attempted to determine the causes of various fragmentation events through the study of multiple breakup characteristics including breakup time and location, Area-to-Mass Ratio (AMR) of the fragments, fragment spreading speeds and directions, and event energy. [13] outlined The Aerospace Corporation's method of determining

key breakup parameters within 12 hours following a breakup event. Subsequently models are used to determine the risk stemming from the debris on other resident satellites. The method used to obtain the breakup epoch is similar to that employed by [11], [14] and [15], where orbits of the fragments are back propagated to an epoch when they are at their closest. Additional parameters such as the state vector and mass of the fragmenting object, and the event energy are computed – these are fed to the IMPACT model which calculates the mass, size, and velocity distributions of the fragments. Based on the spreading speeds of the fragments and the event energy (coupled with factors such as the presence of another cataloged object in the vicinity of the event), causes are postulated for test cases. Two other works by The Aerospace Corporation, [15] and [16], also offer insight into how fragments and events can be characterized by calculating fragment spreading speeds, AMR and mass distributions, from which information on the breakup time and location, as well as the event energy can be obtained. A software called Collision Vision is used to find the breakup epoch; a method of comparing slowly varying orbital elements is used to develop the velocity perturbations on the fragments. In [14], the Hitomi (Astro-H) fragmentation event was studied in detail – breakup epoch, location, energy was calculated and conjunction analysis was carried out to determine the cause of the event. The NASA EVOLVE-4 breakup model, which simulates fragmentation events and the debris environment, was used to assess possible collision outcomes. A similar breakup model developed by ESA, is the MASTER (Meteoroid And Space debris Terrestrial Environment Reference) model. MASTER serves to model the near-Earth environment by simulating all known debris-generating events in space. This population snapshot is vital for mission design; the risk a satellite would face in a particular orbit can be promptly assessed and long-term environment evolution can be studied [17].

The most comprehensive work in fragmentation theory is *Theory of Satellite Fragmentation in Orbit* by Tan and Reynolds (2020) [4], and serves as a primary reference for this paper; this is the first book of its kind on satellite fragmentation in which the physical processes that occur during fragmentation events are examined, and theoretical relationships to compute velocity and directional perturbations on fragments are presented. These are applied to an array of fragmentation events ranging from the Delta upper stage explosive

events, to collisions such as that of Iridium 33 and Cosmos 2251. Many examples in this book were implemented using publicly available datasets, making it possible to replicate results and validate algorithms developed in the scope of this research.

Additionally, ground-based experimental methods to characterize fragmentation events have taken place – these include both hyper-velocity impact studies [18] [19] as well as pressurized-to-failure explosive propellant tank tests [20]. In these studies, the number and distribution of fragments arising from fragmentation events are experimentally simulated – results from which are beneficial in the development of breakup modeling software as well as in understanding how an event may have unfolded based on the observed debris distribution in the controlled environment.

1.2 Thesis Scope and Outline

This thesis focuses on determining key breakup characteristics – breakup epoch, fragment spreading speeds and angular distributions, event intensity – to subsequently hypothesize the cause of an event. Chapters 2 and 3 provide the necessary background and orbital theory foundations needed to situate the context of the space debris environment. Chapter 4 outlines the fragmentation theory used to obtain the breakup characteristics of interest. The methodology is validated with well-studied events such as the upper stages pertaining to the NOAA-3 and Spot-1 satellites, in Chapter 5. In Chapter 6, the validated techniques are used to investigate three Centaur upper stage fragmentation events (2009-047B, 2014-055B, 2018-079B) which took place in 2018 and 2019. At the time of writing, there is no consensus on the causes of these events. Akin to collecting an array of clues to solve a case, this research aims to uncover pertinent information surrounding the breakups to ultimately postulate their causes. Chapter 7 summarizes the conclusions derived from this thesis and puts forth recommendations and future trajectories this research could take.

2. BACKGROUND

2.1 Two-Body Problem

The two-body problem refers to the classical problem of determining the motion of two bodies due solely to their own mutual gravitational attraction [21]. It is a specific case of the *N*-body problem, which encapsulates the motion of *N* particles of interest. The two-body formulation of this problem is the only case which has a complete solution and is thus fundamental in understanding orbit mechanics.

Figure 2.1 shows two point masses relative to an inertial frame of reference with origin, O. This frame does not rotate but may move with constant velocity. The only forces present are gravitational – these act along a line connecting the centers of the two objects. The bodies can be treated as point masses under the assumption that they are spherically symmetric with uniform densities.
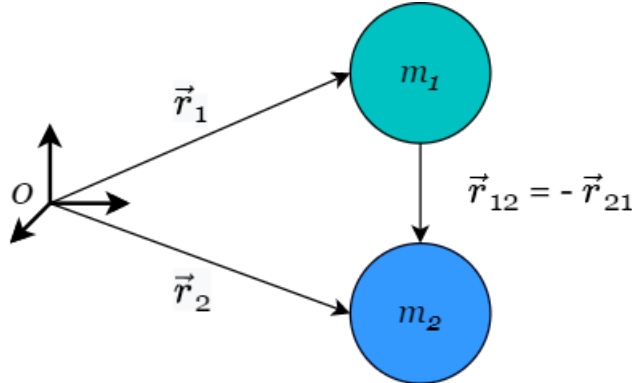
Figure 2.1. Two point masses in an inertial coordinate frame with origin, *O*.

Newton's Universal Law of Gravitation provides the basis for modeling orbital motion. It states that any two point masses attract one another with a force proportional to the product of their masses and inversely proportional to the square of the distance between them [22]. This is expressed mathematically in Equation 2.1, which denotes the force exerted on particle 2 by particle 1.

$$\vec{F}_1 = -G\frac{m_1 m_2}{r_{1,2}^2}\hat{r}_{1,2} = -G\frac{m_1 m_2}{r_{1,2}^3}(\vec{r}_2 - \vec{r}_1) \tag{2.1}$$

In combination with Newton's Second Law, the inertial force due to gravitation of particle 1 on particle 2 is given by Equation 2.2 and the force due to gravitation of particle 2 on particle 1 is given by Equation 2.3.

$$\vec{F_1} = m_1\ddot{\vec{r_1}} = -G\frac{m_2 m_1}{r_{2,1}^3}(\vec{r_1} - \vec{r_2}) \tag{2.2}$$

$$\vec{F_2} = m_2\ddot{\vec{r_2}} = -G\frac{m_1 m_2}{r_{1,2}^3}(\vec{r_2} - \vec{r_1}) \tag{2.3}$$

Since the forces act along the same line, with equivalent magnitudes and in opposite directions, they negate each other as shown in Equation 2.4.

$$m_1\ddot{\vec{r_1}} + m_2\ddot{\vec{r_2}} = 0 \tag{2.4}$$

It can be concluded that the center of mass of the two particles does not indeed accelerate and the origin of the inertial frame of reference can be ascribed to this location.

Equations 2.2 and 2.3 can be rewritten by representing each particle's position relative to the center of of mass.

$$\ddot{\vec{r_1}} = -G\frac{m_1 + m_2}{r_{2,1}^3}\vec{r_1} \tag{2.5}$$

$$\ddot{\vec{r_2}} = -G\frac{m_1 + m_2}{r_{1,2}^3}\vec{r_2} \tag{2.6}$$

Subtracting Equation 2.5 from Equation 2.6, the relative acceleration between the two particles can be found as shown in Equation 2.8.

$$\ddot{\vec{r}} = -G\frac{(m_1 + m_2)}{r_{1,2}^3}(\vec{r_2} - \vec{r_1}) \tag{2.7}$$

Simplifying, the relative equation of motion for the two-body problem is defined as,

$$\ddot{\vec{r}} = -\frac{\mu}{r^3}\vec{r} \tag{2.8}$$

where μ is the gravitational constant, $\mu = G(m_1 + m_2)$, and $\vec{r}$ is the relative position vector, $\vec{r} = \vec{r_2} - \vec{r_1}$.

A second order vector differential equation of this type can be solved by computing six integrals. These result in the six orbital elements that are used to define Keplerian motion and are described in the following section.

2.2 Orbital Elements

There are two sets of quantities that completely specify a two-body orbit. The first of these is a state vector, typically associated with position and velocity vectors. State vectors are defined with respect to a specific coordinate frame. Coordinate frames will be discussed in more detail in Section 3.3. Alternatively, six quantities comprising scalar magnitude and angular representations, called orbital elements, can be defined [22]. While a variety of orbital elements which provide information pertaining to an orbit can be defined, this section will focus on the six classical Keplerian orbital elements.

The six classical orbital elements are listed below:

- semimajor axis, a : portrays the size of the orbit

- eccentricity, e : denotes the shape of the orbit

- inclination, i : refers to the tilt of the orbit plane

- right ascension of the ascending node (RAAN), Ω : orients the orbit with respect to the vernal equinox, γ (defined in Section 3.3.1).

- argument of perigee, ω: indicates the orientation of the perigee relative to the ascending node (both defined below)

- true anomaly, θ: denotes the orbiting object's position relative to its perigee

These orbital elements are visually depicted in Figure 2.2, which shows a satellite orbiting the Earth in the geocentric equatorial frame.

The perigee refers to the closest approach of the orbiting object relative to the origin. Conversely, the apogee is the point along the orbit that is furthest from the origin (not
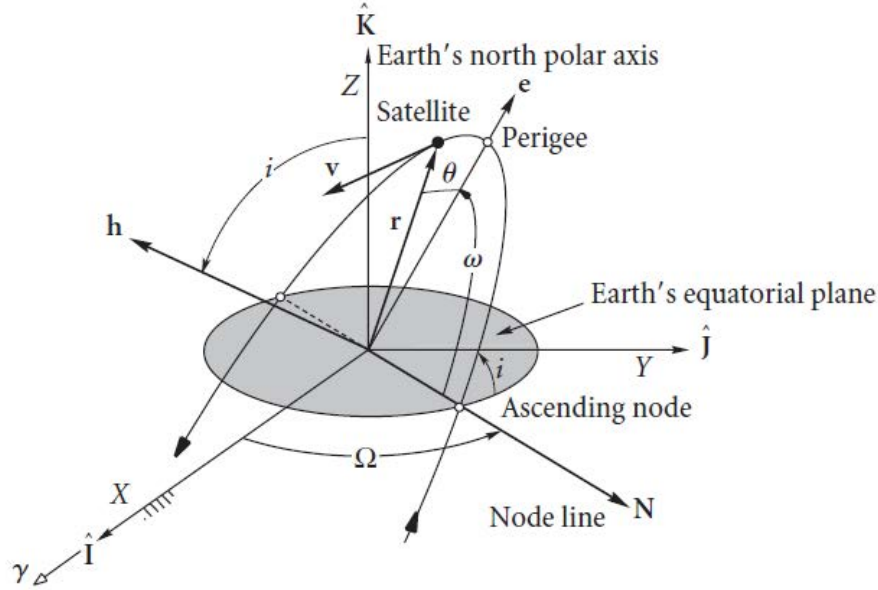
Figure 2.2. Three dimensional orbit indicating orbital elements in the geocentric equatorial frame [21].

shown). The node line emerges from the intersection of the equatorial plane of the attracting object and the orbit plane of the orbiting object. The ascending node is the location at which the orbiting object passes above the equatorial plane, while the descending node is the location at which this object descends beneath the equatorial plane. The vector, **h**, denotes the angular momentum vector of the orbit and lies perpendicular to the orbit plane.

2.3 SSA Catalogs

This section covers the sources of Space Situational Awareness (SSA) data that are relevant to this research. Two catalogs maintained by the US and Russia are described. Additionally, SSA information for this research was also provided by the Astronomical Institute at the University of Bern (AIUB), the specifics of which are discussed in Section 6.2.

2.3.1 USSTRATCOM Catalog

The 18th Space Control Squadron, which is a part of the United States Strategic Command (USSTRATCOM) detects, tracks, and identifies human-made objects in orbit. Obser-

vational data is obtained from the Space Surveillance Network (SSN), which is a network of sensors located at two dozen sites worldwide and operated by US Army, Navy, and Air Force personnel [23]. Over 23,000 objects are tracked – objects that are unclassified are listed on the publicly available Spacetrack catalog (www.Space-Track.org) [24]. Data maintained in this catalog is in the two-line element format (TLE).

The North American Aerospace Defense Command (NORAD) put forth the 'TLE' format to store key satellite orbit parameters – it consists of two lines, each containing 69 characters. TLEs can be propagated using orbital models such as the Simplified General Perturbations (SGP) model and the Simplified Deep Space Perturbations (SDP) model. It is important to note that TLEs are mean elements in the True Equator Mean Equinox (TEME) of epoch frame. Additional information on how to propagate TLEs is covered in Section 3.4. Figure 2.3 shows a sample TLE for the NOAA-6 satellite. Its entries are briefly described as follows [25]:

- Name: This is the alphabetic identifier of the object – it is included in the '3LE' or three-line element format.

- International Designator: The first two digits of this term refer to the last two digits of the launch year. The following three digits pertain to the launch number of the object (NOAA 6, for instance, appears to be the 123rd object launched in 1984). The alphabet term refers to the piece of launch – a payload might be 'A', while an upper stage might be 'B', and so on.

- Epoch: This entry contains two terms and pertains the time to which the time-varying fields in the TLE are referenced. The first term is the last two digits of the year. The second term is the day of the year (includes fractional component).

- 1st and 2nd Derivatives of Mean Motion: These two fields provide an insight into how the mean motion changes with time.

- Drag term (BSTAR): This term provides an indication of how susceptible the object is to drag — a higher number point to a larger drag effect.

- Ephemeris Type: This entry represents the orbital model used to generate the data. It is only for internal analysis – distributed sets generally have a value of 0.

- Element Number, Check Sum: The first three digits pertain to the number of element sets generated for the object. Sometimes the sets are not properly synced, resulting in inaccuracies in this field. The last digit is used to ensure there are no errors in the line – it is the last digit of the sum of all the numbers in the line (plus signs and periods are ignored, but minus signs are assigned a value of 1).

- Satellite Number: This is a unique numeric identifier assigned to each object by NORAD. 'U' in Line 1 indicates that the object is unclassified.

- Orbital elements: Inclination (degrees), Right Ascension of the Ascending Node (degrees), Eccentricity (leading decimal point is omitted), Argument of Perigee (degrees), Mean Anomaly (degrees).

- Mean Motion: Revolutions completed by the object in 24 hours.

- Revolution Number, Check Sum: The first five digits pertain to the number of revolutions completed by the object since its launch till the current epoch. The last digit used to check for errors, akin to the Check Sum digit in Line 1.
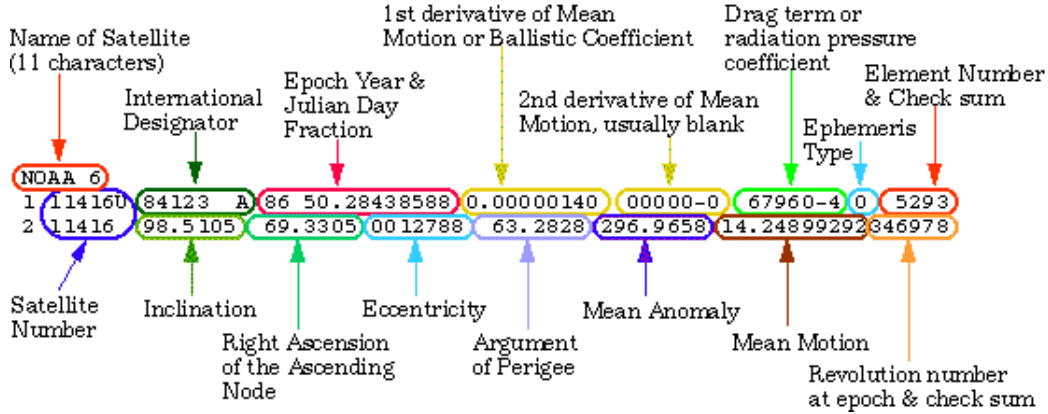
Figure 2.3. Sample TLE of the NOAA 6 satellite [26].

TLEs do not contain any publicly available covariance. While it is possible to estimate these uncertainties using models, this is beyond this scope of this work.

2.3.2 Vimpel Catalog

This section draws on [27]. The JSC Vimpel Interstate Corporation and Keldysh Institute of Applied Mathematics based in Russia maintain the 'Vimpel catalog', which records orbit parameters of space debris objects in Highly Elliptical Orbits (HEO). The catalog mainly documents orbits with a period of over 200 minutes, mostly comprising geostationary space debris and objects with large eccentric orbits. Unlike the US catalog, the Vimpel catalog does not store information in TLEs – ephemeris information, which includes 15 parameters, is instead provided for each object. This contains: reference epoch of orbital parameters, semimajor axis, inclination, eccentricity, right ascension of the ascending node, argument of latitude, argument of perigee, average effective area to mass ratio, and apparent magnitude. Two uncertainty values – one each for time (up to 100 minutes) and position (up to 1000 km) – are also provided, though these are not accounted for in the propagation model used in this thesis. Ephemeris data for each object is generally issued each week on the Vimpel catalog – TLEs, on the other hand, are often less frequently updated and can sometimes be many months old.

The orbital parameters catalogued by Vimpel are osculating Keplerian elements (unlike mean elements in TLEs) in the inertial coordinate system referred to the epoch J2000 (Section 3.3.1). These orbital parameters are obtained using a numerical model which takes into account the Earth's gravitational perturbations (geopotential harmonics up to the eighth inclusive), third body effects due to the Sun and the Moon (using the DE-405 model), solar radiation pressure, and atmospheric drag (GOST R 25645.166-2004). Perturbations are further discussed in Section 3.1.

3. ORBITAL THEORY

3.1 Orbital Perturbations

While the two-body model is convenient to implement and broadly considers the scope of the problem, it is an oversimplification. After all, the Earth and other bodies in space are not perfectly spherical in nature, with uniform densities – the point mass assumption is thus far from accurate. Third body effects, such as those due to the Sun's and the Moon's gravity must also be accounted for, along with atmospheric drag and effects such as solar radiation pressure. This section defines each of these perturbations and highlights how they are accounted for in the scope of this thesis.

3.1.1 Earth Gravity

Since the Earth is not a perfect sphere, but rather a Geoid, its gravitational potential needs to be modeled accordingly. Typically, this is done using surface spherical harmonics which are the trigonometric argument of the Legendre polynomials shown below [22]:

$$U = \frac{\mu}{r}[1 + \sum_{l=2}^{\infty} \sum_{m=0}^{l} (\frac{R_E}{r})^l P_{l,m}[\sin{(\phi_{gc,sat})}] \{C_{l,m} \cos{(m\lambda_{sat})} + S_{l,m} \sin{(m\lambda_{sat})}\}] \qquad (3.1)$$

The terms in Equation 3.1 are defined as follows:

- μ : gravitational constant of the attracting body (i.e. Earth in this case)

- r : distance between the origin and the location at which the potential is determined

- $P_{l,m}$: Legendre polynomials with degree, l, and order, m

- R_E : Earth's mean radius

- $\phi_{gc,sat}$, $\lambda_{gc,sat}$: geocentric latitude and longitude of orbiting object

- $C_{l,m}$, $S_{l,m}$: gravitational coefficients

The spherical harmonics can be broadly divided into three sub-categories: 1. Zonal harmonics ($m = 0$), 2. Sectoral harmonics ($l = m$), and 3. Tesseral harmonics ($l \neq m \neq$

28

0). The J-notation, such that $-C_{l,0} = J_l$, can be used for the zonal harmonics. The zonal harmonic term associated with J_2 is almost 1000 times larger than the other coefficients and corresponds to the Earth's oblateness. For this research, a formulation of Equation 3.1 using normalized spherical harmonics mass coefficients was initially used to generate the (2,0), (2,2), (3,0), (3,1), (4,0) terms. This resulted in infeasible computation times for the long propagation periods needed for this research. As a result, only the J_2 term, (2,0), is used to generate the results seen in this thesis; the difference in output between using five terms versus only the oblateness proves to be insignificant for the scope of this work.

3.1.2 Third Body

In addition to the gravitational effects of the Earth, it is also important to consider perturbations arising from the gravity of the Sun and the Moon. Since this thesis is concerned with objects in the near-Earth regime, the Sun and the Moon are modeled as point masses. From Newton's Second Law (as covered in Section 2.1), the accelerations on a satellite due to n number of bodies can be written as,

$$m_{sat}\ddot{\vec{r}}_{sat} = -G\sum_{i=1}^{n}\frac{m_{sat}m_{i}}{r_{i,sat}^3}\vec{r}_{i,sat} \tag{3.2}$$

It is useful to express the acceleration of the satellite relative to the Earth as shown in Equation 3.3, where the subscripts E, S, and M pertain to the Earth, Sun, and Moon respectively.

$$\ddot{\vec{r}}_{E,sat} = -G\frac{m_E + m_{sat}}{r_{E,sat}^3}\vec{r}_{E,sat} + Gm_S\left(\frac{\vec{r}_{sat,S}}{r_{sat,S}^3} - \frac{\vec{r}_{E,S}}{r_{E,S}^3}\right) + Gm_M\left(\frac{\vec{r}_{sat,M}}{r_{sat,M}^3} - \frac{\vec{r}_{E,M}}{r_{E,M}^3}\right) \tag{3.3}$$

The first term on the right side of the equation pertains to the point mass gravitational acceleration of the Earth. The other two terms correspond to the third body acceleration effects due to the Sun and the Moon. Thus, the net perturbing acceleration on the satellite due to third body effects can be simplified to,

$$a_{\text{Third Body}} = -\mu_S\left(\frac{\vec{r}_{sat,S}}{r_{sat,S}^3} - \frac{\vec{r}_S}{r_S^3}\right) - \mu_M\left(\frac{\vec{r}_{sat,M}}{r_{sat,M}^3} - \frac{\vec{r}_M}{r_M^3}\right) \tag{3.4}$$

The mass of the satellite is considered to be negligible relative to the masses of the other bodies and is omitted from calculations in this work.

Gravitational forces (both form the Earth and third body effects) are conservative in nature – they do not modify the energy of the system. Non-conservative forces, such as atmospheric drag and solar radiation pressures also act on Earth-orbiting objects – these depend on the physical characteristics of the object, such as its effective surface area, mass, and attitude. These perturbations are discussed in the following two subsections.

3.1.3 Atmospheric Drag

This section primarily references [28]. The dense atmosphere of the Earth naturally affects the acceleration of objects that pass through it. This drag force tends to be the largest non-gravitational perturbation acting on low altitude satellites. Equation 3.5 shows the acceleration on a satellite due to drag.

$$a_{\text{Drag}} = -\frac{1}{2}C_D\frac{A}{m}\rho v^2\hat{v} \tag{3.5}$$

C_D is the drag coefficient (dimensionless, with values typically ranging from 1.5-3), A is the satellite's cross-sectional area that is in contact with the atmosphere column, m is the satellite's mass, ρ is the atmospheric density, v is the velocity of the satellite relative to the atmosphere, and $\hat{v}$ specifies the velocity direction relative to the atmosphere. A canon ball model is assumed. For this research, a value of 2 is chosen for the drag coefficient (assuming a spherical satellite). The density is estimated using standard atmosphere models – the US Standard Atmosphere 1976 model is used for altitudes ranging 86-1000 kilometers. For altitudes below 86 kilometers, the ARDC Model Atmosphere, 1959, is used.

3.1.4 Solar Radiation Pressure

Solar Radiation Pressure (SRP) is a non-conservative perturbation arising from the absorption or reflection of photons [28]. The SRP experienced by a satellite using the cannon ball model, which is assumed in this research, can be calculated using Equation 3.6 [29].

$$a_{\mathrm{SRP}} = -\frac{A}{m}\frac{E}{c}\frac{\mathrm{AU}^2}{r_S^2}\left(\frac{1}{4} + \frac{1}{9}C_d\right)\frac{\vec{r}_S}{r_S} \tag{3.6}$$

Here, A/m is the area-to-mass ratio (AMR) of the satellite, E is the solar constant at Earth's surface, c is the speed of light, AU is the astronomical unit, r_S is the position vector from the Sun to the satellite, and C_d is the coefficient of diffuse reflection, which depends on the surface material.

3.2 Time

This section draws on [29]. The passage of time on Earth is generally marked by its rotational period as it revolves around the Sun – that is, the 'solar day' of 24 hours or 86,400 seconds is how humans organize their activities and track 'daily' flow of time. However, the rotational period of the Earth is not perfectly equal to a solar day – the Sun's right ascension changes by about one degree each day, resulting in the solar day lasting roughly four minutes longer than the Earth's rotational period, which is actually about 23 hours and 56 minutes. This rotational period is regarded a 'sidereal day' and is the time between successive meridian passages of the vernal equinox. Other factors such as the shift in the apparent vernal equinox due to precession, Earth's elliptical orbit around the Sun, and the slowing of the Earth's rotation (due to friction from tidal motion) also affect the Earth's motion, which inevitably affect time calculations which depend on Earth's rotation and revolution about the Sun. Additionally, the clock used to measure this time would also have to account for relativistic effects due to gravity and speed.

As a result, it is helpful to define time scales with specified units and references: Terrestrial Time (TT) is a conceptually uniform time scale that is used as the independent argument of geocentric ephemerides – a TT day is 86,400 SI seconds. International Atomic time (IAT) is in accordance with TT but has an offset of 32.184 seconds and also accounts for the imperfections of existing clocks. Universal Time (UT1) is a modified version of the solar time scale that is defined by the mean Sun – UT1 accounts for corrected polar movement and short periodic tidal effects.

Coordinated Universal Time (UTC) is related to TAI by an offset of integer seconds, which are regularly updated to keep UTC in close agreement with UT1.

Finally, it is also important to define the Julian date, JD, which corresponds to the number of days that have passed since January 1, 4713 BC at 12:00. It is common to use the Modified Julian Date (MJD) for simplicity,

$$MJD = JD - 2400000.5 \qquad (3.7)$$

JD and MJD are often used to define epochs for orbit propagation.

3.3   Coordinate Systems

In addition to using standard time formats, it is also helpful to define coordinate systems – these establish the reference frame for a satellite's orbital elements or state vector.

A coordinate system is governed by the following quantities [29]:

- origin

- fundamental plane

- reference direction

- handedness (right/left)

- Cartesian or non-Cartesian (spherical/cylindrical)

Coordinate systems can be inertial (space fixed) in nature, such as the Earth Centered Inertial (ECI) frame, or affixed to a body, as in the case of the Earth Centered Earth Fixed (ECEF) frame. The latter is not covered in this section as it is not used in the scope of this thesis. Additionally, it is beneficial to define a coordinate system in the local reference plane of an orbiting satellite (such as the RSW frame, defined later in this section).

3.3.1 Earth Centered Inertial (ECI) frame, J2000

This reference frame is geocentric, with the origin located at the Earth's center, and is fixed in space. The fundamental plane is marked by the Earth's equator, with the x axis pointed in the direction of the mean vernal equinox – this is the point at which the ecliptic plane and the equatorial plane intersect. It is important to note that the direction towards the vernal equinox changes over time due to effects such as precession. Precession describes the secular change in the orientation of the Earth's rotation axis and the equinox. These variations are caused by the gravitational effects due to other bodies, such as the Sun and the Moon, and result in a torque on the Earth's rotational axis; consequently, Earth's rotational axis traces a circle every 26,000 years. This results in the slow recession of the vernal equinox towards the ecliptic [29]. Another torque acting on the Earth's rotational axis is nutation, which is the periodic and short-term variation of the equator and the vernal equinox due to solar and lunar torques. Additionally, a perturbing effect arises from polar motion – this is the movement of the rotational axis of the Earth, relative to its crust.

Due to the constantly changing torques and forces acting on the Earth, it is beneficial to define a standard, or reference epoch. J2000, which is JD 2451545 (noon at January 1 2000) is used for this research. The International Earth Rotation and Reference System Service (IERS) maintains the International Celestial Reference System (ICRS) and the International Terrestrial Reference System (ITRS). ICRS is closely aligned with the mean equator at J2000 and can be considered a precise realization of an ECI system. ITRS is an Earth Centered Earth Fixed reference system and exhibits no net rotation relative to the Earth's crust – it can be considered a precise realization of an ECEF system [29].

It must be noted that J2000 refers to the Mean Equator Mean Equinox frame. Output from orbit propagators used in this research use the True Equator Mean Equinox of epoch – that is, the x axis points toward the mean vernal equinox at the current epoch, while the z axis points towards the instantaneous North Pole.

Figure 3.1 depicts the ECI frame. The z axis is oriented towards the Earth's North Pole.
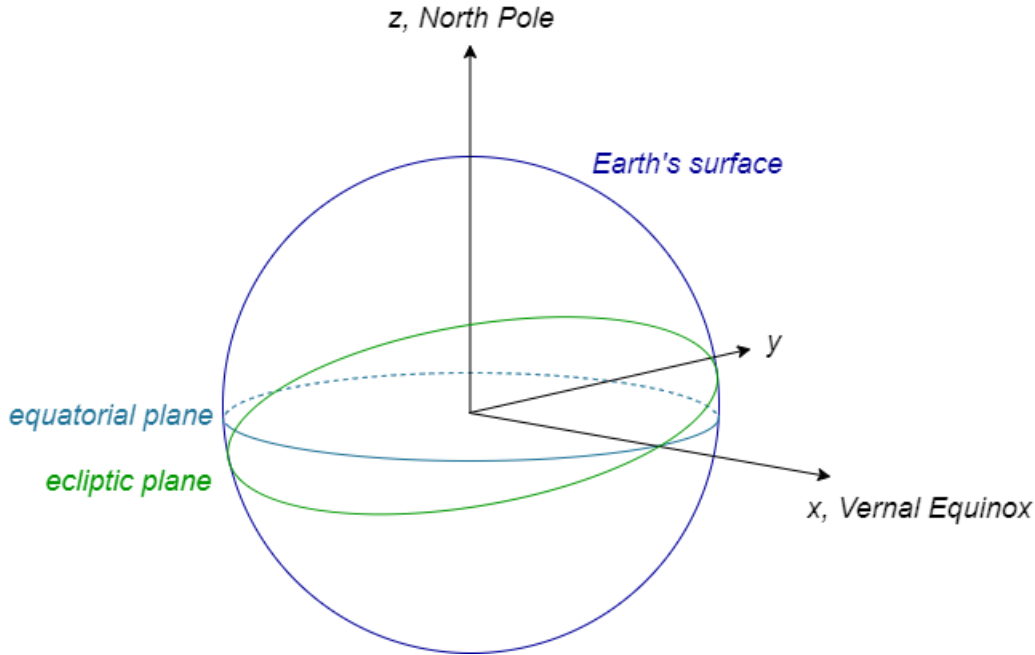
Figure 3.1. Earth Centered Inertial (ECI) reference frame – both the x and y axes lie on the equatorial plane, while the z axis is orthogonal to it.

3.3.2 Satellite-centered RSW frame

This is a satellite coordinate system that is specifically applied to studies of relative motion [22]. This system is in the frame of reference of the satellite and thus moves with it. Radial positions and displacements lie along the R axis; this is parallel to the position vector of the satellite. Along-track displacements are in the direction of the S axis, which is orthogonal to the position vector and in the same orbit plane. Cross-track or out-of-plane displacements are normal to the orbit plane and lie along the W axis. It is important to note that the along-track direction is not the same as the in-track direction, which is parallel to the velocity vector. Figure 3.2 shows the RSW reference frame.

3.4 Propagating Two-Line Elements

When investigating breakups, it is naturally necessary to obtain the state (position, velocity, orbital elements) information of a parent satellite or its fragments at the breakup time. This is done by propagating the state vector to obtain orbital elements and other pertinent
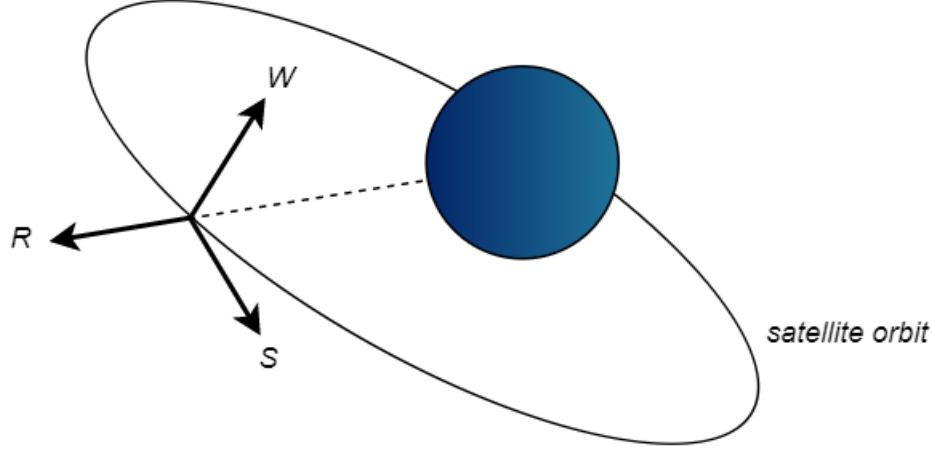
Figure 3.2. Satellite coordinate system (RSW) – the R and S axes lie parallel to the orbit plane, while the W axis lies perpendicular to it.

information at a specified, desired epoch. Two main data types are used in this research – TLEs and ephemerides (as covered in Section 2.3.) – and require separate propagation methods.

It is important to note that TLEs are mean elements and have been truncated. Unlike osculating elements, which are instantaneous elements for a satellite under the influence of perturbations, mean elements result from averaging the effect of perturbations over a specific time interval [22]. In order to be propagated, it is essential to reconstruct the periodic variations and the perturbations that have been removed from TLEs. This is done using the orbital models such as the Simplified General Perturbations (SGP) model for near-Earth objects or the Simplified Deep Space Perturbations (SDP) for deep-space objects. SGP4 accounts for atmospheric drag effects using the 'B star' term, the secular effects of the Earth's zonal harmonics, third body effects from the Sun and the Moon, along with resonance effects of Earth's gravity [30] [31]. This work uses an SGP4 routine written by Vallado (2006) – SGP4 was originally developed in 1970 by Lane and Crawford. The Cartesian output of the SGP4 model is in Earth-Centered Intertial (ECI) coordinates and is True Equator Mean

Equinox (TEME) of epoch. The x axis is in the mean direction of the current vernal equinox (not J2000), and the z axis is aligned with the Earth's instantaneous North Pole as was shown in Figure 3.1. It must be noted that SGP4 is a semi-analytic propagator. In analytic propagators, analytical expressions are used in place of the equations of motion to approximate the motion of a satellite over time [22]. This results in quick run times, albeit less accurate propagated states. Numerical propagators numerically integrate the equations of motion for a satellite. This results in longer run times, but yields more accurate results in comparison to analytic or semi-analytic propagators such. Semi-analytic propagators incorporate both analytical and numerical techniques – typically, secular and long-period components of motion are solved analytically, while short-period components of motions are computed through numerical integration.

Ephemerides (such as state information in the Vimpel catalog) can be propagated directly, since they are osculating elements and not means. For this research, a numerical propagator, which accounts for the perturbations mentioned in Section 3.1 is used to obtain state information regarding objects at desired epochs; it must be noted that the models used for this research are not the same as those used by the Vimpel corporation.

Additionally, in the case of TLEs, SGP4 adds perturbations (using different models than what is used in the numerical propagator) to mean elements, while the initial state of the Vimpel ephemeris data is in the form of osculating elements. These discrepancies naturally result in slightly different propagated states for the same object – it is important to acknowledge this as a possible source of error when comparisons are being made across different data sources and propagators. The discrepancies that arise in propagating the same initial state, for both a week and a month, between SGP4 and the developed numerical propagator are summarized in Table 3.1. Results from GMAT (NASA's General Mission Analysis Tool), which also uses a numerical propagator, are provided as reference. The numerical propagators are largely in alignment (despite using different perturbation models), and are more accurate. The analytical methods used by SGP4 result in noticeably different outcomes.

While this research does not factor in state uncertainties, the effects they may have on the results are discussed in Section 6.10.

Table 3.1. Comparison of propagated states using numerical propagators and SGP4

	SGP4	Numerical	Numerical-GMAT
r_x (km), 1 week	-10296.0027	-10356.6336	-10376.1516
r_y (km), 1 week	-24923.8955	-24847.7373	-24837.3116
r_z (km), 1 week	-3373.0024	-3381.9842	-3386.3637
v_x (km/s), 1 week	2.4149	2.4099	2.4084
v_y (km/s), 1 week	-3.0400	-3.0524	-3.0538
v_z (km/s), 1 week	0.3463	0.3447	0.3445
r_x (km), 1 month	14821.3798	14556.9468	14559.7752
r_y (km), 1 month	-35952.9279	-35978.5845	-35978.1398
r_z (km), 1 month	1559.1368	1502.5922	1506.2561
v_x (km/s), 1 month	2.4545	2.4649	2.4648
v_y (km/s), 1 month	0.2225	0.1963	0.1967
v_z (km/s), 1 month	0.5187	0.5197	0.5197

4. FRAGMENTATION THEORY

4.1 Breakup Epoch Calculation

One of the first steps in investigating any fragmentation event is determining the time of breakup and the parent object, if it is not already known. The breakup epoch provides crucial insight into where along its orbit the object was when it fragmented – the position and velocity of the parent object can then be determined. From this, the velocities imparted on the fragments and their angular distributions can be calculated. Thus, since the breakup epoch affects the calculation of subsequent relevant quantities surrounding the event, it is imperative that the breakup time is as accurate as possible.

The breakup epoch is found by back propagating the orbits of the fragments to a point in time when the fragments would have been at a single location – however, considering errors that accumulate during the propagation process result in less-than perfectly accurate states, it is generally acceptable to simply minimize the distances between the fragments, since a true convergence is unlikely to occur.

4.1.1 Distance Functions

There are multiple distance functions that can be used for the purpose of determining the breakup epoch. In essence, there are three main distances that can be computed: orbital distances (D-criteria), nodal distance, and linear distance.

D-Criteria

This section draws on reference [11]. The concept of a 'D-criterion' to determine non-dimensional orbital distances was first put forth by Southworth and Hawkins in 1963 to identify meteor streams [32]. Drummond [33] and Jopek [34] introduced similar formulations, modifying [32]. These D-criteria were applied for the identification of asteroid families and have subsequently found applications in the study of Earth-orbiting objects. All three formulations of the D-criteria are functions of five Keplerian orbital elements: semimajor axis

(a), eccentricity (e), inclination (i), right ascension of the ascending node (Ω), and argument of perigee (ω). q denotes the perigee, $q = a(1 - e)$.

The classical D-Criterion of Southworth and Hawkins, D_{SH} is shown in Equation 4.1.

$$D_{SH}^2 = (e_B - e_A)^2 + \frac{(q_B - q_A)^2}{R_E^2} + (2\sin{(\frac{I_{BA}}{2})})^2 + (\frac{e_B + e_A}{2})^2(2\sin{(\frac{\pi_{BA}}{2})})^2 \tag{4.1}$$

Here, the subscripts A and B refer to the indices of the two fragments being compared. R_E is the radius of the Earth. 'e' refers to the magnitude of the Laplace-Runge-Lenz vector (referred to as the Laplace-Lenz vector in [11]) and is defined in Equation 4.9 – note that eccentricity, e, does not appear in these equations and is accounted for in the perigee, q, term. The terms I_{BA} and π_{BA} are formulated as follows:

$$(2\sin{(\frac{I_{BA}}{2})})^2 = (2\sin{(\frac{i_B - i_A}{2})})^2 + \sin{(i_A)}\sin{(i_B)}(2\sin{(\frac{\Omega_B - \Omega_A}{2})}))^2 \tag{4.2}$$

$$\pi_{BA} = \omega_B - \omega_A + 2\sin^{-1}(S_{BA}) \tag{4.3}$$

$$S_{BA} = \cos{(\frac{i_B + i_A}{2})}\sin{(\frac{\Omega_B + \Omega_A}{2})}\sec{(\frac{I_{BA}}{2})} \tag{4.4}$$

i refers to the inclination, Ω is the right ascension of the ascending node, and ω is the argument of perigee.

The Drummond formulation, D_D is given by,

$$D_D^2 = (\frac{e_B - e_A}{e_B + e_A})^2 + (\frac{q_B - q_A}{q_B + q_A})^2 + (\frac{I_{BA}}{180})^2 + (\frac{e_B + e_A}{2})^2(\frac{\theta_{BA}}{180})^2 \tag{4.5}$$

θ refers to the true anomaly and I_{BA} is the angle between the angular momentum vectors such that:

$$I_{BA} = \cos^{-1}(\frac{\vec{c}_A \cdot \vec{c}_B}{c_A c_B}) \tag{4.6}$$

c refers to the angular momentum such that,

$$\vec{c} = \vec{r} \times \vec{v} \tag{4.7}$$

Note that terms without the vector notation refer to scalar magnitudes. The term, θ_{BA}, is the angle between the lines of the apsides of the two orbits and is calculated in Equation 4.8.

$$\theta_{BA} = \cos^{-1}(\frac{\vec{e}_A \cdot \vec{e}_B}{e_A e_B}) \tag{4.8}$$

The Laplace-Runge-Lenz vector is defined as follows:

$$\vec{e} = \frac{(\vec{v} \times \vec{c})}{\mu} - \frac{\vec{r}}{r} \tag{4.9}$$

The D-Criterion, D_J, proposed by Jopek is shown in Equation 4.10.

$$D_J^2 = (e_B - e_A)^2 + (\frac{q_B - q_A}{q_B + q_A})^2 + (2\sin(\frac{I_{BA}}{2}))^2 + (\frac{e_B + e_A}{2})^2(2\sin(\frac{\pi_{BA}}{2}))^2 \tag{4.10}$$

Nodal Distance

Another measure of orbital distance is the nodal distance, D_{nodal}, which is defined as the distance between two osculating orbits, provided at the same epoch, along the line of mutual nodes [11]. The vector pertaining to the direction of the line of mutual nodes is given by Equation 4.11. The vector points towards the ascending node of object B with respect to object A.

$$\vec{d}_{node} = \vec{c}_A \times \vec{c}_B \tag{4.11}$$

The true anomalies, θ, of the two mutual nodes of the bodies in the direction of D_{node} are given by:

$$\cos(\theta_A) = \frac{\vec{e}_A \cdot \vec{d}_{node}}{e_A d_{node}} \tag{4.12}$$

$$\cos(\theta_B) = \frac{\vec{e}_B \cdot \vec{d}_{node}}{e_B d_{node}} \tag{4.13}$$

'e' is the magnitude of the Laplace-Lenz vector and c is the angular momentum.

Next, the geocentric distances of the two nodal points for each of the orbits can be found. Note that μ is the Earth's gravitational parameter. For object A:

$$r_{A,1} = \frac{c_A^2}{\mu(1 + e_A \cos(\theta_A))} \tag{4.14}$$

$$r_{A,2} = \frac{c_A^2}{\mu(1 - e_A \cos(\theta_A))} \tag{4.15}$$

Similarly, for object B:

$$r_{B,1} = \frac{c_B^2}{\mu(1 + e_B \cos(\theta_B))} \tag{4.16}$$

$$r_{B,2} = \frac{c_B^2}{\mu(1 - e_B \cos(\theta_B))} \tag{4.17}$$

Two nodal distances can then be obtained by subtracting the corresponding geocentric distances between objects A and B:

$$d_1 = |r_{B,1} - r_{A,1}| \tag{4.18}$$

$$d_2 = |r_{B,2} - r_{A,2}| \tag{4.19}$$

The smaller value between d_1 and d_2 is the nodal distance, D_{nodal}.

Of the four orbital distance formulations (3 D-Criteria) and nodal distance, [11] found D_{SH} and D_J to perform best – these formulations were able to correctly identify the breakup time and parent object for different test cases. The D_J formulation is used to generate results for this thesis due to its ease of application and performance. The other formulations were implemented for comparison and in accordance with [11], it was found that D_J and D_{SH} generated near identical results, while D_D and the nodal distance yielded less accurate breakup times. Figure 4.1 shows the performance of the various orbital distance formulations. MOID, the minimal orbital intersection distance, is also depicted but is not implemented in this research due to its complexity.
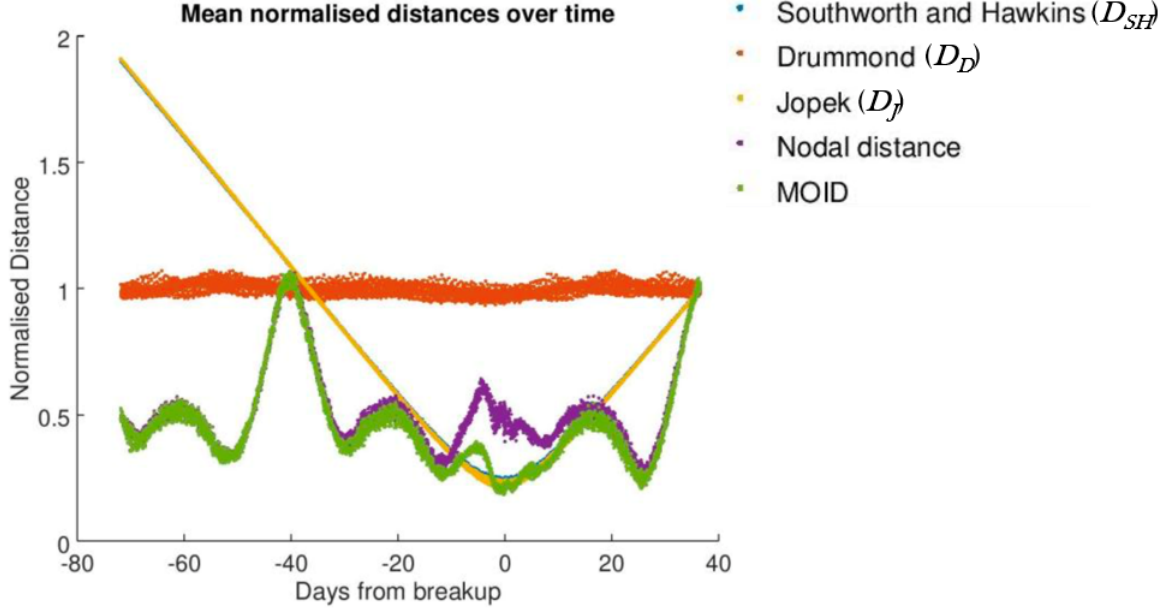
Figure 4.1. Mean normalized orbital distances pertaining to fragments of Orbcomm FM-16 [11].

Linear distance

The distance functions covered so far measure a form of orbital distance – accounting for the orbital elements of each of the fragments. A simpler, linear distance formulation, can also be put forth. Equation 4.20 calculates the Euclidean distance between two objects in three dimensions.

$$D_{linear} = \sqrt{(r_{x,B} - r_{x,A})^2 + (r_{y,B} - r_{y,A})^2 + (r_{z,B} - r_{z,A})^2} \qquad (4.20)$$

Here, the $r_{x,y,z}$ terms refer to the geocentric coordinates of the the corresponding fragment.

4.1.2 Breakup Epoch Determination

For this research, two of the five studied distance functions are applied to generate results – these are the D-Criterion developed by Jopek, D_J, and the linear distance formulation. These two distance functions are applied in three scenarios to find the breakup time as follows:

1. Minimizing inter-fragment distances: The distances between each and every fragment are found relative to each other. The mean of the inter-fragment distances is found and stored for each time step. The time which yields the minimum average inter-fragment distances is the breakup time.

2. Minimizing inter-fragment distances with pre-event parent: This is identical to scenario 1, but the pre-event parent object is also in the fragment 'mix'. This, of course, assumes the parent object is known and so are its orbital parameters before the breakup, which may not always be the case.

3. Minimizing fragment distances relative to pre-event parent: This scenario assumes information regarding the parent object before its breakup is available. The fragment distances are measured with respect to the parent object, as opposed to between the each of the fragments themselves.

Interestingly, it is found that the linear distance formulation consistently yields breakup epochs closer to ones in literature for test cases than the orbital distance formulation. Additionally, scenario 3, in which the distances are measured relative to the pre-event parent is found to work best. Thus the final results generated in this thesis use both of these techniques in unison. Figures 4.2, 4.3, and 4.4 demonstrate the performances of the breakup determination techniques for the Centaur event, 2018-079B, using data from the Vimpel catalog. The fragments are initially propagated to a common time, 12 AM Apr 15th 2019, and subsequently back-propagated to obtain the minimum distance. Figure 4.2 pertains to inter-orbit distances (not relative). The fragments do not converge to a point. This is the case in Figure 4.3 as well, which shows the orbital distances of fragments relative to the parent object. Conversely, Figure 4.4 shows an encouraging plot of the linear distances – all of which converge to a satisfying point. The breakup time obtained is 18:57 on Apr 6th 2019, which is the breakup date documented for this event in literature [35]. It is interesting to note that in either orbital or linear formulations, the mean distance of fragments relative to the parent object is smaller – this is indicative of fragment spread.
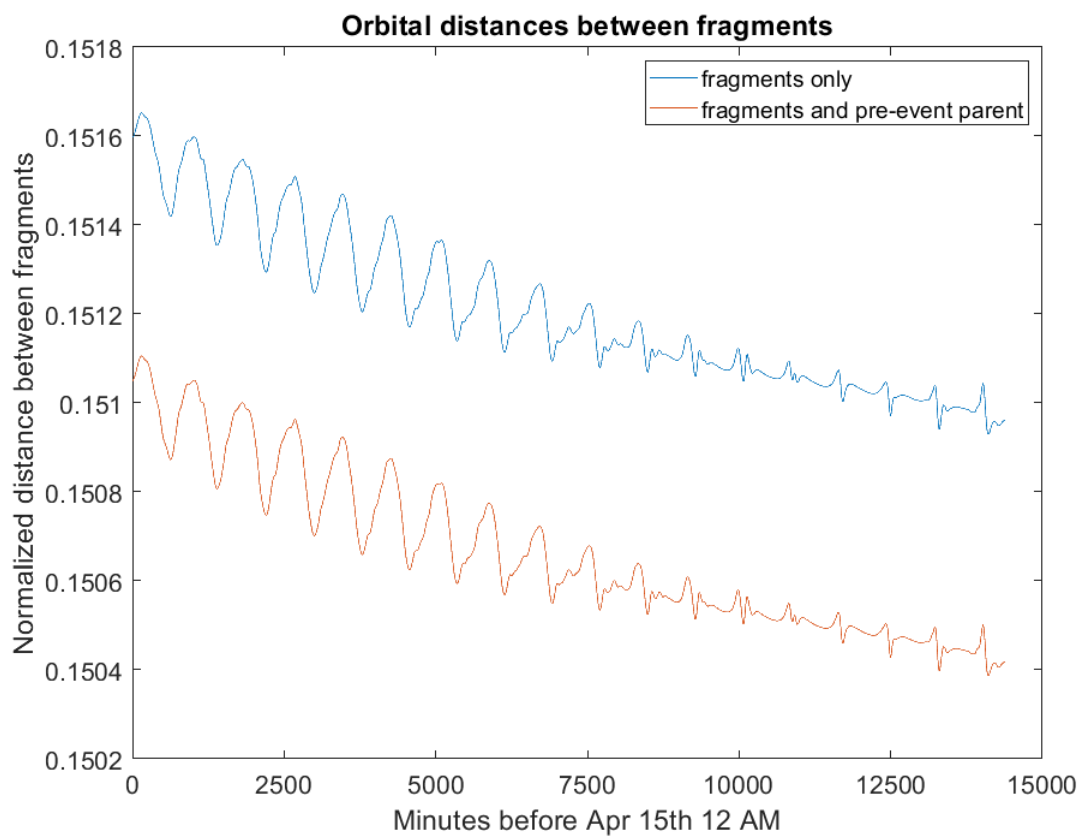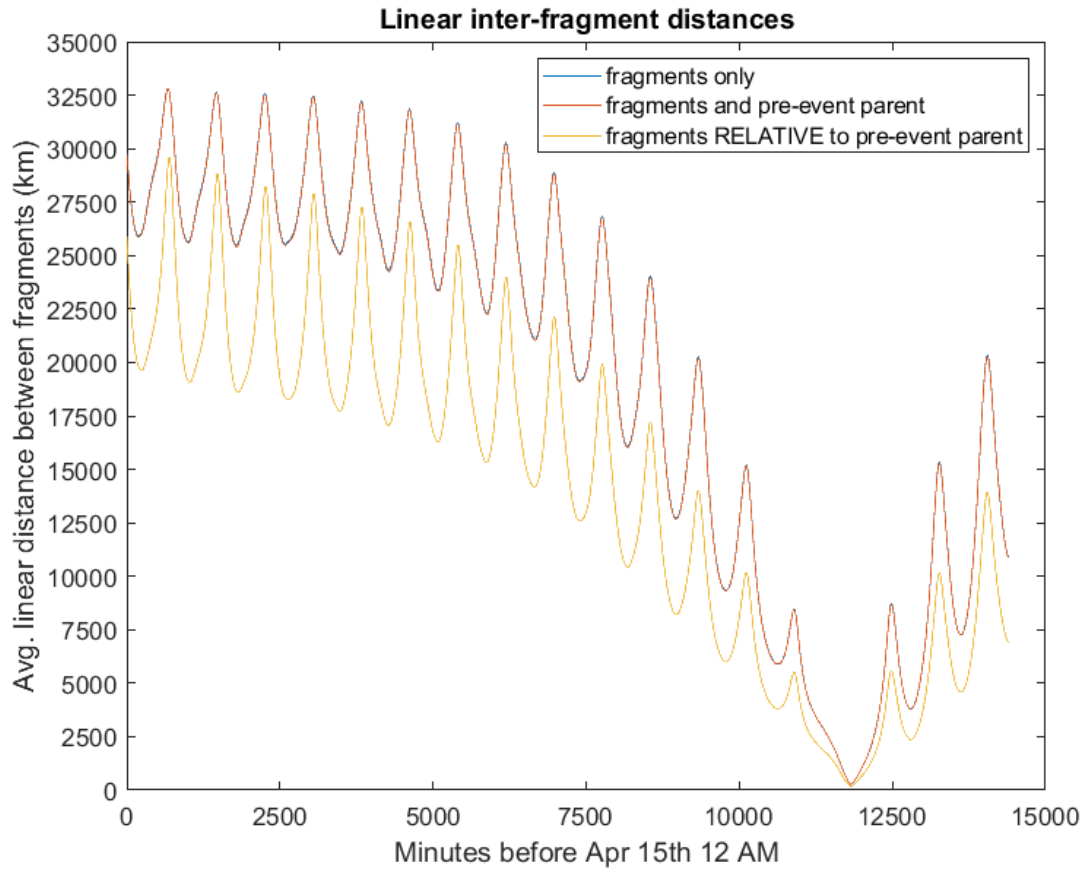
Figure 4.2. Inter-object orbital distances pertaining to 2018-079B.
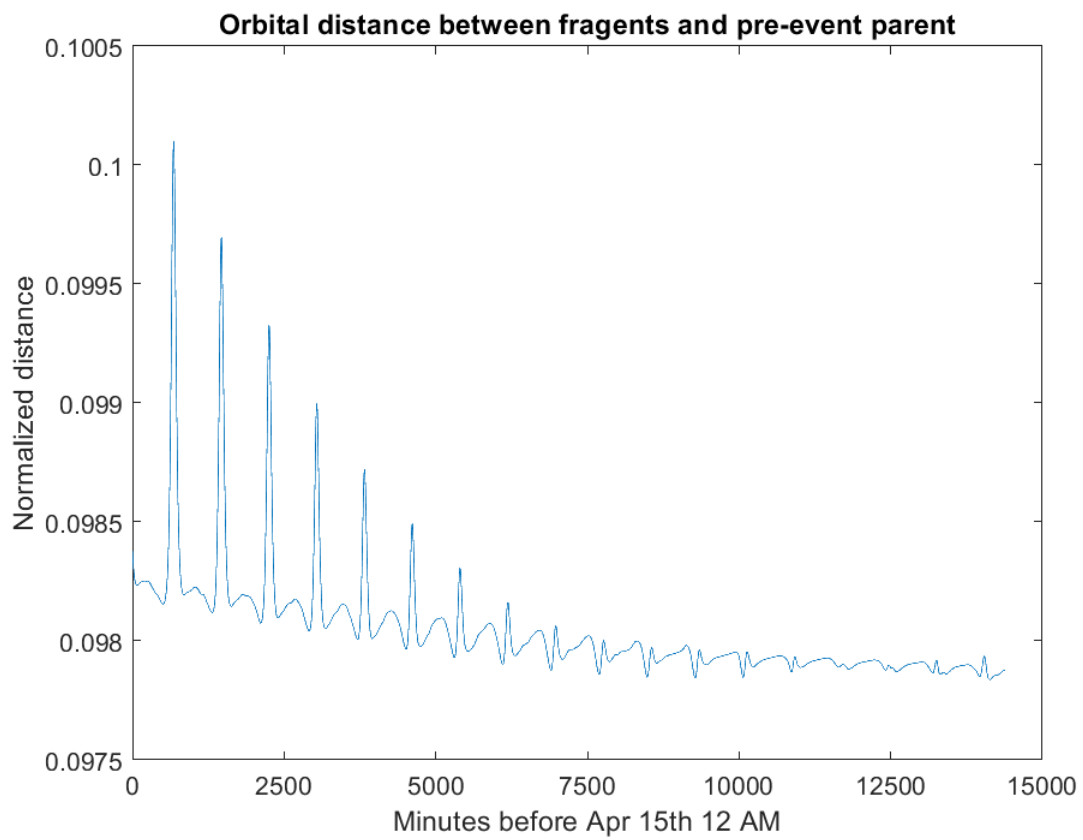
Figure 4.3. Orbital distances of fragments of 2018-079B relative to the pre-event parent.

Figure 4.4. Linear inter-object distances pertaining to the fragments of 2018-079B. The minimum corresponds to the documented breakup date of Apr 6th.

Once an appropriate distance function is selected, the breakup time can be calculated as follows:

1. Propagate all the orbits of the fragments (and pre-event parent if available) to a common time, t_0, after the event. This could be the mean epoch of the first determined orbits of the fragments [11].

2. Select a time, t_{prev}, that is before the hypothesized breakup time – this could be many months before the first cataloged fragments to ensure the event is not missed.

3. A time step is then chosen. It is crucial that this is as small is possible, so that a global minimum of the distance function is found.

4. At each time step, the mean fragment distances, d_{mean}, (as mentioned in the above scenarios) are found.

5. Finally, the minimum of the set of d_{mean} values across the interval $[t_{prev}, t_0]$ is found and this is the breakup time, t_b.

4.1.3 Parent Object Identification

Once the breakup epoch is identified – the parent object (in case it is not already known) can be found. This assumes the parent object is listed in the publicly available TLE catalog. The first step is to find the apogee, perigee, inclination, and right ascension of the ascending node values of each of the fragments at the calculated breakup time, t_b. The maximum and minimum values of each of these orbital elements pertaining to the fragments, will function as 'filters'. A margin can be added – about 100 km and around 5 degrees generally work well. The TLE catalog is then searched at a time before t_b – this can be up to 2 days prior if there is reason to believe t_b is not very accurately calculated. Objects that satisfy the filters are shortlisted as possible parent candidates. The distance function is then applied once again, this time measuring the mean distance between the fragments and the parent candidate. The candidate which minimizes the distance to the fragments is selected as the parent object.

4.2 Gabbard Diagrams

This section draws upon [4]. The Gabbard diagram is an instrumental tool in gathering preliminary insights surrounding fragmentation events. It was developed by John Gabbard, who used it to study the Delta upper stage fragmentation events in the 70's while working at the North American Aerospace Defense Command (NORAD). The diagram itself is a two-dimensional chart displaying all of the fragments of an event – the x axis pertains to the orbital period of the fragments, while the y axis pertains to the apogee and perigee altitudes. Both the apogee and perigee heights are marked for each fragment and necessarily lie on a vertical line.

In order to construct a Gabbard diagram, it is necessary to know some state information of the fragments. In particular, the semimajor axis, a, and the eccentricity, e, are of interest. The period, P, of an orbit can be related to a using the following relationship,

$$P = \sqrt{\frac{4\pi^2}{\mu}a^3} \tag{4.21}$$

where μ is the gravitational parameter of the Earth.
The apogee and perigee heights can then be obtained using Equations 4.22 and 4.23 respectively.

$$h_{apo} = a(1 + e) - R_E \tag{4.22}$$

$$h_{per} = a(1 - e) - R_E \tag{4.23}$$

where R_E refers to the Earth's radius.

It becomes evident that Gabbard diagrams depend on the semimajor axis and eccentricity of the fragments. a and e of the fragment orbits are naturally influenced by the intensity of the event and how the fragments dispersed from the event center. The change in a and e for a given fragment relative to the parent's orbit can be related to the velocity perturbations it received from the event. There are three orthogonal components to these

velocity perturbations – downrange or along-track (dv_d), radial (dv_r), and cross-range (dv_x). These components lie in the RSW coordinate frame (Section 3.3.2). Equations 4.24, 4.25, and 4.26, relate the change in orbital elements to the received velocity perturbations.

$$da = \frac{2}{n}(\frac{e\sin(\theta)}{\sqrt{1-e^2}}dv_r + \frac{a\sqrt{1-e^2}}{r}dv_d) \tag{4.24}$$

$$de = \frac{\sqrt{1-e^2}}{na}\left\{\sin(\theta)dv_r + \frac{a(1-e^2)}{er} - \frac{r}{ae}dv_d\right\} \tag{4.25}$$

$$di = \frac{r\cos(u)}{na^2\sqrt{1-e^2}}dv_x \tag{4.26}$$

i is the inclination, θ is the true anomaly, n is the mean motion, u is the argument of latitude of the parent object, and r is the geocentric distance to the object. These equations indicate that a and e are affected by both dv_d and dv_r, while i is only affected by dv_x.

It is also possible to relate the energy of a fragment to these velocity perturbations. The energy of the parent object prior to its fragmentation is,

$$E = \frac{1}{2}[v_r^2 + v_d^2] - \frac{\mu}{r} \tag{4.27}$$

where v_r and v_d refer to the radial and downrange velocities of the parent object.

The specific total energy of a fragment following the fragmentation event is,

$$E + dE = \frac{1}{2}[(v_r + dv_r)^2 + (v_d + dv_d)^2 + dv_x^2] - \frac{\mu}{r} \tag{4.28}$$

Thus, the change in specific energy, dE, of the fragment is given by,

$$dE = v_d dv_d + v_r dv_r + \frac{1}{2}(dv_r^2 + dv_d^2 + dv_x^2) \tag{4.29}$$

Gabbard diagrams can provide key information on the altitude of a breakup, the nature of the orbit, and dispersal speeds and directions of the fragments. Events in circular or near-circular orbits versus those in more elliptical orbits have characteristic features – these identifiable traits are covered in the following sections.

4.2.1 Circular Orbits

In the case of circular of near-circular orbits, $e \approx 0$, and $a \approx r$. Equations 4.24 and 4.25 thus simplify to,

$$da = \frac{2}{n}dv_d \tag{4.30}$$

$$de = \frac{\sin(\theta)}{na}dv_r \tag{4.31}$$

Differentiating Equation 4.21 and substituting Equation 4.30,

$$dP = \frac{3P}{an}dv_d \tag{4.32}$$

It becomes evident that the change in period of a fragment relative to its initial (parent) orbit is directly proportional to its change in downrange velocity.

The change in apogee and perigee heights of a fragment can be obtained by differentiating Equations 4.22 and 4.23. By substituting 4.24 and 4.25,

$$dh_{apo} = \frac{2}{n}dv_d + \frac{\sin(\theta)}{n}dv_r \tag{4.33}$$

$$dh_{per} = \frac{2}{n}dv_d - \frac{\sin(\theta)}{n}dv_r \tag{4.34}$$

It can be seen that cross-range perturbations do not affect the apogee and perigee heights.

If the downrange velocity imparted on a fragment is positive, the fragment gains energy, and both a and P of the fragment will increase. In accordance with the *Hohmann transfer principle*, h_p is not affected by dv_d [4] – this simplifies Equation 4.35 to,

$$dh_{per} = -\frac{\sin(\theta)}{n}dv_r \tag{4.35}$$

In a perfectly circular orbit, if there is no radial perturbation on the fragments, the perigee points would lie horizontally on a straight line, with the apogee points vertically above them, oriented with a positive slope. If there is a dv_r perturbation, the apogee and perigee points are shifted above and below their respective lines by the distance given by the dv_r terms in Equations 4.33 and 4.35. This forms the right side of the Gabbard diagram. Similarly,

50

the left side can be constructed – in this case, the fragments possess negative downrange velocities, the fragments lose energy, and have smaller P and a compared to the parent object. The Hohmann transfer principle dictates that there will be no change in the apogee height such that,

$$dh_{apo} = \frac{\sin(\theta)}{n} dv_r \tag{4.36}$$

dh_{per} will take the same form as Equation 4.34. Now, the apogee points lie on a horizontal line, with the perigee points lying vertically below on an inclined line with the same slope as the right side of the plot. The inclined slope has a gradient of,

$$m = \frac{4a}{3P} \tag{4.37}$$

The point of intersection of the horizontal and inclined lines yields the location of the fragmentation point – the P_0 and h_0 at this point are the period and fragmentation altitude of the parent. These intersecting lines form a characteristic 'x' shape for circular orbits.

The above equations highlight key relationships between different parameters which govern the Gabbard diagram. Conclusions regarding the intensity of an event can be drawn by visually inspecting a Gabbard diagram and noting the spread of fragments from the center (P_0, h_0). The extension of data points horizontally on either side of P_0 gives an indication of the maximum dv_d imparted on the fragments. Similarly, the spread of fragments above and below the apogee and perigee lines indicates the maximum dv_r imparted – this maximum is likely to occur at the fragmentation center where the dv_d should equal 0. If the fragmentation event is isotropic in nature, the maximum dv_d and dv_r values should be similar in magnitude.

The key characteristics of a fragmentation in a circular orbit are summarized in Figure 4.5. The fragments that receive posigrade impulses ($dv_d > 0$) speed up in their orbits, while those that receive retrograde impuslses ($dv_d < 0$) slow down.
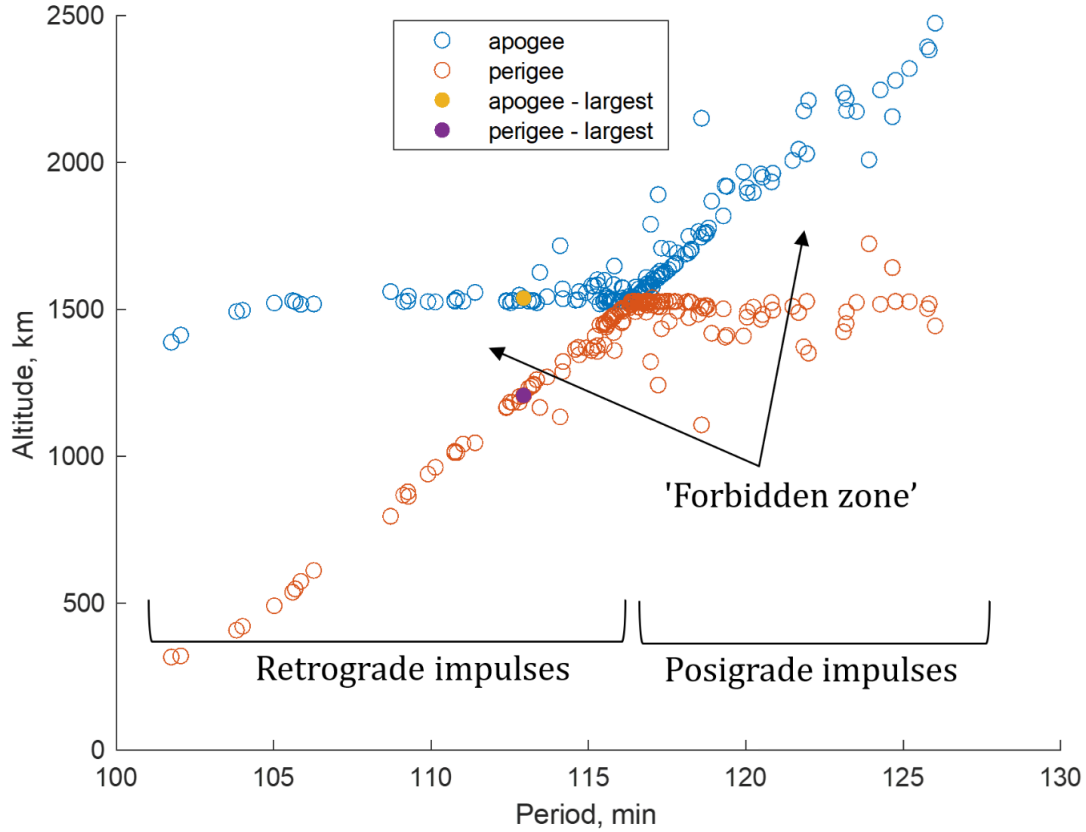
Figure 4.5. Gabbard diagram pertaining to the NOAA-3 upper stage fragmentation event in a near-circular orbit – 161 fragments are shown, with the largest fragment identified.

One can note that the region between the two lines is largely devoid of data points – this is the 'forbidden zone'. In some cases, data points may congregate on the left most side of the plot in this forbidden zone; these would be fragments that are affected by atmospheric drag. Drag acts to reduce the semimajor axis and eccentricity of orbits (noticeable for elliptical cases) – these data points thus possess lower apogee/perigee heights and smaller periods.

4.2.2 Elliptical Orbits

Gabbard diagrams for elliptical orbits have fewer characteristic traits, but can still be insightful. The two apsidal lines do not directly intersect for elliptical lines, but they would intersect if extended. This hypothetical intersection point alludes to the period of a frag-

menting object in a circular orbit at that altitude.

The forbidden zones of Gabbard diagrams for elliptical orbits are also different – they are dependent on where in its orbit the satellite fragmented (its true anomaly). If the satellite is ascending ($0 < \theta < \pi$), the forbidden zone appears in between the two apsidal lines. Conversely, if the parent satellite was descending in its orbit ($\pi < \theta < 2\pi$), the forbidden zone is above the apogee line and beneath the perigee line. Additionally, the slopes of the apsidal lines are indicative of the true anomaly of the fragmenting satellite. If the fragmentation occurs near the perigee (where $\theta = 0$) for instance, the perigee line is horizontal. These trends are summarized in Figure 4.6 – note that θ refers to θ (true anomaly) and θ_0 refers to the true anomaly at which the slopes of the two apsidal lines are equal.

In the case of highly elliptical orbits (HEO), where the eccentricity is generally above 0.5, Gabbard diagrams usually contain even fewer characteristic traits than elliptical orbits. This is because the slope of the perigee line is usually far smaller than that of the apogee line and there is a large gap between the two. Nevertheless, some insights regarding the energy of the event can still be obtained by considering the horizontal spread of the fragments (indicative of downrange velocity perturbations) and any deviations away from the apsidal lines (indicative of radial velocity perturbations). These are further discussed with examples pertaining to the Centaur upper stage events in Section 6.4.

4.3 Velocity Perturbations

This section references [36]. Once preliminary insights regarding an event are gleaned from Gabbard diagrams, it is beneficial to obtain the actual velocity perturbations – their magnitudes are instrumental in determining the energy of an event, which subsequently enables one to hypothesize its cause.

The velocity perturbations are calculated in the local, RSW, frame of the satellite. The total velocity of a satellite is given by,

$$v = \sqrt{\mu(\frac{2}{r} - \frac{1}{a})} \tag{4.38}$$
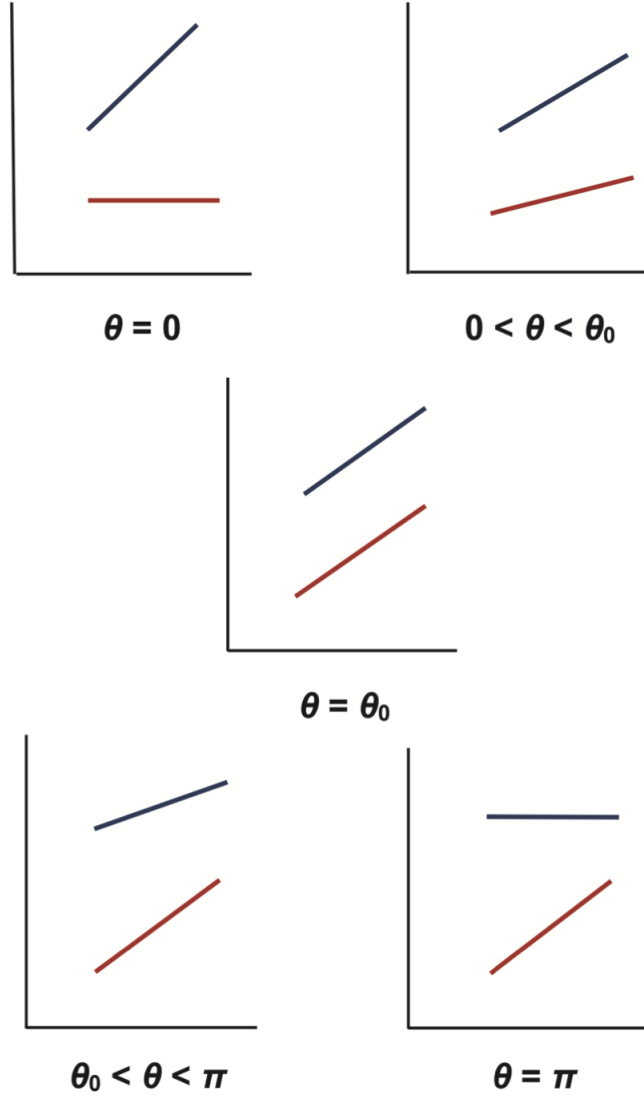
Figure 4.6. Trends in apsidal lines with respect to true anomaly for elliptical Gabbard diagrams. [4].

This velocity is in the plane of motion, with downrange (v_d) and radial (v_r) components as shown in Equations 4.39 and 4.40.

$$v_d = \sqrt{\mu a \left(\frac{1 - e^2}{r^2} \right)} \qquad (4.39)$$

$$v_r = \pm \sqrt{v^2 - v_d^2} \qquad (4.40)$$

In accordance with prior symbol definitions, a refers to the semimajor axis, e is the eccentricity, r is the geocentric distance to the satellite, and μ is the gravitational parameter. The sign of the radial velocity, v_r, depends on whether the satellite is ascending or descending in its orbit – a positive sign applies when θ (true anomaly) $< \pi$ and a negative sign is used when $\theta > \pi$. There is no initial out of plane motion. When this parent satellite fragments, it imparts impulses on fragments, each of which receive velocity perturbations in three orthogonal components: downrange (dv_d), radial (dv_r), and cross-range (dv_x). Figure 4.7 depicts the velocity perturbations in the local frame of the satellite. The origin pertains to the fragmentation point.
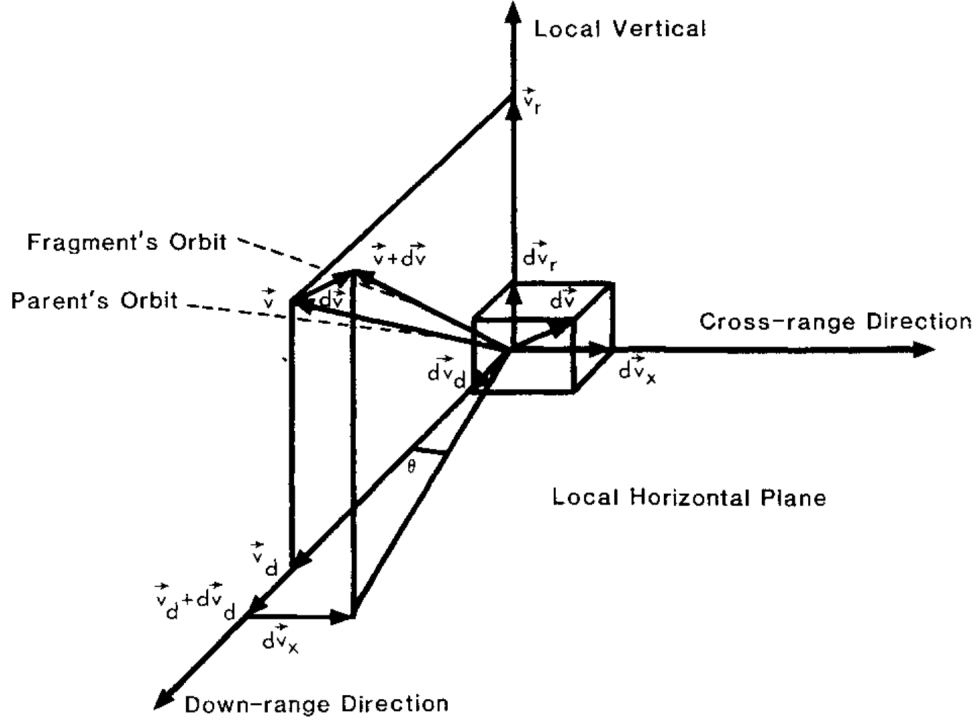
Figure 4.7. Velocity components of the parent satellite and a fragment in the local RSW reference frame [36]. θ refers to the plane-change angle in this case.

Following the fragmentation event, each fragment will posses the following velocities in each of the three components: $v_d + dv_d$, $v_r + dv_r$, and dv_x – where the first term for both the downrange and radial components pertains to the parent's velocities and the second term indicates the added velocity perturbation imparted as a result of the fragmentation. Using

the velocity definitions above, it is possible to determine the change in specific energy of a fragment,

$$E' - E = \frac{1}{2}(v'^2 - v^2) = \frac{-\mu}{2}(\frac{1}{a'} - \frac{1}{a}) \tag{4.41}$$

where the ($'$) terms pertain to the fragment and those without it pertain to the parent satellite. Equation 4.41 can also be written in terms of the velocity perturbations:

$$E' - E = \frac{1}{2}[(v_r + dv_r)^2 + (v_d + dv_d)^2 + dv_x^2 - v_r^2 - v_d^2] \tag{4.42}$$

The change in the specific angular momentum of a fragment can be obtained using,

$$h'^2 - h^2 = |r \times v'|^2 - |r \times v|^2 = \mu a'(1 - e'^2) - \mu a(1 - e^2) = r^2[(v_d + dv_d)^2 + dv_x^2 - v_d^2] \tag{4.43}$$

Additionally, the plane-change angle, ζ, between the new, perturbed orbit of the fragment relative to the initial parent object is given by,

$$\tan(\zeta) = \frac{dv_x}{v_d + dv_d} \tag{4.44}$$

ζ can also be found as a function of the inclinations of the parent orbit (i), the fragment's orbit (i'), and the latitude of the fragmentation point (λ).

$$\zeta = \pm \cos^{-1}(\frac{\cos(i)\cos(i') + \sqrt{(\cos^2(\lambda) - \cos^2(i))(\cos^2(\lambda) - \cos^2(i'))}}{\cos^2(\lambda)}) \tag{4.45}$$

Here, the positive sign is used when $i' > i$ and the negative sign is used when $i' < i$ if the satellite is ascending. The converse is applied when the satellite is descending.

Figure 4.8 helps visualize the 'breakup spherical triangle' that yields Equation 4.45. u refers to the argument of latitude.

Equations 4.42, 4.43, and 4.44 are simultaneous equations that can be solved for the three unknowns, dv_d, dv_r, and dv_x. The solutions yield,

$$dv_d = \frac{\cos(\zeta)}{r}\sqrt{\mu a'(1 - e'^2)} - v_d \tag{4.46}$$
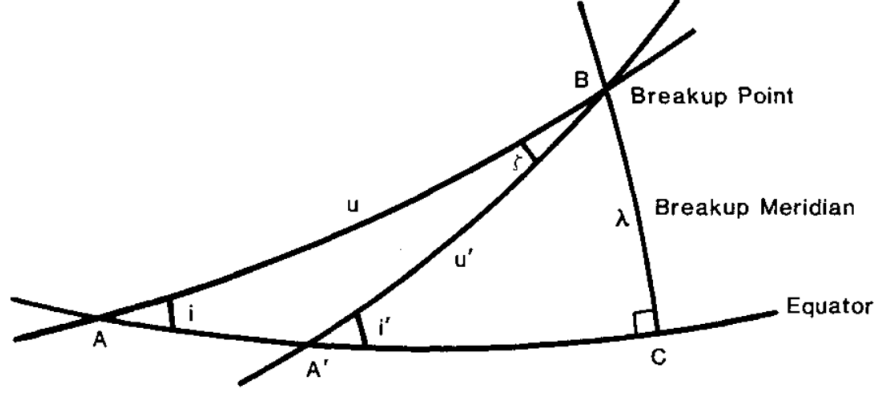
Figure 4.8. Breakup spherical triangle displaying phase-change angle of a fragment with respect to its parent satellite. [36].

$$dv_r = \pm\sqrt{\mu(\frac{2}{r} - \frac{1}{a'}) - \frac{\mu}{r^2}a'(1 - e'^2)} - |v_r| \tag{4.47}$$

$$dv_x = \frac{\sin{(\zeta)}}{r}\sqrt{\mu a'(1 - e'^2)} \tag{4.48}$$

μ refers to the gravitational parameter of the Earth, ζ is the plane-change angle, a is the semimajor axis, e is the eccentricity, and r is the geocentric distance. v_d and v_r refer the the parent object's downrange and radial velocities respectively. As with v_r, the sign of dv_r depends on whether the fragment is ascending or descending. The true anomaly of the fragment, θ, can be found using,

$$\theta' = u' - \omega' \tag{4.49}$$

where u' and ω' refer to the argument of latitude and the argument of perigee of the fragment respectively.

A direct correlation exists between the velocity perturbations (dv_d, dv_r, dv_x) and the orbital elements, semimajor axis (a), eccentricity (e), and inclination (i). Fragments which receive a positive dv_d tend to have higher a values than the parent object and vice versa. Similarly, fragments which receive a positive dv_x generally move into a higher i orbit than the parent object. The relationship between dv_r and e is similar – a positive dv_r often results in a more eccentric orbit. These relationships are also telling of the impact uncertainties in orbital elements could have on the outcomes of the velocity perturbations. An uncertainty

in inclination, for instance, would affect the plane-change angle, which in turn would result in inaccurate downrange and cross-range velocity perturbations.

While these exact equations yield usable results in most scenarios, the presence of the square root in the equations sometimes results in imaginary values. In the case of dv_r, very low eccentricities can result in an imaginary solution. On the other hand, certain values of the plane-change angle can result in imaginary dv_d and dv_x values – ζ is complex when the latitude of fragmentation exceeds the inclination. In this research, the breakup time used to calculate the velocity perturbations is slightly adjusted in some scenarios to obtain sufficient real values for subsequent analysis. Additionally, it is important to consider the effect of uncertainty in the state information pertaining to the parent object and the fragments. While the equations are mostly functions of slowly varying orbital elements, any uncertainty arising from initial optical measurements or propagation, will certainly impact the resulting velocity perturbations.

Upon obtaining the velocity perturbations imparted on the fragments due to the event, the intensity of an event can be found. This is defined as a measure of the average specific kinetic energy imparted on a fragment for a given event. The total velocity perturbation on a fragment is,

$$dv = \sqrt{dv_d^2 + dv_r^2 + dv_x^2} \tag{4.50}$$

Once the average dv amongst all the fragments is known, the average specific kinetic energy for an event in m^2/s^2 can be found using,

$$E = \frac{1}{2}dv^2 \tag{4.51}$$

4.4   Angular Perturbations

This section draws on [4]. In addition to the spreading speeds of the fragments, the direction of dispersal is also of interest – that is, which way did the fragments head, following the event? These angular perturbations are not only dependent on the manner of fragmentation

(explosion/collision with satellite/collision with debris), but are also affected by *where* on the parent satellite the impact/rupture occurred. Thus, by uncovering the angular perturbations, it is possible to work backwards and trace how exactly the fragmentation unfolded and subsequently postulate its cause.

One can define two angles, akin to the latitude and longitude of the Earth, as a function of the three orthogonal components of the velocity perturbations on the fragments (dv_d, dv_r, and dv_x). Equations 4.52 and 4.53 show how the latitude, λ, and longitude, ϕ, are computed respectively.

$$\lambda = \sin^{-1}\left(\frac{dv_r}{dv}\right) \tag{4.52}$$

$$\phi = \tan^{-1}\left(\frac{dv_x}{dv_d}\right) + n\pi \tag{4.53}$$

where $n = 0$ if $dv_d > 0$, $n = 1$ if $dv_d < 0$ AND $dv_x > 0$, and $n = -1$ if $dv_d < 0$ AND $dv_x < 0$.

The relationship between these angular coordinates and the velocity components are summarized in Figure 4.9.
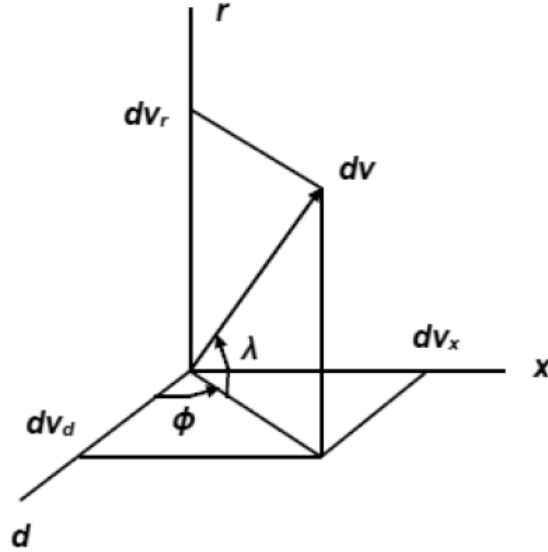
Figure 4.9. Angular coordinates (λ,ϕ) pertaining to *dv* received by a fragment. The origin denotes the fragmentation point [4].

Depending on the signs of the velocity components, the defined angular coordinates occupy one of eight octants in three-dimensional space. These coordinates can then be

projected onto a *Lambert's equidistant cylindrical projection map* to help visualize the spread of the fragments on a hypothetical sphere.

4.5   Fragmentation Models

This section references [4] and [37]. The dispersal of fragments is naturally dependent on the cause of the event – a fragmentation event as a result of a single rupture location will have a very different, characteristic, angular distributions than one arising from an explosive event, with multiple rupture locations. Benz et al. [37] put forth three fragmentation models used to describe propellant tank explosions. These are shown in Figure 4.10. Note that this is a 2D representation – the circle shown is a cross-section of a propellant tank. The solid lines indicate fragment speeds, while the dotted lines denote escaping gases.
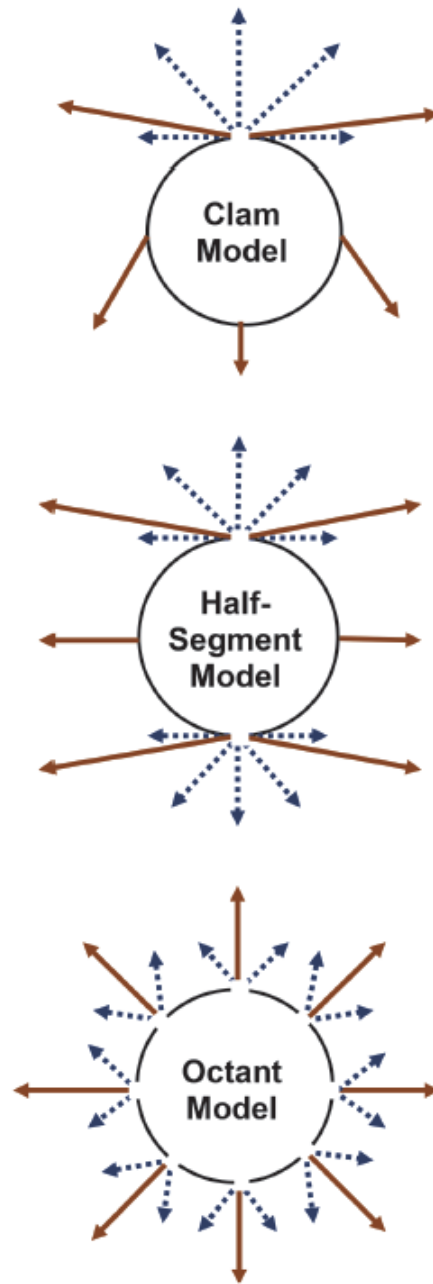
Figure 4.10. Fragmentation models describing three key forms of propellant tank explosions. The solid lines represent the relative fragment speeds; the dotted lines indicate escaping gases. [4].

The three models are briefly described as follows:

1. Clam model: This model is used to describe cases where there is single rupture location from which gases escape. Most of the fragments are pushed to the opposite side of this rupture point, with nearly half of them being confined in a 50 degree cone angle. The fragments departing tangentially from the impacted area possess the highest velocities and those directly opposite the rupture possess the smallest velocities.

2. Half-segment model: In this model, there are two rupture locations at opposite ends. The fragments are pushed outwards, roughly orthogonal to a hypothetical line connecting the ruptures. The fragment distribution resembles a donut or torus.

3. Octant model: This model is applicable to situations with multiple rupture locations. Here, the fragment distribution is generally isotropic (uniform distribution in every direction), with relatively consistent spreading speeds. The fragments are also likely to be similarly sized.

The relationship between the spreading speeds of the fragments and the location of the rupture point can be understood by studying the momentum transfer. For a rocket body with length, l, mass, m, and cross-sectional area, A, its density, ρ is given by,

$$\rho = \frac{m}{Al} \tag{4.54}$$

For a given fragment, the change in momentum, dp, received from the event is a product of the force and time duration:

$$dp = F dt \tag{4.55}$$

Assuming the fragmentation occurs instantaneously, the change in momentum in the small time duration, dt, can be neglected.

Thus, only the force imparted is of interest, such that

$$dp = d(mv) = mdv \tag{4.56}$$

since mass is constant.

The pressure, P, acting on a fragment during the event is,

$$P = \frac{F}{A} \tag{4.57}$$

Rearranging,

$$dv = \frac{P A dt}{m} = \frac{P dt}{\rho l} \tag{4.58}$$

The velocity perturbation on the fragment as a result of the fragmentation event is proportional to the force impacted on it. Since the force is its peak at the rupture locations (due to exiting gases leaving at high pressures), the fragments leaving these areas travel with higher speeds than those situated furthest away from the rupture locations.

5. VALIDATION RESULTS

Before the techniques outlined in the previous chapters are applied to the Centaur events, they are first validated for well-studied, historic events. Specifically, the following four events are used as the test-cases: NOAA-3 second-stage rocket body (RB), Landsat-1 second-stage RB, Nimbus-6 second-stage RB, Spot-1 third-stage RB – these were selected due to availability of sufficient TLEs in the public catalog. Additionally, *Theory of Satellite Fragmentation in Orbit* ([4]) investigated these events in detail and is thus used as the primary source for validating the methods discussed in this work. Results pertaining to the NOAA-3 and Spot-1 events are presented and discussed in this section; results for the Landsat-1 and Nimbus-6 events are shown in the appendix (Sections A.1 and A.2).

The NOAA-3 RB (1973-084B) was the first of the seven Delta upper stages which exploded in the time frame between 1973-1981. The fragmentation event occurred on 28th December 1973, which is about two months after it was deployed. The RB fragmented at an altitude of 1515 km over the south-west region of the Pacific Ocean at 37°S latitude and 181°E longitude. About 130 kg of propellants were left in the tank. The RB was cylindrical in shape with the following parameters: length - 6.3 m, diameter - 1.4 m, dry mass - 840 kg. Prior to the event, the RB was in a nearly circular Sun-synchronous orbit with an eccentricity of 0.0005689 and an inclination of 102.05°[38]. 165 fragments cataloged through 25th November 1974 were used in the analysis done by [4]. For this work, 161 fragments cataloged through 25th November 1974 on the Spacetrack catalog are used.

The Spot-1 Ariane RB (1986-019C) is widely considered an anomalous event with some sources citing propulsion-related causes [39] and others posturing that the RB may have been struck by a small debris [40] [41]. The event occurred nine months after its launch into a Sun-synchronous orbit – the RB fragmented over eastern Africa (latitude: 7°N, longitude: 42°E) at 805 km on 13th November 1986. The RB was cylindrical and had the following parameters: length - 10.3 m, diameter - 2.6 m, dry mass - 1400 kg. The rocket was in a nearly circular orbit with an eccentricity of 0.0021203 and an inclination of 98.6973°. [38].

[4] used 226 catalogued and 237 uncatalogued fragments as of 25th Febuary 1987. For this work, 266 fragments from the TLE catalog are used, and are also the fragments catalogued as of 25th Febuary 1987.

The following sections calculate relevant breakup characteristics of both of these events – findings are compared and validated with those in [4].

5.1 Breakup Epoch

The breakup time of the NOAA-3 RB in literature is 0904 GMT on 28th December 1973 [38]. In order to test the breakup algorithm, the breakup epoch is calculated using the methods described in Section 4.1.

Table 5.1 shows the breakup times obtained using four techniques – orbital (orbital) and linear (linear) inter-object distances, and orbital (orbital rel) and linear (linear rel) distances relative to the pre-event parent. The pre-event parent object is also used in the inter-object distance techniques.

Table 5.1. Breakup times of the NOAA-3 event using different breakup algorithms.

Technique	Time	Distance
Orbital	~21:00, 29th Dec 1973	0.0139
Orbital rel.	~18:00, 29th Dec 1973	0.0094
Linear	09:04, 28th Dec 1973	1089.38 km
Linear rel.	09:04, 28th Dec 1973	574.96 km

Following the first iteration of the breakup algorithm (which calculates the distance once a day for n specified days), both the orbital distance functions arrive at 28th Dec, while the linear distance functions arrives at 27th Dec. Additionally, iterating by the hour for 48 hours surrounding each date, results in the mean orbital distances arriving at minimums in the evening of 28th Dec. The linear distances, on the other hand, arrive at ~9:00 on 28th Dec! Further iterations are not carried out for the orbital functions since they would hover around the hour and are clearly not close to the breakup time in literature. Calculating the

65

linear distances each minute over a 2-hour period about the suspected hour (9:00) yields the correct breakup time of 09:04.

A similar process is repeated for the Spot-1 event – once again, the breakup time in literature, 19:40 (GMT) on 13th November 1986, is obtained using the linear distance functions.
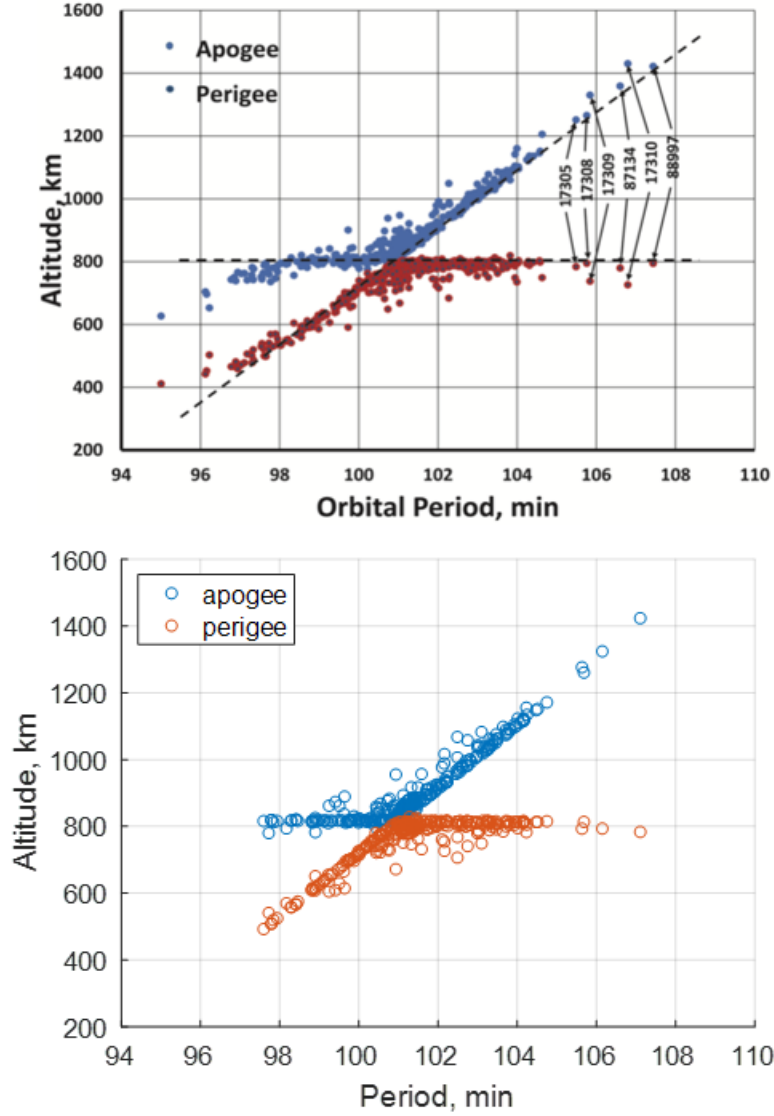
5.2 Gabbard Diagram

5.2.1 NOAA-3

The Gabbard diagram for the NOAA-3 event, is shown in Figure 5.1. On the left, is the plot generated by [4] for comparison. Since the same dataset (from Spacetrack) and roughly equal numbers of fragments are used, the observed congruence is expected. The largest fragment, assumed to be the fragment which inherits the international desginator of the parent object, is identified. The 'X' shape of the plot is characteristic of near-circular or circular orbits. The center of the 'X' marks the position of the fragmentation – the altitude at this intersection, does seem to align with the breakup altitude of 1515 km. The distribution of fragments on either side of this fragmentation point appears to be fairly even, suggesting this may be an isotropic fragmentation. However, there are a few fragments on the left-hand side that seem disconnected from the 'X' and possess lower periods – these fragments received negative downrange perturbations and slowed down relatively more in their orbits. The 'forbidden zone' between the two slopes is largely devoid of fragments, suggesting drag effects are not yet dominant.
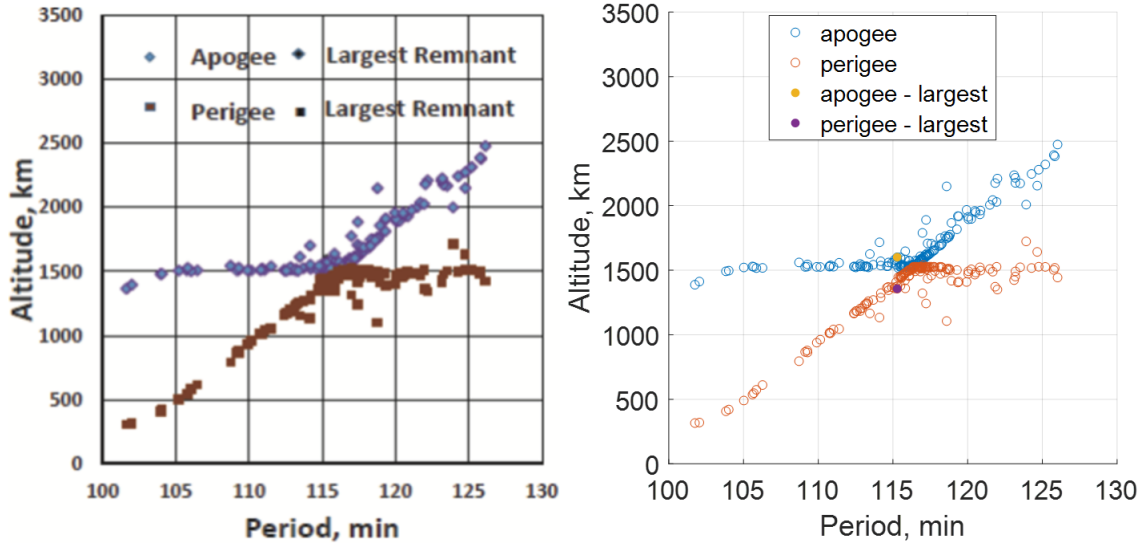
Figure 5.1. NOAA-3: Gabbard diagram of fragments compared with [4] (left).

5.2.2 Spot-1

The Gabbard diagram for the Spot-1 event, is shown in Figure 5.2. Since the Spot-1 RB was also in a near-circular orbit, its Gabbard plot also shows the characteristic 'X' shape – however, it can be seen that the horizontal spread of data points covers a lesser period range as compared to the NOAA-3 event. This points to a lower energy event. The data used by [4] included 197 more fragments, justifying the additional data points present in its plot (top). Some of the fragments studied by [4] experienced drag effects as indicated by the points in the forbidden zone on the left-hand side. Conversely, little to no fragments are in the forbidden zone in the replicated plot – it is possible that the fragments that were most affected by drag were uncatalogued. While the fragment spread is fairly even on both sides of the center, there are a handful of fragments that received large downrange perturbations and sped up in their orbits; these are labelled in the top plot from [4]. Note that the largest remnant is not identified since none of the fragments inherited the international designator of the parent object following the event.

Figure 5.2. Spot-1: Gabbard diagram of fragments compared with [4] (top).
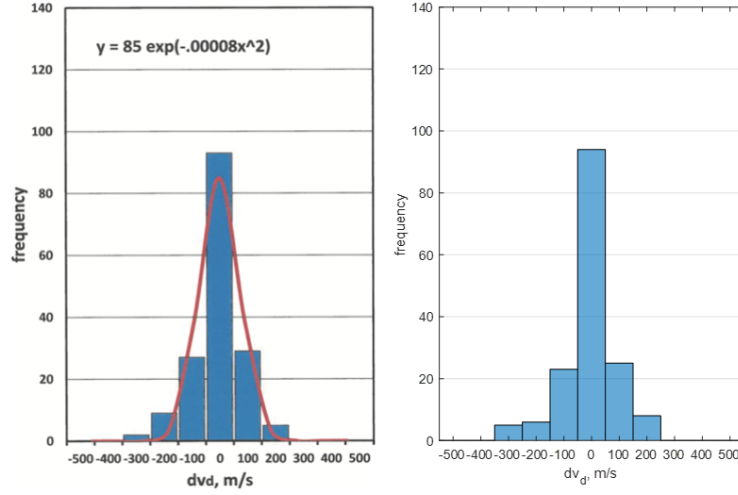
5.3   Velocity Perturbations

5.3.1   NOAA-3
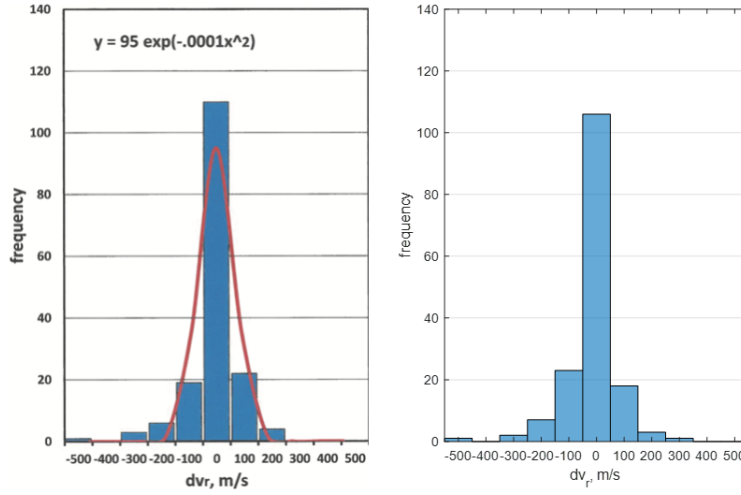
Fragment Velocity Frequencies:

Figure 5.3 shows the velocity perturbations on the fragments and their relative frequencies for the NOAA-3 event. The generated plots are very close to those documented in [4] (shown on the left) – a slight discrepancy occurs in the dvr frequency plot, but that is likely a result of using slightly different TLE sets (fewer TLEs were used for the replication).

The general trends are fairly isotropic in nature, with a roughly even number of fragments receiving positive and negative perturbations across all components. Upon a closer look at the number of fragments with positive and negative perturbations, it becomes evident that more fragments received positive dvd and dvx perturbations, while slightly less fragments received negative dv perturbations. Figure 5.4 is in alignment with the typical exponential trend of fragment velocities that are characteristic of explosive fragmentations – fragments with higher velocities are lower in frequency. It must be noted that the dvr for 27 fragments resulted in complex numbers and these were defaulted to 0.

(a) NOAA-3: Downrange velocities of fragment.

(b) NOAA-3: Radial velocities of fragments.
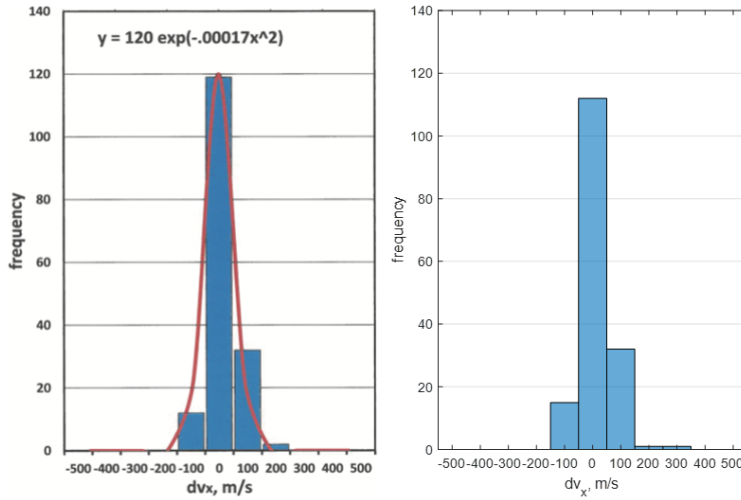
(c) NOAA-3: Cross-range velocities of fragments.

Figure 5.3. NOAA-3: Velocity frequencies of fragments compared with [4] (left).
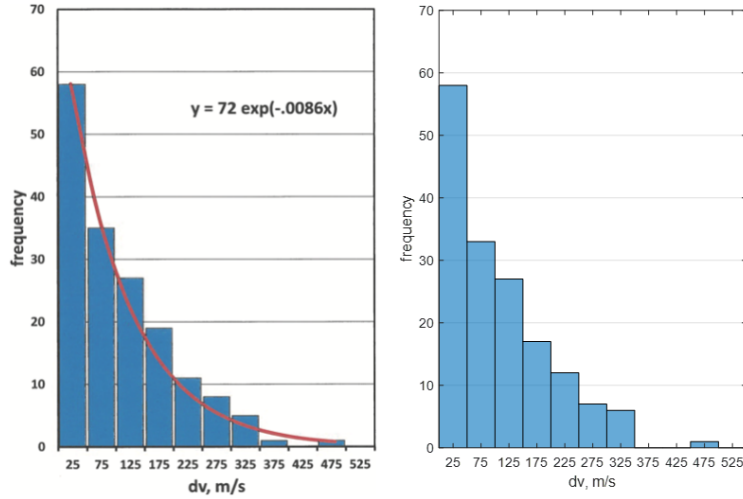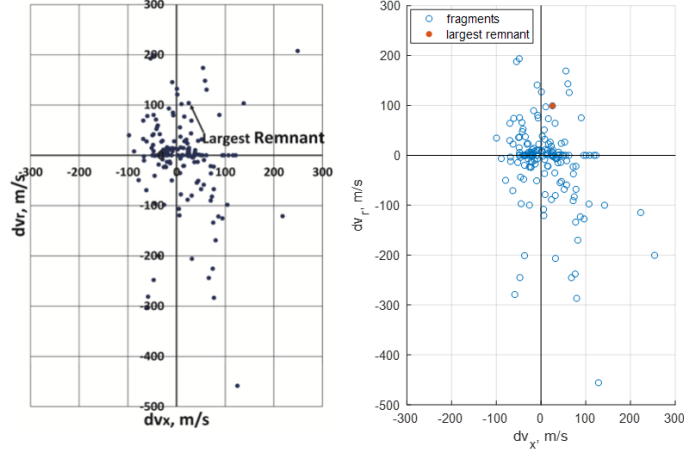
Figure 5.4. NOAA-3: Total velocity perturbations of fragments compared with [4] (left).
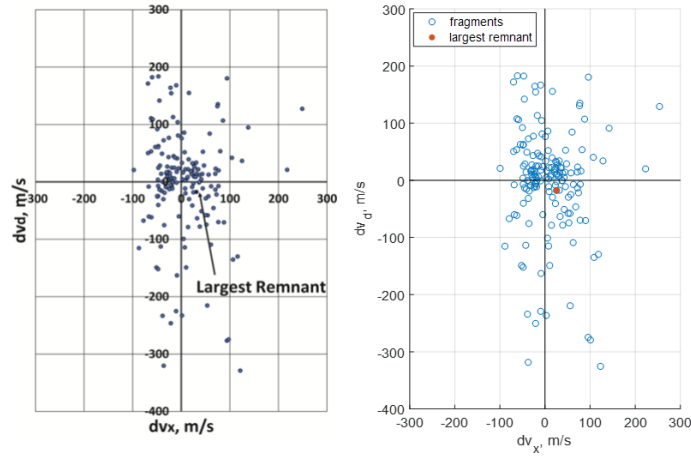
2D and 3D Fragment Velocity Distributions:

Figure 5.5 shows the velocity distributions in the 2D plane. As expected based on the isotropic distributions observed in the Gabbard and frequency plots, the 2D velocities also appear to be fairly evenly distributed, without notable directionalities. There is a noticeably lower range of dvx velocities, relative to dvd and dvr; large out-of-plane perturbations are generally a product of collisions, so this supports and explosive fragmentation hypothesis. It is interesting to note that the largest fragment received a large positive dvr (radially outward) perturbation. The 3D plot in Figure 5.6 summarizes the observed trends. The largest remnant in the replicated plot is shown in black. 6 fragments with unusually large negative radial velocities are circled on the left plot. The general 'random' trend that is observed is in alignment with an isotropic explosion.
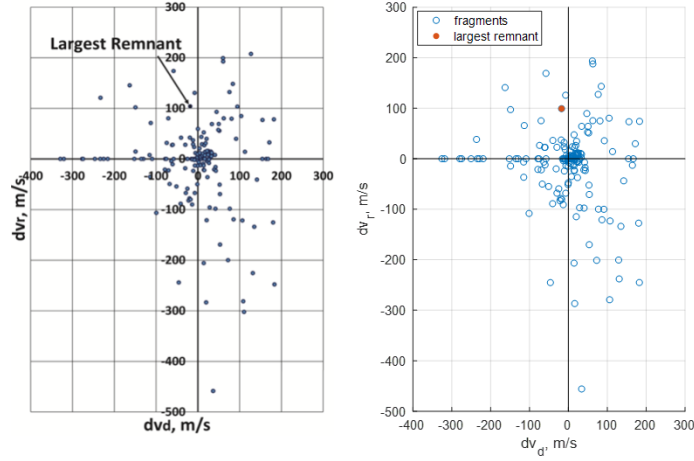
(a) NOAA-3: 2D plot of downrange vs. radial velocities of fragments.

(b) NOAA-3: 2D plot of cross-range vs. radial velocities of fragments.

(c) NOAA-3: 2D plot of cross-range vs. downrange velocities of fragments.

Figure 5.5. NOAA-3, 2D velocity distributions of fragments compared with [4] (left).
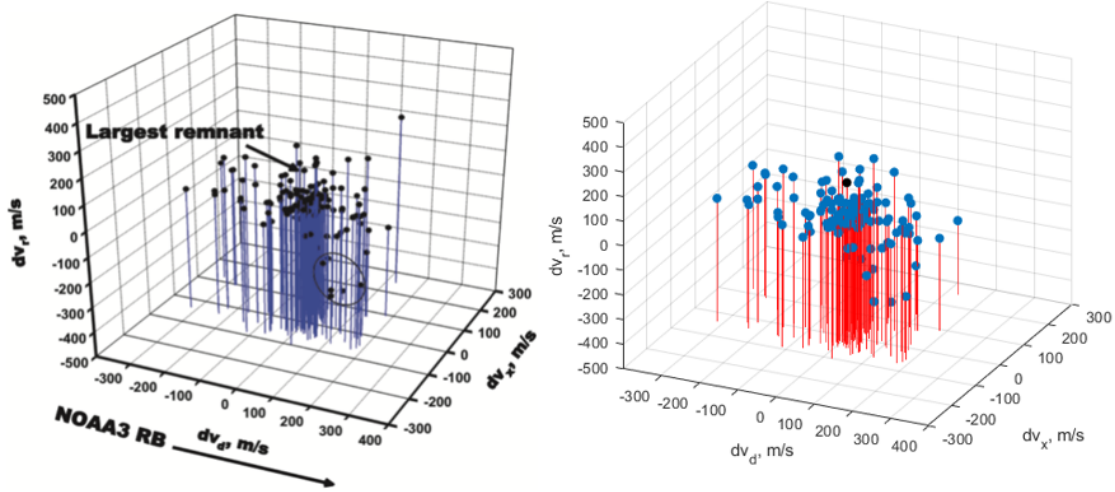
Figure 5.6. NOAA-3: 3D velocity distributions of fragments compared with [4] (left).

5.3.2 Spot-1

It must be noted that the replicated velocity plots are not in complete alignment with the reference plots – this is because considerably fewer fragments are used in this work. The overall trends observed are still similar.
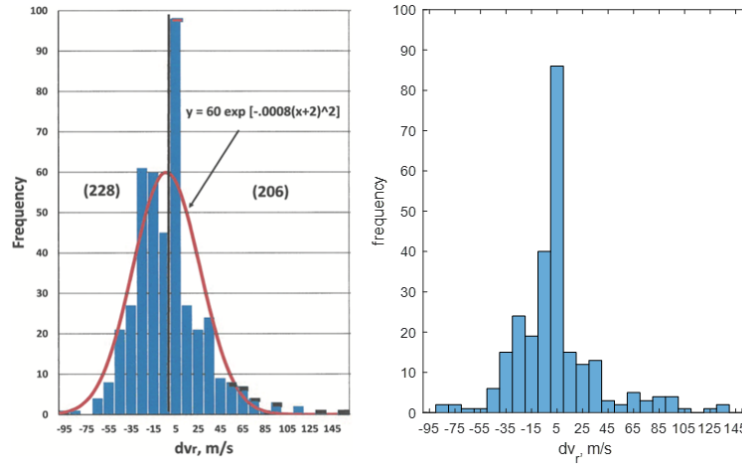
Fragment Velocity Frequencies:

Figure 5.7 shows the velocity perturbations on the fragments and their relative frequencies for the Spot-1 event. Diving into the actual velocity values, more fragments received negative dvd and dvx perturbations; interestingly an equal number of fragments (114) received positive and negative dvr perturbations. 38 fragments had indeterminate (complex) dvr perturbations and were assigned a value of 0. While the spread of velocities in not noticeably skewed, an interesting trend can be observed in the dvx distribution – quite a few fragments received high-velocity perturbations in the cross-range direction.
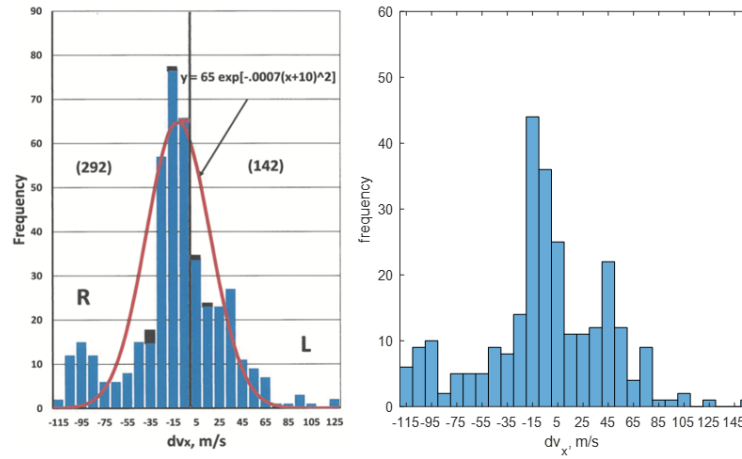
The dv plot in Figure 5.8 interestingly deviates from a typical exponential distribution – a large number of fragments possess high velocities (the highest frequency of fragments is in the 30-40 m/s range). The high dvx values may contribute to this trend.

73
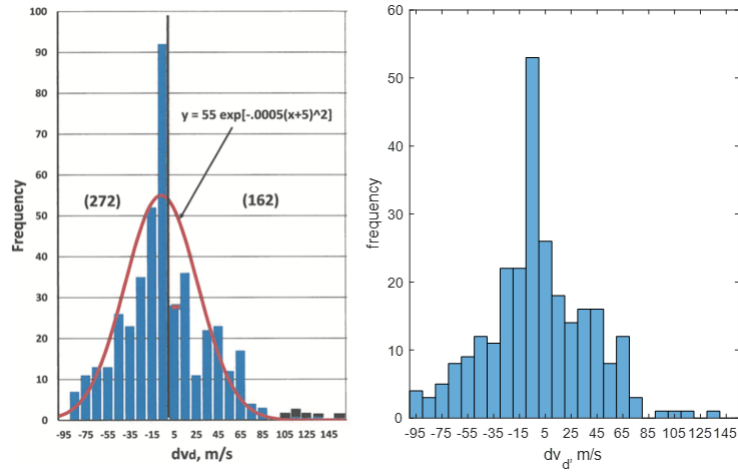
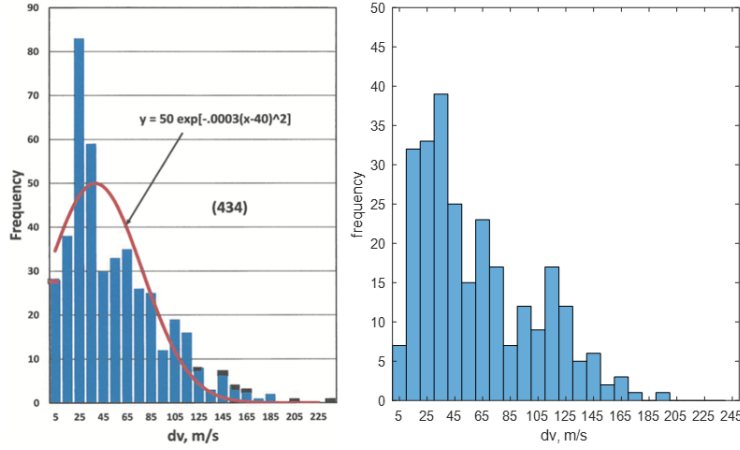(a) Spot-1: Downrange velocities of fragments.

(b) Spot-1: Radial velocities of fragments.

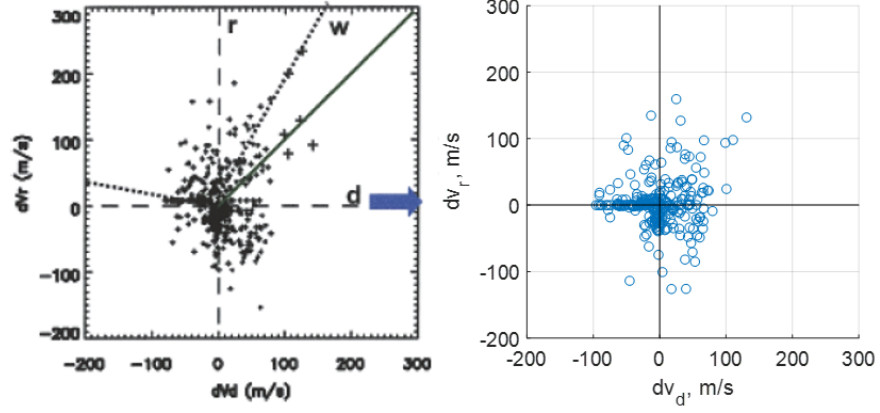(c) Spot-1: Cross-range velocities of fragments.

Figure 5.7. Spot-1: Velocity frequencies of fragments compared to [4] (left).

Figure 5.8. Spot-1: Total velocity perturbations of fragments compared to [4] (left).
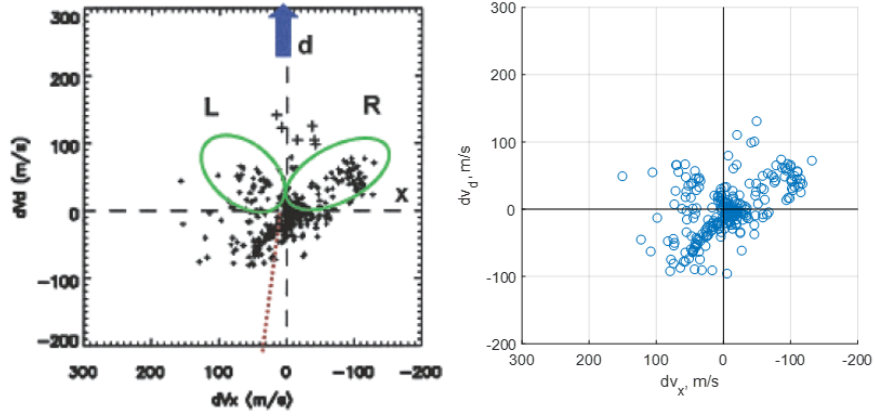
2D and 3D Fragment Velocity Distributions:

Figure 5.9 shows the velocity distributions in the 2D plane for the Spot-1 event. The high number of fragments clustered around the origin indicates that this is likely a low-velocity event. It is also worth noting the 'butterfly patterns' observed encircled in green in the left plots are not typical of explosions and may point towards an alternative cause. Additionally, 6 high-energy fragments are marked with '+' in the left plots. The 3D plot in Figure 5.10 affirms the 2D trends and shows a majority of the fragments clustered near the origin, with a few fragments possessing higher velocities. The high-energy fragments, believed to be ricochet fragments, are shown with '<>' in the left plot.

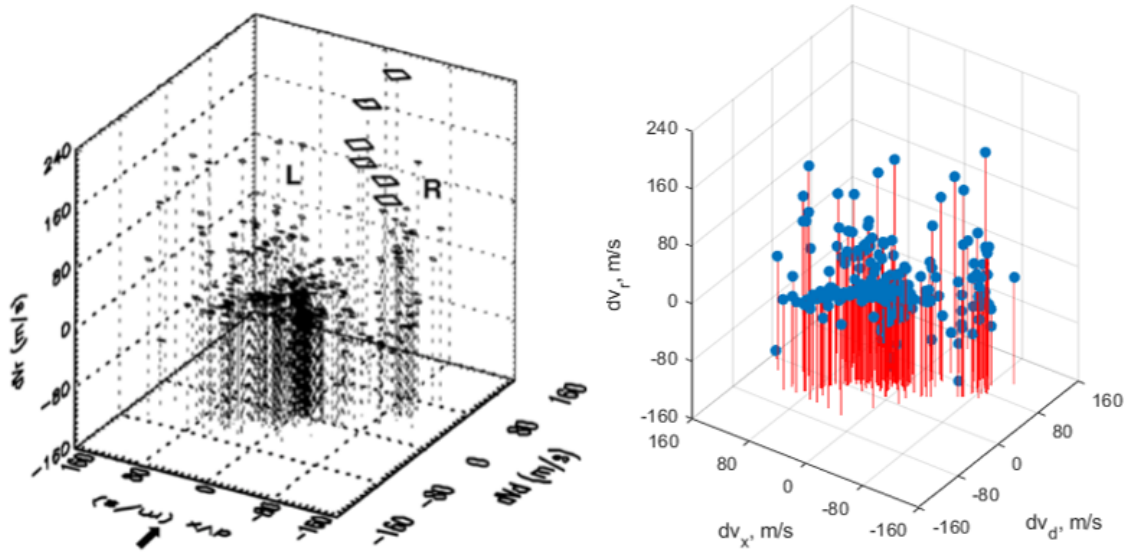(a) Spot-1: 2D plot of downrange vs. radial velocities of fragments.
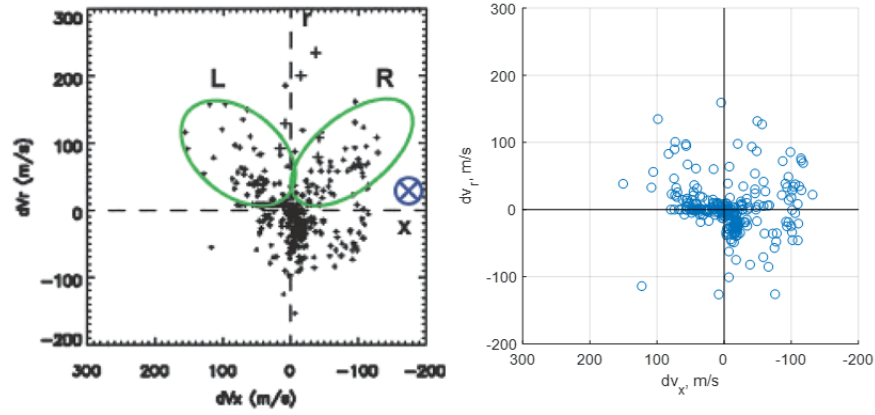
(b) Spot-1: 2D plot of cross-range vs. radial velocities of fragments.

(c) Spot-1: 2D plot of cross-range vs. downrange velocities of fragments.

Figure 5.9. Spot-1 2D velocity distributions of fragments compared to [4] (left).

Figure 5.10. Spot-1 3D velocity distributions of fragments compared to [4] (left).

5.4 Angular Perturbations

5.4.1 NOAA-3

The angular distribution of fragments shows an isotropic spread with no singular octant possessing an unusually large number of fragments. The largest fragment is shown in the top right of both the plots: circled in the reference plot (above) and shown in red in the replicated plot (below). Additionally, the six 'recoil fragments' with unusually large dvr perturbations are circled in quadrant VIII in the top plot. Five of these can also be observed in the replicated plot.
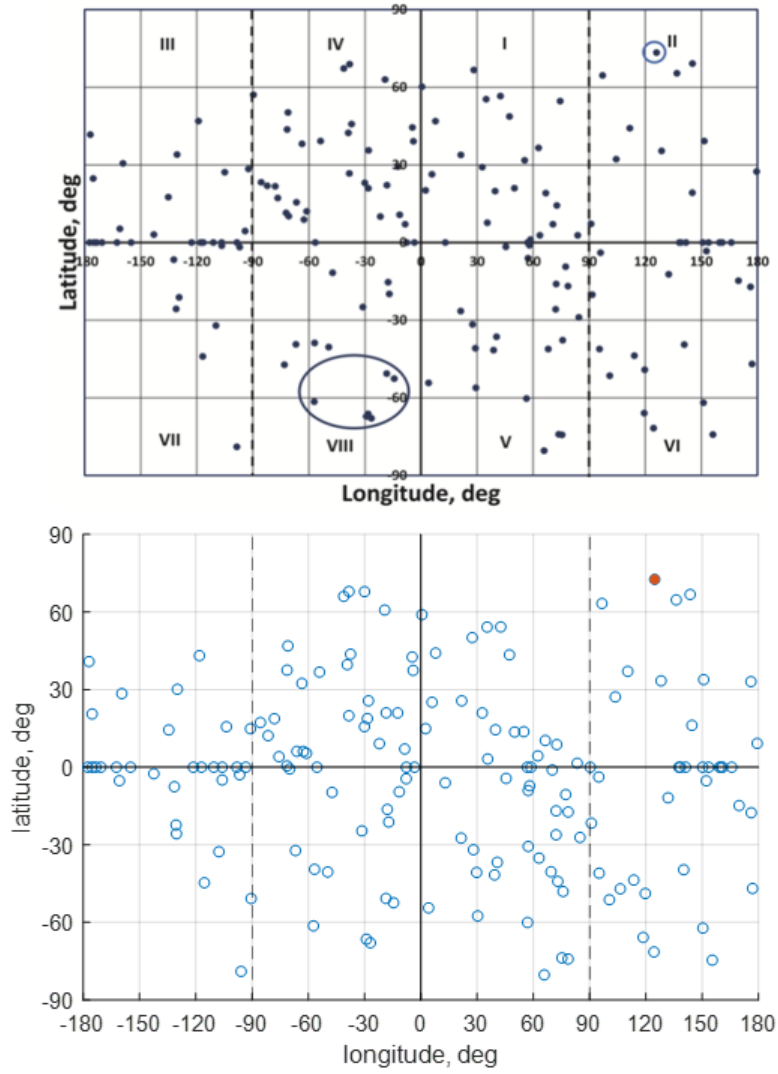
Figure 5.11. NOAA-3: Angular distribution of fragments compared to [4] (top).

5.4.2   Spot-1

Figure 5.12 shows the angular perturbations on the fragments of the Spot-1 event. An angular distribution has not been documented by [4], but one is presented here to uncover additional insights. This plot looks noticeably different from the distribution pertaining to the NOAA-3 RB; the bottom right of the plot is largely devoid of fragments, indicating about a quarter of the spherical projection is clear of fragments. This region could potentially be an impact zone (reminiscent of the Clam model if this is the only rupture point). Additionally, it is interesting to note that there is also a 'gap' in the chart on the top left corner, which is diametrically opposite the region devoid of fragments on the right – this opens up the possibility that an object may have pierced through the RB and exited on the other side; this is evocative of the Half-Segment model.
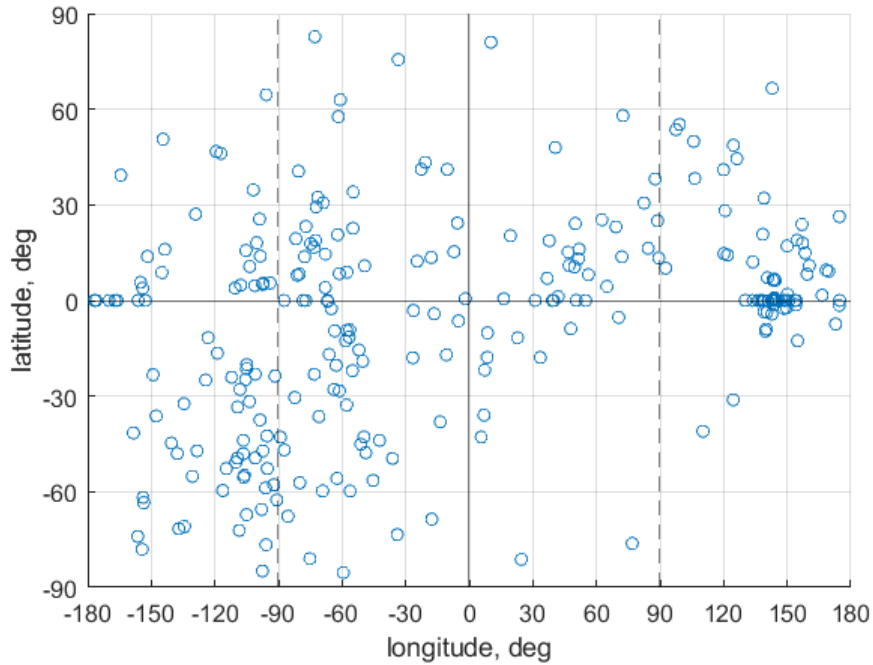
Figure 5.12. Spot-1: Angular distribution of fragments.

5.5 Event Intensity

The computed and reference ([4]) intensities of the two events in m^2/s^2 are shown in Table 5.2.

Table 5.2. Intensities of the NOAA-3 and Spot-1 events

Event	mean dv (m/s)	E (m^2/s^2)
NOAA-3	108.75	5913.28
NOAA-3 Ref.	107.77	5807.19
Spot-1	61.16	1870.27
Spot-1 Ref.	54.98	1511.40

The intensity computed for NOAA-3 is quite close to the reference values (the slight discrepancy likely arises from the fewer fragments used in the replication). The disparity amongst the Spot-1 values is expected given only about half as many fragments are used in the reproduction process compared to the reference ([4]).

It is evident that the Spot-1 event was far less energetic, with its average fragment velocities being almost half of those pertaining to the NOAA-3 event. Explosive fragmentations tend to have higher fragment velocities and thus intensities owing to their highly energetic nature. On the contrary, collisions, especially those with debris rather than full-size satellites, tend to result in lower intensity events; the velocity imparted onto an RB by a piece of debris is generally insufficient to result in a high energy event, which consist of fragments with high spreading speeds.

5.6 Fragmentation Hypotheses

5.6.1 NOAA-3

The isotropic spread of fragments and their relatively high spreading speeds point towards an explosive fragmentation in alignment with the Octant model as shown in Figure 4.10. It

is known that the cause of the event was due to combustion of leftover propellant – this type of rocket body explosion is prone to result in the Octant model.

5.6.2 Spot-1

The Spot-1 event is less straight-forward to dissect in comparison to the NOAA-3 event – the fragment distribution is far less isotropic, particularly evident in the angular perturbations plot in Figure 5.12. It is also worth noting that unlike the Delta upper stages, the Ariane RB used cryogenic propellants and contained safety valves to prevent over-pressurization [40] – a propulsion-based event is thus unlikely.

Additionally, the low spreading speeds of the fragments are indicative of a collision, but with a small object – it was also verified that no cataloged satellite was in the vicinity of the Spot-1 RB near the time of its breakup. The altitude region of the RB (around 800 km) is known to have the "highest spatial density of orbiting population" [42]; a collision with an untracked object in this region is thus relatively likely.

6. CENTAUR RESULTS

This section presents the results from the application of fragmentation theory (Chapter 4) on three Centaur upper stage fragmentation events of interest. [43], a conference paper written by the author of this thesis, is heavily referenced.

6.1 Background

The three events were discovered based on measurements by the International Scientific Optical Network (ISON) and the Roscosmos Automated Warning System on Hazardous Situations in Outer Space (ASPOS OKP).

All three of the fragmented objects are identical Centaur upper stages launched on the Atlas V launch vehicle operated by United Launch Alliance. The Centaur upper stages are of the Single-Engine Centaur (SEC) variant with a Pratt & Whitney RL10A-4-2 engine, using liquid oxygen and liquid hydrogen as propellant [44] – an image of one is shown in Figure 6.1. Each of the Centaur stages successfully placed US military communications satellites into Geostationary Transfer Orbits (GTO), ultimately possessing highly elliptical orbits (HEO) with relatively high perigees. The body of the Centaur is relatively large: it has a length of 12.68 m, a diameter of 3.05 m, and a dry mass of 2243 kg [45]. This is about twice the size of the Delta upper stages (includes the NOAA-3 event, discussed in Chapter 5), which famously exploded in the 1970s. Agapov and Savin found that debris resulting from the three events has increased the number of all HEO and Medium Earth Orbit (MEO) objects catalogued by 2698 – this is over 31 percent of the HEO and MEO population [46]. The breakup dates calculated by them, along with information regarding the orbits of the three parent objects are summarised in Table 6.1.

Figure 6.1. Atlas V Centaur Upper Stage [47].

Table 6.1. Key facts surrounding the Centaur upper stage events

	Event 1 (2009-047B)	Event 2 (2014-055B)	Event 3 (2018-079B)
SSN	35816	40209	43652
Breakup date	24th Mar 2019	30th Aug 2018	6th Apr 2019
Payload	USA-207	USA-257	USA-288
Orbit (km)	34700 x 6675	35180 x 8202	35092 x 8526
Inclination (deg)	23.1	22.2	12.2

The 2009-047B event is particularly interesting – it was found by [35] to result in fragments with very low velocities (later confirmed in Section 6.5.1). Small-sized fragments were also few in number, which is in contradiction to existing fragmentation models.

For ease of discussion, 2009-047B will henceforth be referred to as Event 1, 2014-055B as Event 2, and 2018-079B as Event 3.

6.2 Data Sources

Fragment sets from three data sources are used to investigate the Centaur events – Astronomical Institute of the University of Bern (AIUB), the Vimpel catalog (Section 2.3.2), and the Spacetrack catalog (Section 2.3.1).

AIUB has long-standing scientific collaborations with International Scientific Optical Network (ISON), the Keldysh Institute of Applied Mathematics, Moscow, and the Astronomical Scientific Center, Moscow, and observation data is regularly exchanged with them. In the context of this collaboration, colleagues in Russia timely informed AIUB about these three events and provided orbital elements for the discovered fragments. Since October 2018, AIUB has been performing observations with the ESA 1-m telescope at Tenerife, on behalf of ESA, along with its sensors – the Swiss Optical Ground Station and the Geodynamics Observatory Zimmerwald, Switzerland – these observations are to characterize debris clouds and maintain an orbit catalogue for a subset of the fragments associated with the events. Further information regarding the survey strategy used by the observational campaign is found [35].

The number of fragments catalogued by each source for the three events are summarized in Table 6.2.

Table 6.2. Number of fragments catalogued by AIUB, Vimpel, and Spacetrack

	Event 1 (2009-047B)	Event 2 (2014-055B)	Event 3 (2018-079B)
AIUB	725	676	907
Vimpel	81	208	187
Spacetrack	1	69	55

Data obtained from AIUB contained ephemerides of the fragments pertaining to February 2020. This is about 10 months after Events 1 and 3, and 1.5 years after Event 2.

The fragments were catalogued in the Vimpel catalog just over a week after each of the events.

TLEs from USSTRATCOM were obtained from space-track.org. Only a single fragment,

which inherited the parent object's international designator, has been catalogued for Event 1. Interestingly, 2009-047B's first appearance in the Spacetrack catalog is on 3rd April 2019 (10 days after the event), with no data on the pre-event parent object available. For Events 2 and 3, fragments appeared in the catalog 5 and 7 months after each event, respectively. Similar to Event 1, the first appearance of 2014-055B in the catalog was after the event, on 24th January 2019 (about 4 months after the breakup).

A note on terminology: 'parent' or 'pre-event parent' refers to the parent objects prior to the fragmentations. 'Parent remnant' is used to refer to the most significant fragment resulting from each event for the AIUB data. For the Vimpel data, this remnant is assumed to be the fragment with the lowest AMR value; for the Spacetrack data, the object which inherited the parent's international designator is assumed to be the parent remnant.

6.3 Breakup Epoch

The breakup epochs for the three events are calculated using the method described in Section 4.1.2 – the fragments are propagated backwards to an epoch at which they are at their closest. Table 6.3 shows the breakup times calculated for each of the three events. Entries marked with '*' correspond to the breakup date calculated in [46].

Table 6.3. Breakup times for the three events corresponding to data sources.

	AIUB	Vimpel	Spacetrack
Event 1	~12:00, 3rd Apr 2019	3:33, 24th Mar 2019*	-
Event 2	17:14, 30th Aug 2018*	22:04, 30th Aug 2018*	20:40, 30th Aug 2018*
Event 3	~15:00, 7th Apr 2019	18:57, 6th Apr 2019*	16:43, 6th Apr 2019*

The tabulated breakup times are those arising from the linear distance function measuring distances relative to the pre-event parent, as was found to be most useful in the validation cases discussed in Section 5.

The breakup epoch calculation is sensitive to three main factors – firstly, how recent the data is to the fragmentation event (data closer to the event will require less propagation and is

thus less prone to error accumulation). Secondly, if the pre-event parent data is available (the breakup algorithm performs best when the fragment distances are measured relative to the pre-event parent). Lastly, the number of fragments used. This is relevant when fragments are added to the catalog sporadically, as in the case of the Spacetrack catalog. If only a handful of fragments are added a week after the breakup, while the remaining fragments are added a few months after, using all of the data is more favorable since the benefit of having more data points outweighs the disadvantage stemming from longer propagation. Conversely, it is also possible that a large fragment data set may include outliers which could skew mean distances. This factor, along with the long propagation times for the AIUB fragments may point to the discrepancy in the breakup dates for Event 1 and Event 3 for the AIUB data. An additional factor which may have contributed to the inaccurate breakup epoch (by about 10 days!) found for Event 1 when using the AIUB data is the nature of the event itself – the fragments pertaining to this event received very small velocity perturbations and thus remained in a cluster. The closeness of the fragments well after the event may have contributed to the distance function arriving at an incorrect breakup epoch.

For subsequent analysis, Vimpel breakup times are used due to their alignment with [46]. Regardless, it is found that when slightly different breakup epochs are used (within 1-2 hours of a time), there is not a significant change in the results – while individual fragment velocities may change, the overall distributions remains largely the same. This is demonstrated in Section A.3, where results pertaining to Event 2 are shown for a breakup time of 23:04 on 30th Aug 2018, which is an hour past the Vimpel breakup time.
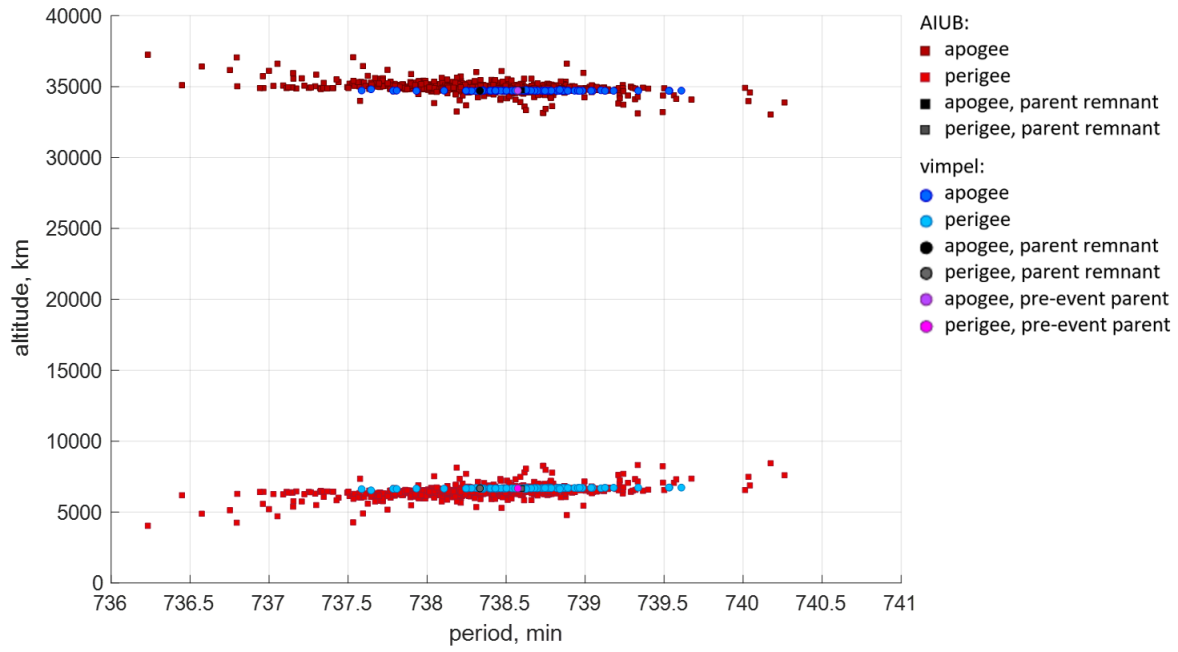
6.4   Gabbard Diagram

The Gabbard Diagrams for the three events are presented in this section. In contrast to the 'X' shape distribution of fragments observed in the Gabbard plots for the NOAA-3 and Spot-1 events in Section 5.2, the plots for the Centaur events should two non-intersecting lines, which is characteristic of the elliptical orbits the objects were in.

6.4.1 Event 1 (2009-047B)

Note that Spacetrack fragments are not shown since only one has been catalogued. The Gabbard diagram for Event 1, shown in Figure 6.2 is rather interesting; the fragments appear to have received a relatively small impulse as can be inferred from the small range in periods and the apogee/perigee altitudes. In fact, this is the smallest range of periods that has been observed in this thesis (event compared to the Delta upper-stages and the Spot-1 events). The horizontal spread of the fragments is roughly even on both sides of the pre-event parent for the Vimpel data, but the AIUB fragments are mostly to the left of the parent. This suggests that a considerable amount of AIUB fragments slowed down in their orbits. It is interesting to note that fragments in the Vimpel catalog received minimal radial velocity perturbations, as inferred from the near-straight apsidal lines. Three outliers from the AIUB data with significantly larger periods are omitted from this Gabbard plot. The velocity perturbations of these fragments are covered in Section 6.5.1. The parent object for Event 1 was ascending, denoting the Forbidden Zone is between the apsidal lines – this region has a clear dearth of fragments, suggesting minimal drag effects took place on the fragments.

6.4.2 Event 2 (2014-055B)

The Gabbard diagram for Event 2, shown in Figure 6.3, is more conventional (for elliptical orbits) than that for Event 1, spanning larger ranges of both apogee/perigee altitudes and periods. The three data sources (AIUB, Vimpel, and Spacetrack) appear to be in accordance with each other. The prominent spread of AIUB fragments away from the apsidal lines suggests high radial velocities. A number of fragments (mostly AIUB and a few Vimpel) possess high periods upwards of 900 minutes – these fragments received large positive downrange impulses and thus sped up considerably along the orbit. The parent object pertaining to Event 2 was descending in its orbit – the Forbidden Zone thus lies outside of the apsidal lines. While most of the fragments lie in between the lines, the handful that are above the apogee line and below the perigee line are affected by drag effects.

Figure 6.2. Event 1 (2009-047B), Gabbard diagram of fragments.
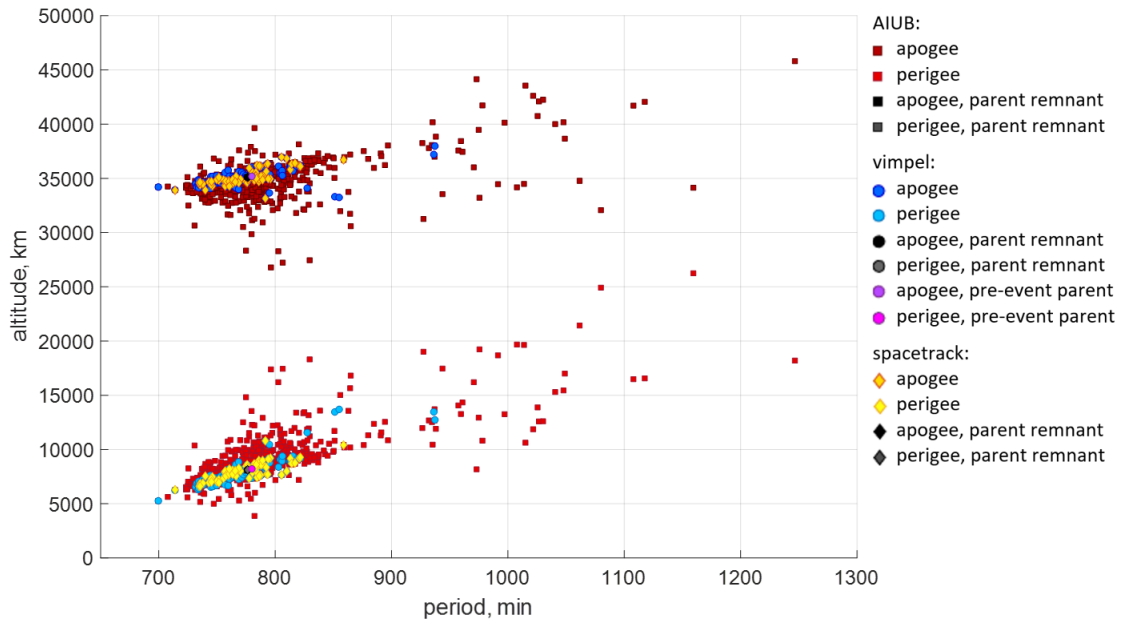
Figure 6.3. Event 2 (2014-055B), Gabbard diagram of fragments.
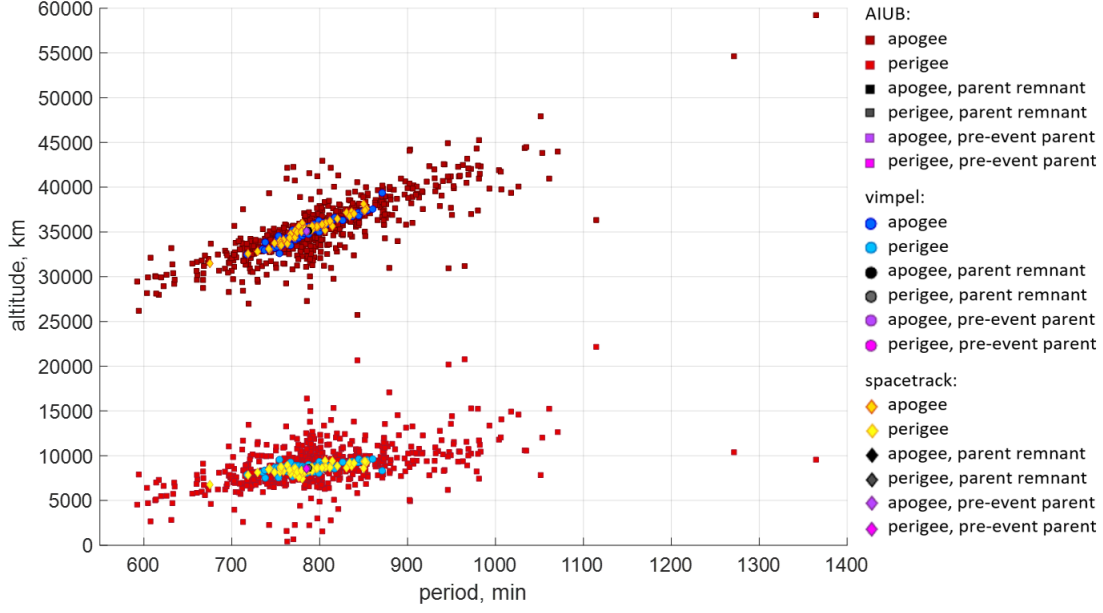
Figure 6.4. Event 3 (2018-079B), Gabbard diagram of fragments.

6.4.3 Event 3 (2018-079B)

The Gabbard diagram for Event 3 is shown in Figure 6.4. The Vimpel and Spacetrack data appear to be closely aligned, with the AIUB fragments extending around them, roughly symmetrically. This Gabbard plot covers the broadest ranges of periods and altitudes (compared to the other Centaur events as well as those used for validation), suggesting this may be the highest intensity event studied in this thesis. The immense extension of the AIUB fragments both vertically and horizontally along the two apsidal lines once again points towards high velocity perturbations encountered by these fragments. The parents for the three data lie very close together, roughly in the middle of the cluster; this may point towards a roughly isotropic fragmentation. All three of the parent remnants are situated in proximity to the parents, suggesting they received minimal perturbations following the event. The forbidden zone for this event is above the apogee line and below the perigee line (the parent was descending) – A number of fragments appear to be in this region, indicating possible drag effects.

6.5   Velocity Perturbations

Due to the nature of the velocity equations discussed in Section 4.3, some fragments may have indeterminate radial velocities when their eccentricities are too small (complex values arise from the square root). The plane-change angle, ζ, is complex when the latitude of fragmentation exceeds the inclination, resulting in indeterminate downrange and cross-range velocities. This was the case with Event 3, with a significant number of fragments resulting in indeterminate downrange and cross-range velocities at the breakup time of 18:57, 6th April 2019. By slightly changing the breakup time on the same date (19:12 for Vimpel fragments, 19:28 for Spacetrack fragments, and 20:21 for AIUB fragments), the fragment velocities were determinable. While specific values of the velocity and angular perturbations change for different breakup times, broader trends remain the same and are still useful for the purpose of this investigation. Additionally, Events 1 and 2 did not have a pre-event parent catalogued by AIUB or Spacetrack; the parameters pertaining to the Vimpel parent object for the events were used instead to calculate perturbations on the fragments. While pre-event parent information was available for both Spacetrack and Vimpel for Event 3, for consistency, the parameters pertaining to the Vimpel parent were used once again; the Vimpel states at the breakup epoch are also likely more accurate given the recency of the ephemeris data.

6.5.1   Event 1 (2009-047B)

Fragment Velocity Frequencies:

Figure 6.5 shows the velocity perturbations on the fragments and their relative frequencies for Event 1. Most of the fragments have very low velocity perturbations in the downrange and cross-range directions, the former mostly ranging 0-50 m/s (backward for AIUB and forwards for Vimpel) and the latter, 0-25 m/s (mostly downwards). While the Vimpel fragments follow the same cross-range trend as the AIUB fragments, they seem to be moving in opposite directions in both the downrange and radial components. Interestingly, the AIUB fragments appear to have a wide range of radial velocities (in comparison to the other two components), with the majority of the fragments being perturbed radially outwards, unlike

the radially inward perturbations of the Vimpel fragments. The three outliers, mentioned in section 5.1, have the following significant downrange and cross-range velocities respectively: 1. 906 m/s, - 170 m/s, 2. 1031 m/s, 306 m/s, 3. 1095 m/s, -129 m/s. The radial velocities for these fragments are indeterminate due to their near-zero eccentricities. Figure 6.6 is interesting as it departs from the typically exponential trend of fragment velocities that has been seen in prior explosive fragmentation events (such as the NOAA-3 distribution in Figure 5.4). Instead of the highest number of fragments possessing velocities in the lowest range, more of the AIUB fragments have slightly larger velocities, totalling 50-100 m/s. All of the Vimpel fragments are contained in the 0-50 m/s range.
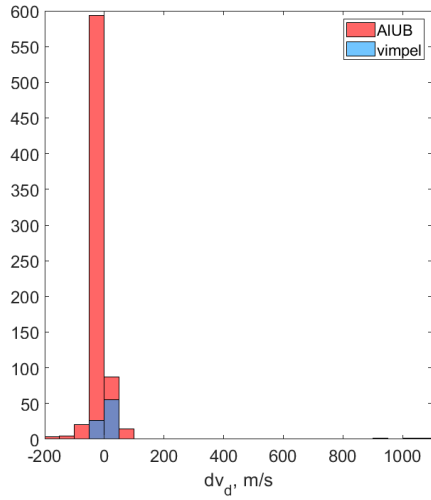
(a) Event 1 (2009-047B): Downrange velocities of fragments.
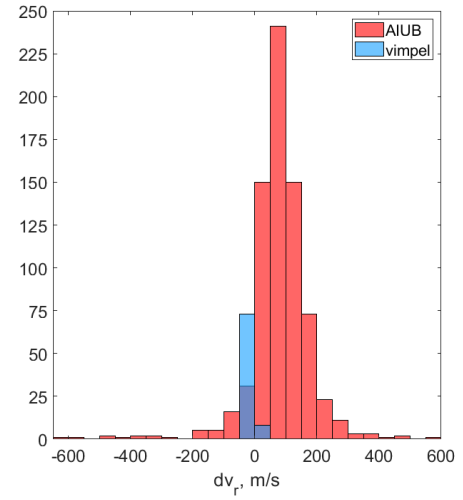
(b) Event 1 (2009-047B): Radial velocities of fragments.
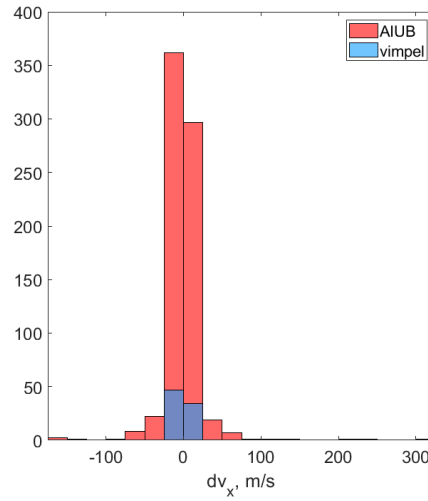
(c) Event 1 (2009-047B): Cross-range velocities of fragments.

Figure 6.5. Event 1 (2009-047B), Velocity frequencies of fragments.
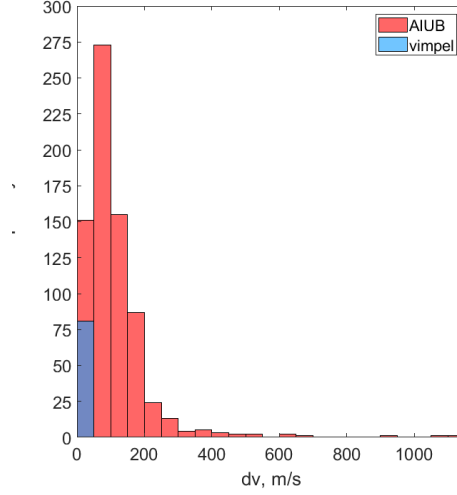
Figure 6.6. Event 1 (2009-047B), Total velocity perturbations of fragments.

2D and 3D Fragment Velocity Distributions:

Figure 6.7 shows the velocity distributions in the 2D plane. It is immediately evident that both the AIUB and Vimpel parent remnants encountered very small perturbations, both lying close to the origin. The AIUB fragments form almost a linear pattern in the dvd-dvr plot; fragments with higher radial velocities tend to have higher downrange velocities for this event. While the dvx-dvd plot is fairly isotropic in nature, the other two plots indicate a high number of AIUB fragments possess large positive radial velocities. The 3D plot in Figure 6.8 reiterates these observations and emphasizes the radially outward perturbation on the AIUB fragments. Conversely, the Vimpel fragments are mostly perturbed radially inwards. The parent remnants are obscured by the other fragments in the 3D plot but are located close to the origin.
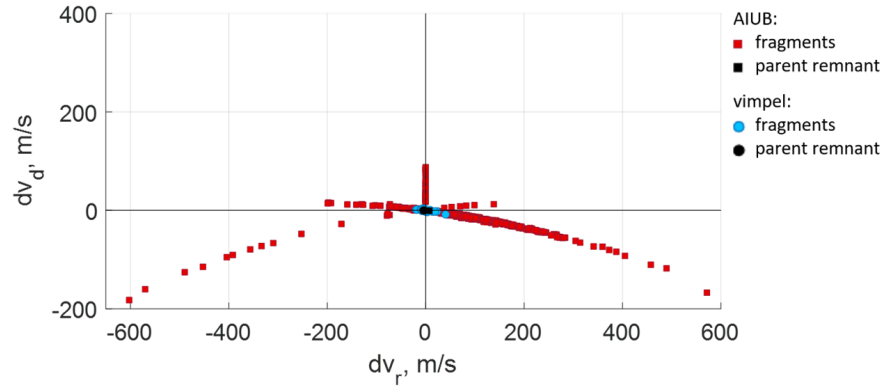
(a) Event 1 (2009-047B): 2D plot of downrange vs. radial velocities of fragments.
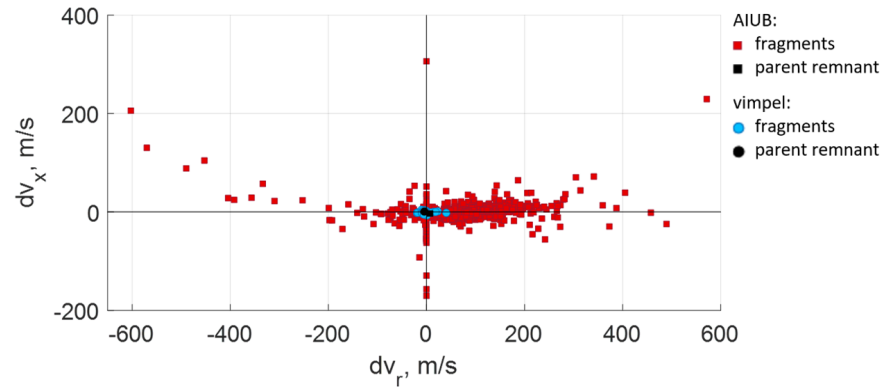
(b) Event 1 (2009-047B): 2D plot of cross-range vs. radial velocities of fragments
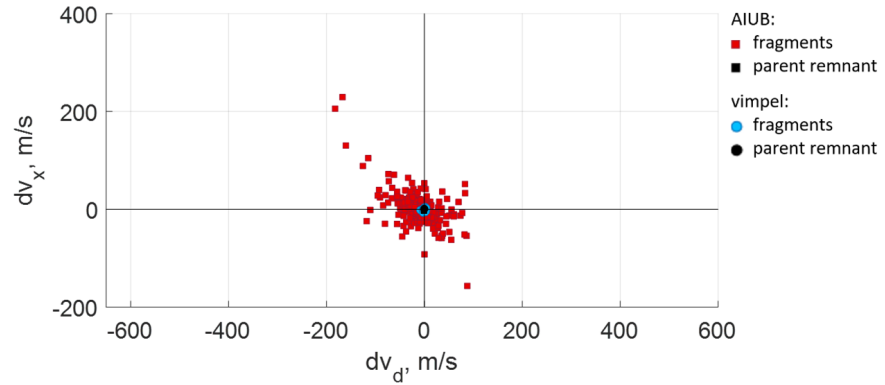
(c) Event 1 (2009-047B): 2D plot of cross-range vs. downrange velocities of fragments

Figure 6.7. Event 1 (2009-047B), 2D velocity distributions of fragments
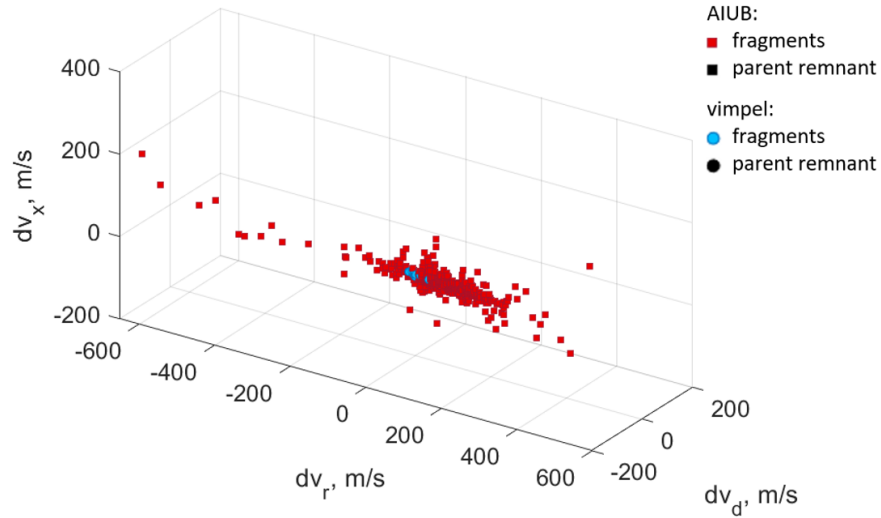
Figure 6.8. Event 1 (2009-047B), 3D velocity distributions of fragments.
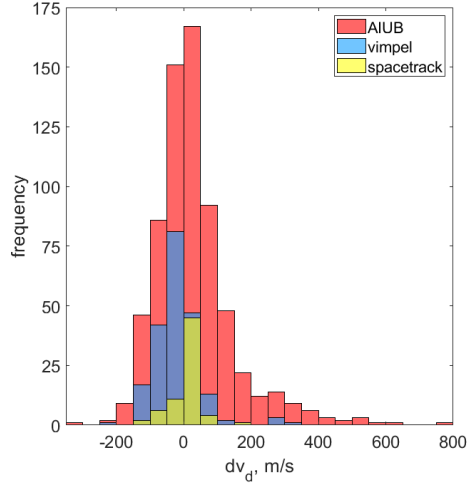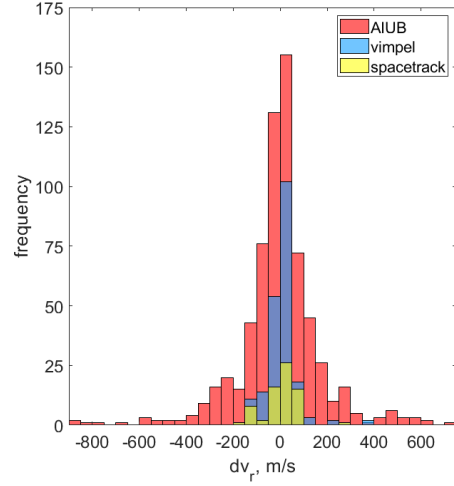
6.5.2 Event 2 (2014-055B)

Fragment Velocity Frequencies:

Figure 6.9 shows the velocity perturbations on the fragments and their relative frequencies for Event 2. It must be noted that 31 fragments of Spacetrack produced indeterminate dvd and dvx values, which were thus replaced with 0, likely skewing the Spacetrack distributions. AIUB, Vimpel, and Spacetrack fragments appear to be mostly in agreement in the velocity ranges for the downrange and radial components. AIUB data indicates more fragments sped up along the orbit while the Vimpel data indicates otherwise, with the same speed range of 0-50 m/s. All three data point towards more fragments with radially outward behaviour with speeds of 0-50 m/s. The cross-range velocities are rather interesting, with Vimpel fragments showing an almost equal upward and downward perturbation. Slightly more Vimpel fragments possess speeds ranging 0-25 m/s directed upward; Most of the Spacetrack fragments also lie in this low-velocity range. AIUB fragments appear to have received a significantly stronger perturbation upwards, with most of the velocities in the 75-125 m/s range.

The dv plot in Figure 6.10 shows that both AIUB and Spacetrack fragments depart from an exponential distribution; more AIUB fragments are found in the 100-150 m/s range, while

most (measurable) Spacetrack fragments are found in the 50-100 m/s range. The Vimpel fragments followed the more conventional exponential distribution with a high number of fragments possessing low speeds of 0-50 m/s. The deviation of the AIUB and Spacetrack fragments from an exponential distribution is reminiscent of the dv plot pertaining to the Spot-1 event in Figure 5.8, albeit the velocity ranges of Event 2 are notably higher.
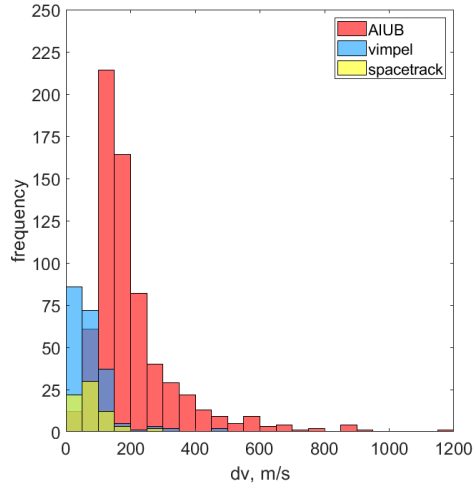

(a) Event 2 (2014-055B): Downrange velocities of fragments.

(b) Event 2 (2014-055B): Radial velocities of fragments.
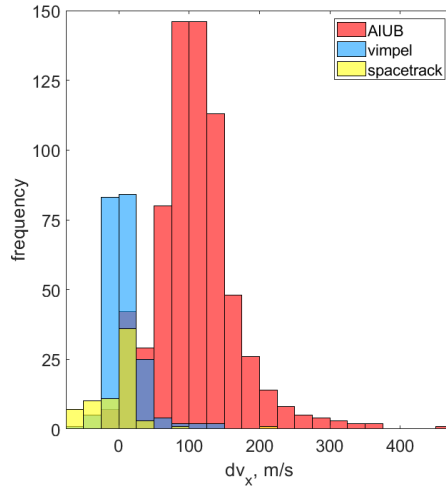
(c) Event 2 (2014-055B): Cross-range velocities of fragments.

Figure 6.9. Event 2 (2014-055B): Velocity frequencies of fragments.

Figure 6.10. Event 2 (2014-055B), Total velocity perturbations of fragments.

2D and 3D Fragment Velocity Distributions:

Figure 6.11 shows the velocity distributions in the 2D plane for Event 2. The alignment of the downrange and radial velocities of the three data is reiterated in the dvd-dvr plot in Figure 6.11a. The distribution is fairly isotropic and the parent remnants are located in the centre. Interestingly, the AIUB fragments seem to form a 'butterfly pattern' similar to one seen in the Spot-1 event (Figure 5.9). As in the case of Event 1, the parent remnants received very small dvd and dvr perturbations. The AIUB data contains a significant amount of dvx fragments that stray away from the Vimpel and Spacetrack clusters, particularly evident in Figure 6.11c. Additionally, the AIUB parent remnant appears to have received a large upward perturbation and is situated amid its fragment cluster.

The 3D plot in Figure 6.12 shows the AIUB and Vimpel fragments as two distinct clusters. The Spacetrack appear to be interspersed between the Vimpel fragments. The AIUB fragments cover a significantly larger range of velocities as can be inferred from the visual spread of the data.
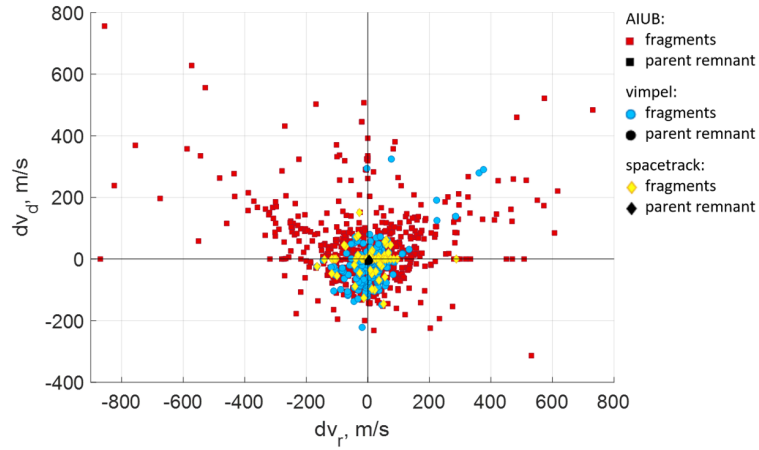
(a) Event 2 (2014-055B): 2D plot of downrange vs. radial velocities of fragments.
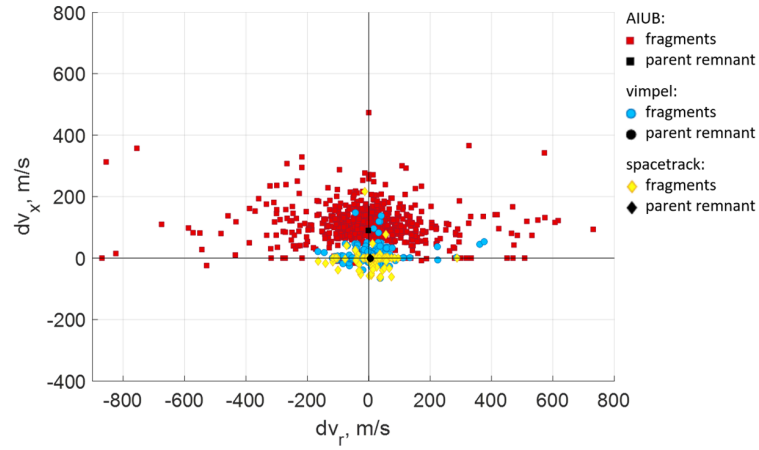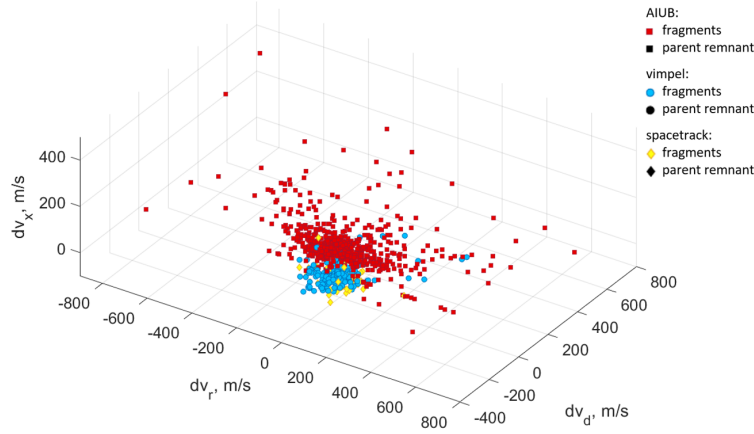

(b) Event 2 (2014-055B): 2D plot of cross-range vs. radial velocities of fragments.
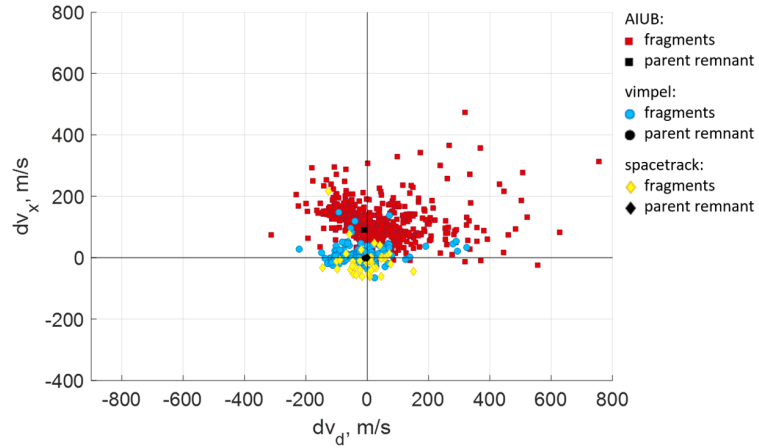
(c) Event 2 (2014-055B): 2D plot of cross-range vs. downrange velocities of fragments.

Figure 6.11. Event 2 (2014-055B), 2D velocity distributions of fragments.

Figure 6.12. Event 2 (2014-055B), 3D velocity distributions of fragments.
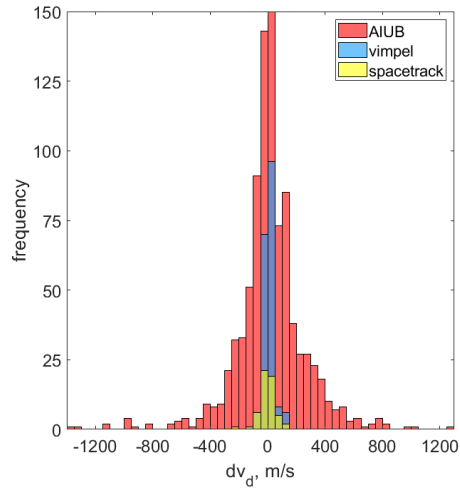
6.5.3 Event 3 (2018-079B)

Fragment Velocity Frequencies:

Figure 6.13 shows the velocity perturbations on the fragments and their relative frequencies for Event 3. Though the velocity ranges fro these plots are a lot higher, the general distribution is quite reminiscent of the NOAA-3 event, which showed isotropic fragment dispersal (Figure 5.3). All three data sources point to roughly isotropic distributions in the downrange and cross-range directions. Both the AIUB and Vimpel fragments indicate a slightly more positive downrange trend; more than half of the fragments sped up along their orbits. Spacetrack data shows the converse trend but is also fairly isotropic. The downrange and radial trends for both the AIUB and Vimpel data are similar, with more fragments possessing positive velocities; conversely, the Spacetrack fragments favour slightly negative velocities. It can be noted that a few AIUB fragments significant radial perturbations both inwards and outwards at velocities around 2 km/s. The cross-range plot is not isotropic in nature for all three data. Both AIUB and Spacetrack point towards a high number of fragments with negative, downward velocities. On the other hand, most of the Vimpel fragments have positive, upward velocities. The range of these cross-range perturbations is notably smaller for the AIUB fragments. Most fragments are contained in the 0-50 m/s range.

The dv plot shown in Figure 6.14 is quite interesting when the magnitude of the velocities are

considered. Many AIUB fragments have significantly higher velocities compared to Events 1 and 2, as well as the NOAA-3 and Spot-1 events; this was first evident in the extensive horizontal distribution of fragments in the Gabbard diagram. Vimpel and Spacetrack fragments follow an exponential distribution with high-velocity fragments being low in number. AIUB fragments slightly depart from this trend, with a high frequency of fragments lying in the 50-100 m/s range; relative to Events 1 and 2, Event 3 is closest to possessing an exponential fragment velocity distribution. This is evocative of an explosive fragmentation event, as was observed for the dv plot pertaining to NOAA-3 (Figure 5.4).
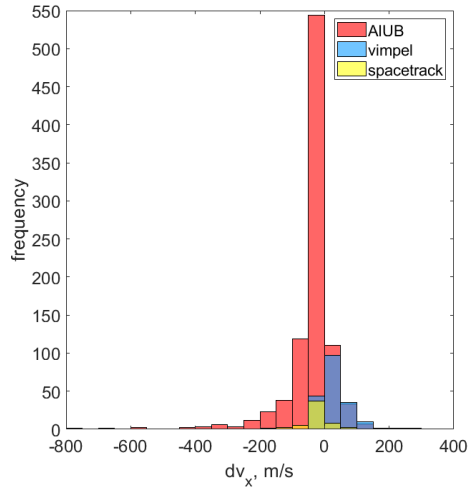
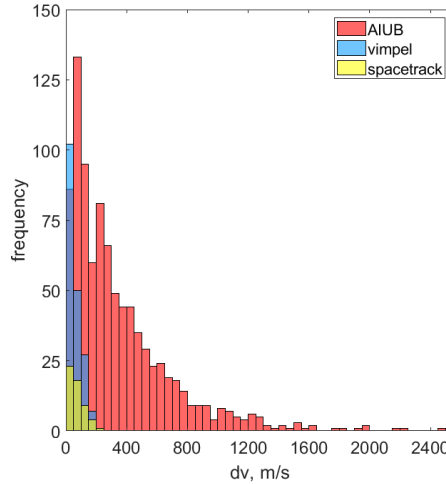(a) Event 3 (2018-079B): Downrange velocities of fragments.
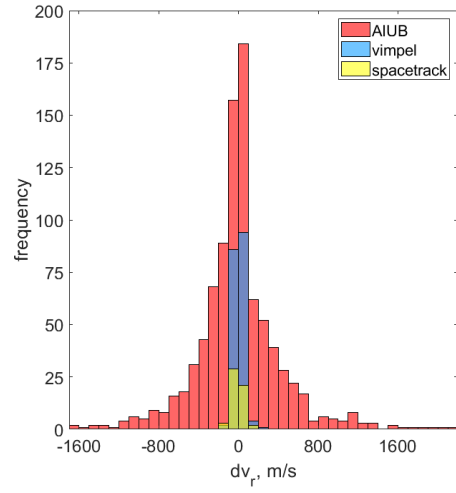
(b) Event 3 (2018-079B): Radial velocities of fragments.

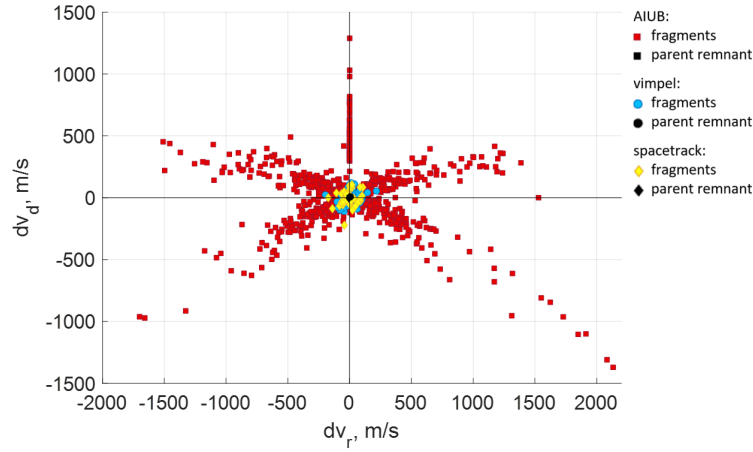(c) Event 3 (2018-079B): Cross-range velocities of fragments.

**Figure 6.13.** Event 3 (2018-079B), Velocity frequencies of fragments.

Figure 6.14. Event 3 (2018-079B), Total velocity perturbations of fragments.

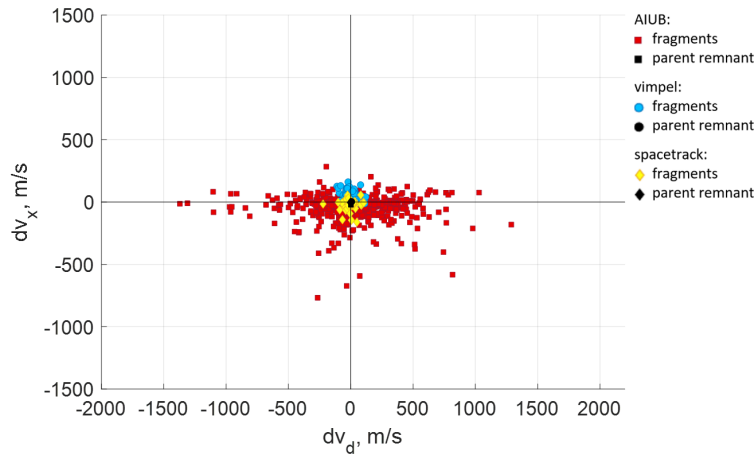## 2D and 3D Fragment Velocity Distributions:

Figure 6.15 shows the velocity distributions in the 2D plane. It is immediately evident that both the parent remnants encountered very small perturbations. The dvd-dvr plot is curious – while the symmetry of the fragment spread points towards an explosive fragmentation, the clearly defined 'X' shape is rather unique and has not been previously encountered in this study. The other two plots are symmetric as well – however, the high number of AIUB fragments possessing disproportionately large radial velocities (relative to their dvx and dvd velocities) is perplexing. The 3D plot in Figure 6.16 reiterates these observations and emphasizes the significant radial perturbations on the AIUB fragments. It is also interesting to note that the Vimpel fragments were shifted in the positive dvx direction, while the AIUB fragmnets were generally shifted downwards. The parent remnants are obscured by the other fragments in the 3D plot but are located close to the origin.

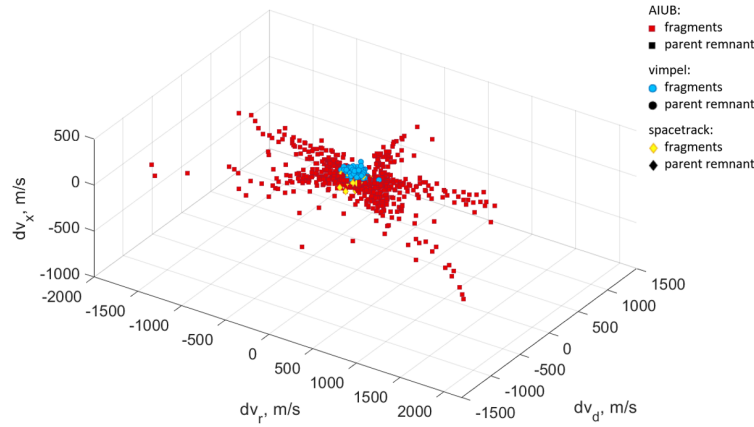(a) Event 3 (2018-079B): 2D plot of downrange vs. radial velocities of fragments.
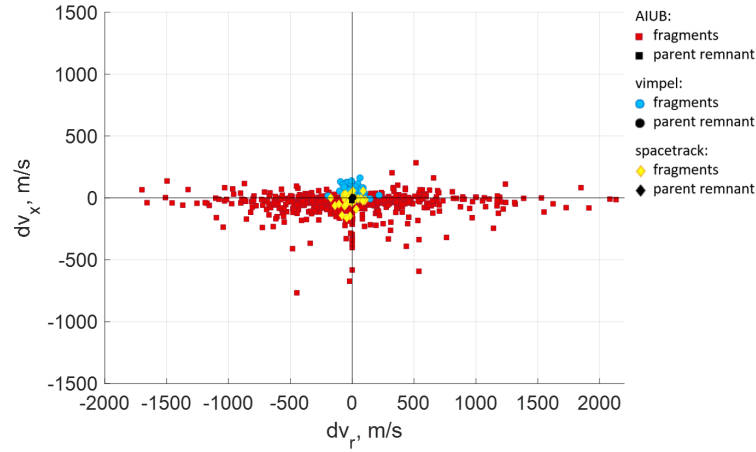
(b) Event 3 (2018-079B): 2D plot of cross-range vs. radial velocities of fragments.

(c) Event 3 (2018-079B): 2D plot of cross-range vs. downrange velocities of fragments.

**Figure 6.15.** Event 3 (2018-079B), 2D velocity distributions of fragments.

Figure 6.16. Event 3 (2018-079B), 3D velocity distributions of fragments.

6.6 Angular Perturbations

6.6.1 Event 1 (2009-047B)

Figure 6.17 shows the angular distributions of the fragments. There appears to be a clear 'arch' pattern displayed by both the AIUB and Vimpel fragments. The parent remnants are situated close to the edges of the fragment distributions for both data. The clustering of fragments in this manner is reminiscent of the Clam model (Figure 4.10). Events characterized by this model have a single rupture point, with most of the fragments emerging on the opposite side of this location. Nearly half the fragments in a Clam event are confined within a fifty-degree cone angle. In the case of Event 1, both data occupy only about a quarter of the surface projection, which is a lot smaller of a section than customary for Clam events, suggesting this may be a variation of one. The rupture location is typically located in the octant diametrically opposite the octant with the most number of fragments. In this case, the 'streak'-like arrangements of the fragments suggest that the rupture point may be in the form of a lengthwise crack as opposed to a circular perforation. Expectedly, this fragment distribution looks very different from those pertaining to the NOAA-3 (5.11) and Spot-1 (5.12) events, which likely followed the Octant and Half-Segment models respectively.

104
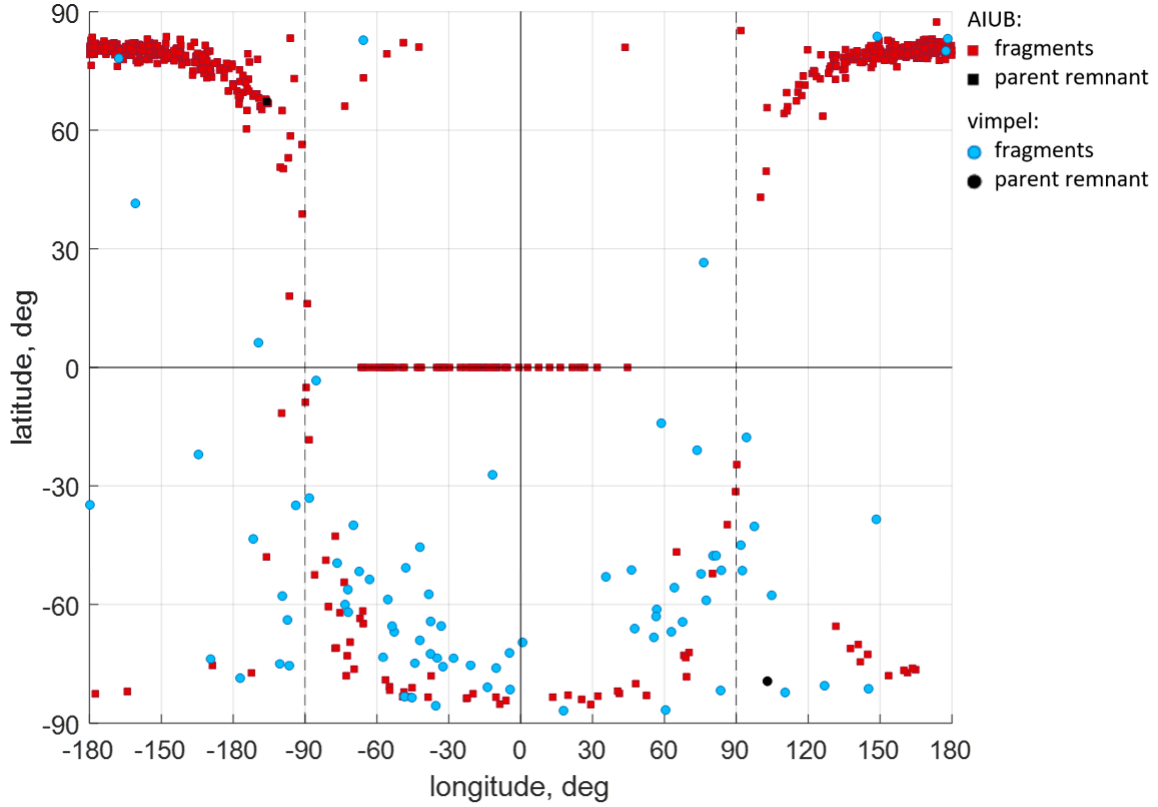
Figure 6.17. Event 1 (2009-047B), Angular distribution of fragments.

6.6.2 Event 2 (2014-055B)

Figure 6.18 shows the angular distributions of the fragments for Event 2. Interestingly, the AIUB and Vimpel distributions are quite incongruous. The AIUB fragments cover roughly two-thirds of the eastern hemisphere of the spherical projection; the parent remnant is roughly in the middle of the cluster. The Vimpel fragments appear to form a vertically oriented torus; the parent remnant is similarly surrounded by other fragments. Not much information can be gleaned from the Spacetrack fragments due to the relatively few 'usable' fragments that had determinable perturbations; these fragments are quite spread out and do not form a noticeable pattern. The Vimpel fragments are in alignment with the Half-Segment model 4.10; this is characterized by ruptures at two opposite locations. The two ruptures may exist at low latitudes along the -90 and + 90 longitude regions (about the western and eastern sides of the spherical projection) – this would result in the debris being ejected upwards and downwards to form the ring-like distribution that is observed. This

105

bears resemblance to the Spot-1 event, which had a diagonal ring of fragments around the spherical projection as seen in Figure 5.12. On the other hand, the AIUB fragments are evocative of the Clam model, pointing towards the presence of one rupture point. The location of this rupture would face the region diametrically opposite to the fragment cluster, which is largely devoid of fragments – coincidentally, this would align with the left rupture location (low latitude near -90 longitude) pertaining to the Vimpel fragments.
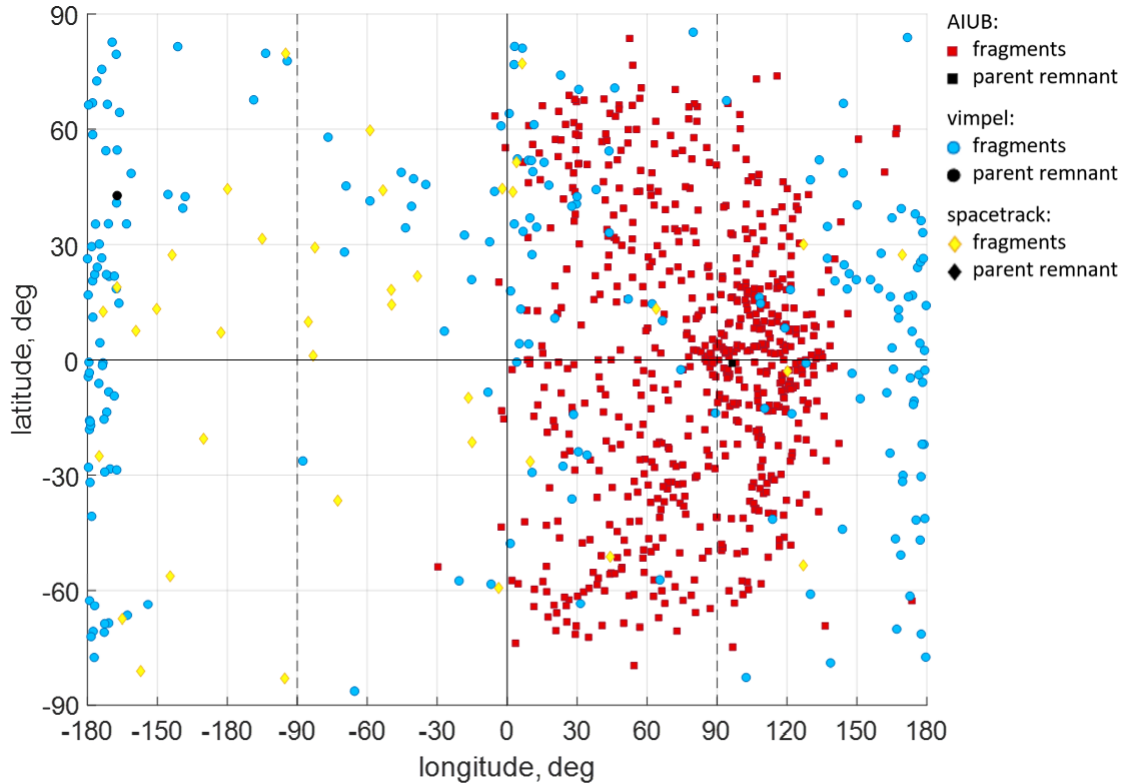

Figure 6.18. Event 2 (2014-055B), Angular distribution of fragments.

6.6.3   Event 3 (2018-079B)

The angular distributions of the fragments of Event 3 in 6.19 show no indication of a singular cluster (Clam model) or the Half-Segment model. The AIUB fragments, for instance, form various clusters indicating the presence of multiple rupture locations. An Octant model, characterized by multiple, roughly equally-spaced rupture locations, (Figure 4.10) may be applicable here. However, since the fragments are not quite evenly spread, this could be a variation of the Octant model with asymmetric ruptures. It is difficult to discern noticeable
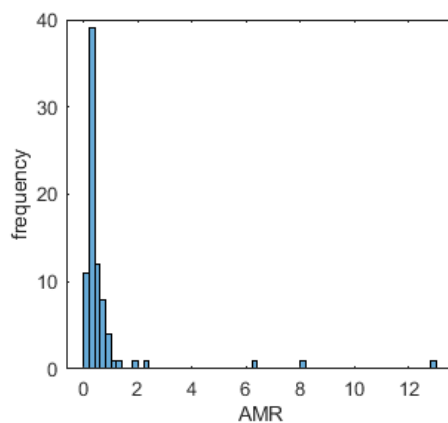
patterns from the Vimpel and Spacetrack fragments; however, random dispersal of fragments is also characteristic of the Octant model.
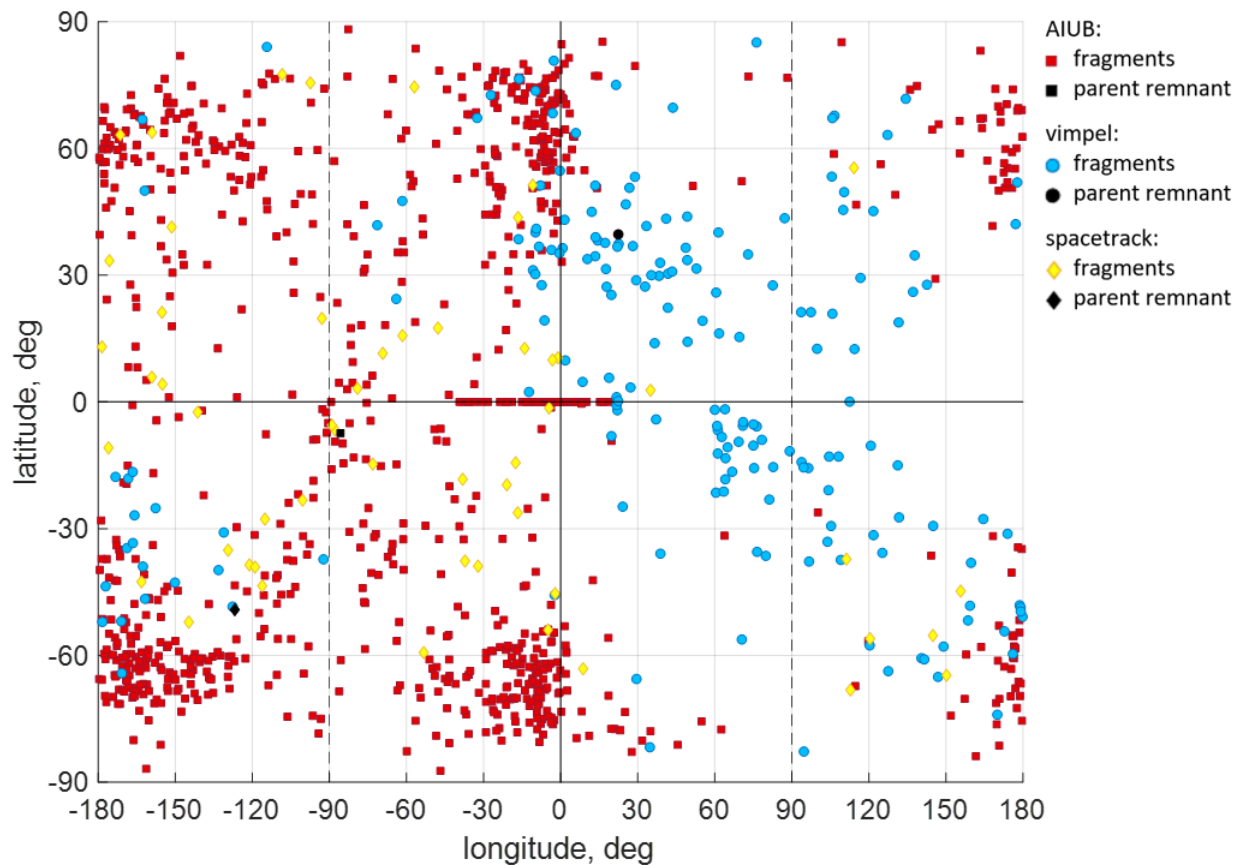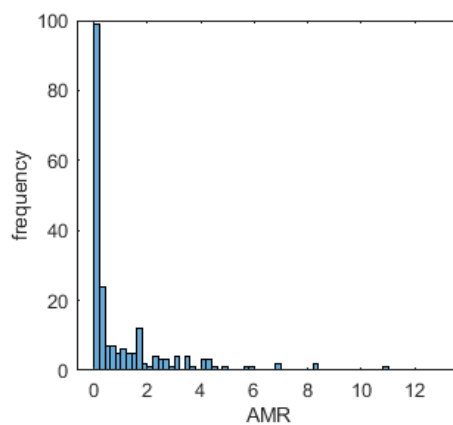

Figure 6.19. Event 3 (2018-079B), Angular distribution of fragments.
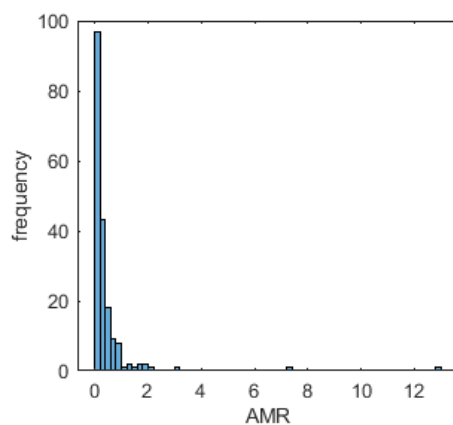
6.7 Area-to-Mass Ratio

The Area-to-Mass Ratio (AMR) is obtained from the Vimpel catalog and AMR frequencies for the three events are shown in Figure 6.20.

(a) Event 1 (2009-047B), AMR frequencies of fragments.

(b) Event 2 (2014-055B), AMR frequencies of fragments.

(c) Event 3 (2018-079B), AMR frequencies of fragments.

Figure 6.20. AMR frequency distributions of the Centaur upper stage events.

From the AMR plots, it is evident that most of the fragments for Events 2 and 3 have AMR lower than 0.2 (m²/kg). Fragments such as these, with low AMR, are typically made of higher density materials such as steel, titanium, or dense aluminium alloys [16]. Most of the fragments of Event 1 possess a slightly higher AMR in the 0.2-0.4 range. This could point towards lower-density materials such as electrical components and aluminium alloys. These outcomes are in alignment with the Centaur's construction – the Centaur upper stage uses stainless steel walled propellant tanks. The pressurization system comprises graphite/epoxy composite materials and aluminium lining materials. The combustion chamber in the RL-10A-4-2 engine is also made of stainless steel [44]. Event 2 fragments show a larger AMR range, indicating quite a few fragments are made of lower-density materials similar to carbon composites, multi-layer insulation, or solar panel fragments.

6.8 Event Intensities

Higher intensity events are likely to be caused by explosions (leftover propellant combustion, for instance) or collisions, while lower intensity events can be attributed to fragmentations due to drag effects and/or structural failure, or small battery explosions.
The intensities of the three events in m^2/s^2 are shown in Table 6.4.

Table 6.4. Intensities of the Centaur upper stage and select historic events

Event	AIUB	Vimpel	Spacetrack
Event 1 (2009-047B)	5950	19	-
Event 2 (2014-055B)	20673	2836	2555
Event 3 (2018-079B)	55905	1513	8170
NOAA-3	-	-	5807
Landsat-1	-	-	3660
Nimbus-6	-	-	45207
Spot-1	-	-	1511

The intensities of the three Centaur upper stage events vary substantially based on the data source. This is likely due to the disparity in the number of fragments from each source

(this would skew averages), in addition to different propagation times, inevitably leading to accumulating uncertainties. Nevertheless, some patterns can be identified. Fragments stemming from Event 1 possess small velocities resulting in the lowest intensity of the three events. While both the AIUB and Spacetrack data point towards Event 3 having the highest intensity, the Vimpel data does not. Event 2 appears to have a mid-range intensity, with the average velocities of the Vimpel fragments in relatively close alignment with those of the Spacetrack fragments.

The Delta upper stage events (NOAA-3, Landsat-1, and Nimbus-6 events) and the Spot-1 event are also included for reference. All three of the Delta events were explosions due to leftover propellant combustion. The high intensity of the Nimbus-6 event is attributable to 245 kg of leftover propellant, compared to 130-150 kg for the other Delta events [4]. It is not known if any propellant was left in the Centaur tanks. Since the Centaur upper stage is about twice the size of the Delta upper stage, a Centaur explosion wold likely be very high in energy, perhaps akin to that of Event 3. The Spot-1 event is believed to have occurred due to a collision with debris and has a noticeably lower intensity. This is quite close to the intensities observed for Event 2 based on the Vimpel and Spacetrack data.

6.9 Fragmentation Hypotheses

There is no evidence of another sizeable, catalogued object (such as a satellite or upper stage) having a close encounter with any of the three parent objects at the breakup epoch. Ruling this out and considering the breakup characteristics for each event, some hypotheses can be made regarding their fragmentation causes.

6.9.1 Event 1 (2009-047B)

The relatively small velocity perturbations of the fragments and the closeness of fragments along the orbit point towards a considerably low-intensity event. As a result, this event is unlikely to be caused by collisions or explosions. The clustered angular distribution of the fragments points to the existence of a single rupture location, possibly a crack. This is likely

due to a structural failure of the Centaur body. Material fatigue may have led the upper stage to buckle under stress – such a breakup would result in the small fragment spreading speeds that are observed for this event. It is also possible that a low-speed collision involving a small object may have taken place – it may not have had sufficient energy to fully pierce the body, but could still cause a rupture. Regardless, for a low-intensity event, the massive production of 725 fragments (catalogued by AIUB) is absurd.

6.9.2 Event 2 (2014-055B)

Depending on the data source, one can conclude that there are either one (indicated by AIUB data) or two (indicated by Vimpel data) rupture locations. The intensity of the event (based on the Vimpel and Spacetrack fragments) is relatively similar to the Spot-1 event, which is believed to have been caused by a collision with small debris. The AIUB fragments for this event encountered unusually strong cross-range velocity perturbations, which could be indicative of such a collision, resulting in out-of-plane motion. Thus, it is possible that a small piece of debris may have pierced through the Centaur body.

6.9.3 Event 3 (2018-079B)

The isotropic spread of fragment velocities, high event intensity, and widely dispersed angular patterns of the fragments, all point towards an explosive fragmentation due to leftover propellant combustion. Unlike the Delta upper stage explosions, the fragments in this event spread in various directions but remained in identifiable clusters (as opposed to dispersing haphazardly in all directions). The distinct multidirectionally-dispersed cluster patterns of the AIUB fragments suggest this may be an anomalous propellant tank explosion that is a variation of the Octant model – it is likely there were fewer rupture locations than in the Delta events. However, these were still equally spaced to result in the symmetric fragment distribution (of the AIUB fragments) that is observed.

6.10 Uncertainty Considerations

The presented Centaur results do not account for any uncertainties in the data used. Uncertainties in optical measurements directly affect the initial state vector of an object. While parameters such as mean motion can be estimated from measurements relatively quickly with confidence, it can often take monitoring multiple revolutions of an object to ascertain key orbital elements (such as semimajor axis and eccentricity) within an acceptable confidence level. Since the velocity perturbations and angular perturbations are functions of these orbital elements, any uncertainty in the initial observation/ephemeris states directly affects the modeled fragment dispersions. For instance, a position uncertainty along the range direction to an object – often unavoidable when optical measurments are obtained from a similar true anomaly (for example, when the object is at its apogee) – will affect the computation of the semimajor axis. A higher semimajor axis generally corresponds to a larger downrange velocity perturbation; if the measurements are thus skewed such that the range to an object is always overestimated, the results may be populated with fragments possessing high downrange velocities. Uncertainties in optical measurements will naturally vary across different sensor networks, affecting data catalogued by AIUB, Vimpel, and USSTRATCOM to varying levels. Additionally, errors that may accumulate over the course of propagating the initial states to desired epochs will also result in inaccuracies in the final state of the objects. Discrepancies arising from different propagators (SGP4 vs numerical) are covered in Section 3.4.

It is assumed that these uncertainties do not play a significant role in the outcomes of this research. Uncertainties in optical measurements generally affect all objects catalogued by a source to the same extent (assuming the objects are in fairly similar orbits). Propagation errors – particularly apparent when using SGP4 – are also extended to all objects. Since this work is concerned with the motion of fragments relative to a parent object, the accuracy of their final states is of less importance than their relative distributions. Even if the states of the objects calculated at the breakup epoch are not entirely accurate, the fragment distributions still yield meaningful patterns and breakup characteristics which are advantageous in identifying event causes. However, since each data source and propagator

has a different impact on the fragment uncertainties, one would still have to investigate the fragments separately (AIUB, Vimpel, Spacetrack), and acknowledge that these differences directly contribute to the disparity in results that is observed for the Centaur events.

7. SUMMARY

7.1 Conclusions

In order to mitigate the exponential growth of the debris population in orbit, it is essential to investigate debris-generating events and identify their causes. This work is concerned with analyzing three particularly puzzling fragmentation events: the Centaur upper stages, 2009-047B (Event 1), 2014-055B (Event 2), and 2018-079B (Event 3), which fragmented in 2018-2019. These events are not immediately evocative of prior fragmentation events in terms of both energy expended and fragment distribution – a closer inspection of the breakup characteristics and fragment properties is warranted and thus carried out in this work. The algorithms used to calculate the various breakup properties are validated using historic, well-studied fragmentation events, and the obtained results are in alignment with those in [4].

The first step of any fragmentation investigation is the breakup epoch determination. The orbits of the fragments (and parent object, if known), are propagated backwards to an epoch when they are at their closest. In the course of this research, both orbital and linear distance formulations are attempted, in cases employing the parent object and those without. It becomes evident that linear distance formulations consistently outperform their orbital counterparts; a breakup time that is in accordance with documented literature is always obtained. Including the parent object in the breakup epoch search and measuring fragment distances relative to it is also found to yield more accurate results. It is vital that a global minimum (rather than a local minimum) is obtained; this involves the usage of small time steps and may result in long computation times for large data sets.

If the parent object is not known, it can be determined by scanning the public two-line element catalog at the breakup epoch for parent candidates and filtering them by how closely their orbital elements match those of the fragments. In some cases, even if the filter limits are relatively narrow, more than one cataloged object is filtered; in this case it might be useful to consider the object type/material and assess its similarity to the area-to-mass

114

ratios of the fragments, if known. Once the breakup epoch is obtained, one can propagate the two-line elements or ephemerides of the fragments to this time and obtain significant insights – velocity perturbations imparted on the fragments and their directionalities can be calculated. These are indicative of both the energy of an event, as well as the manner in which it unfolded. Additionally, a Gabbard Diagram (plot of apogee and perigee heights versus orbital period) can be constructed – the velocity magnitudes and angular dispersions of fragments can often be preliminarily inferred from this plot, making it an indispensible tool to gather initial insights surrounding an event. If available, the area-to-mass ratio of the fragments may also provide additional information regarding material properties. Coupled, these characteristics pertaining to an event can provide crucial information surrounding its cause. This work does not account for uncertainties in the initial state vector of an object; since this research is concerned with the relative motion of fragments to the parent object, the effect of uncertainties is assumed to similarly impact all objects, playing an insignificant role in the relative fragment distributions. However, it is worth noting that downrange velocities of the objects are likely disproportionately affected by uncertainties in range estimates from the optical measurements.

Upon applying these techniques to the Centaur events and comparing the outcomes to historic fragmentations, cases in support of different hypotheses are steadily built for each event: Event 1 (2009-047B), with unusually small fragment velocities and clustered fragments, likely stemmed from a single rupture point. The streak-like distribution of fragments indicates that the rupture could have been in the form of a crack, which ultimately fractured the body. Apart from structural failure in this manner, it is also possible that a low-energy collision with debris took place. On the other hand, Event 2 (2014-055B) had a larger intensity, with angular distributions of the fragments indicating up to two rupture locations. This supports a hypothesis that the Centaur body may have been hit by debris which pierced through the body. The intensity of this event is also similar to that of the Spot-1 event, which is believed to have suffered the same fate. Event 3 (2108-079B) had a considerably higher intensity than both Events 1 and 2 (as well as the Delta upper stage and Spot-1 events).

Given the high-velocity isotropic fragment distribution that is observed, it is probable that a propulsion-related event took place, resulting in a high-energy explosion.

7.2   Recommendations and Future Work

This thesis provides a detailed insight into fragmentation theory and how it can be used to extract relevant breakup characteristics surrounding an event. While this work specifically analyzes a handful of events (Centaur and Delta upper-stages, and Spot-1), the methodology can be swiftly applied to any fragmentation events of interest as long as fragment two-line element sets or ephemerides are available. Fragment distributions and energies in the immediate aftermath of various events can be found – upon comparing these to properties of previously-documented events, conclusions regarding their causes can be made. While these insights can provide a valuable starting point, there is room for additional analysis.

The presented work only scratches the surface of area-to-mass ratio (AMR) analyses. AMR can provide valuable insights into the material and relative masses of the fragments stemming from an event. It would be interesting to see patterns in AMR in conjunction with fragment velocities and angular perturbations; telling insights could be obtained if AMR objects of a certain value received noticeably high or low velocity perturbations and/or lie in a similar section of the angular projection. Unfortunately, AMR information can be difficult to obtain with accuracy, especially for objects that are difficult to track. It might also be worthwhile to carry out further statistical analysis on the correlation between the velocity and angular perturbations. While general trends are known (fragments near rupture points tend to have the highest velocities), it would be beneficial to observe if broader dependencies between the two exist. This may be particularly beneficial if rupture locations cannot be pinpointed solely from the angular projection of the fragments; identifying if high/low velocity fragments gather within a certain dispersion angle may be beneficial. Furthermore, the effects of the largest remnant following an event can be studied in more detail. The correlation between its motion, relative to other, perhaps higher AMR fragments may prove to be insightful. Additionally, incorporating higher order spherical harmonic perturbations terms will minimize errors in propagation. In this work, only the J2 term, which accounts

for the Earth's oblateness, is factored in to minimize computation time. Furthermore, the effect of uncertainty in optical measurements can be investigated in greater detail – it would be worthwhile to examine how uncertainties in the initial state vector of an object affect the fragmentation outcomes.

Deducing the causes of fragmentations is currently far from a perfect science. While fragmentation hypotheses can be arrived at, they are often difficult to confirm. Isotropic explosions due to leftover propellant and large collisions involving cataloged objects can generally be traced; however, more anomalous lower energy events, involving collision with debris or implosions, can be more elusive. It is likely that events involving difficult-to-detect, uncatalogued objects will eventually drive the long-term evolution of the space debris environment and are certain to require considerable scrutiny in the coming years.

REFERENCES

[1] *Space debris by the numbers*, Apr. 2021. [Online]. Available: http://www.esa.int/Safety_Security/Space_Debris/Space_debris_by_the_numbers.

[2] D. J. Kessler and B. G. Cour-Palais, "Collision frequency of artificial satellites: The creation of a debris belt," *Journal of Geophysical Research*, vol. 83, no. A6, 1978. DOI: 10.1029/ja083ia06p02637.

[3] *ESA's annual space environment report*, 2020. [Online]. Available: https://www.sdo.esoc.esa.int/environment_report/Space_Environment_Report_latest.pdf.

[4] A. Tan and R. C. Reynolds, *Theory of Satellite Fragmentation in Orbit*. World Scientific, 2020, ISBN: 9789811208553.

[5] V. Chobotov, D. Spencer, D. Schmitt, R. Gupta, R. Hopkins, and D. Knapp, "Dynamics of debris motion and the collision hazard to spacecraft resulting from an orbital breakup," *The Aerospace Corporation*, 1988.

[6] D. Kessler and J. Loftus, "Orbital debris as an energy management problem," *Advances in Space Research*, vol. 16, no. 11, pp. 139–144, 1995. DOI: 10.1016/0273-1177(95)98764-f.

[7] G. D. Badhwar and P. D. Anz-Meador, "Determination of the area and mass distribution of orbital debris fragments," *Earth, Moon and Planets*, vol. 45, no. 1, pp. 29–51, 1989. DOI: 10.1007/bf00054659.

[8] R. Jehn, "Dispersion of debris cloud from in-orbit fragmentation events," Sep. 1990.

[9] L. Healy, B. Halpin, S. Kindl, B. Hoskins, and C. Binz, "Initial velocity distribution and consequent spatial distribution of fragments," in *First International Orbital Debris Conference*. 2019.

[10] Z. Slatton and D. McKissock, "Methods of predicting and processing breakups of space objects," in *7th European Conference on Space Debris*. 2017.

[11] L. Dimare, S. Cicalo, A. Rossi, E. M. Alessi, and G. B. Valsecchi, "In-orbit fragmentation characterization and parent bodies identification by means of orbital distances," in *First International Orbital Debris Conference (2019)*. 2019.

[12] M. Romano, A. Muciaccia, M. Trisolini, P. D. Lizia, C. Colombo, A. D. Cecco, and L. Salotti, "PUZZLE software for the characterisation of in-orbit fragmentations," in *8th European Conference on Space Debris*. 2021.

[13] F. Hoots and M. Sorge, "Satellite breakup parameter determination," *The Journal of the Astronautical Sciences*, vol. 59, no. 1-2, pp. 120–140, 2012. DOI: 10.1007/s40295-013-0009-2.

[14] S. Flegel, J. Bennett, M. Lachut, M. Möckel, and C. Smith, "An analysis of the 2016 Hitomi breakup event," *Earth, Planets and Space*, vol. 69, no. 1, 2017. DOI: 10.1186/s40623-017-0633-3.

[15] M. Sorge, G. Peterson, and M. J., "Forensic analysis of on-orbit debris generation events," in *7th European Conference on Space Debris*. 2017.

[16] G. Peterson, M. Sorge, and J. McVey, "Forensic analysis of debris-generating events: Orbcomm FM 16," in *First International Orbital Debris Conference*. 2019.

[17] V. Braun, A. Horstmann, S. Lemmens, C. Wiedemann, and L. Böttcher, "Recent developments in space debris environment modelling, verification and validation with master," in *8th European Conference on Space Debris*. 2021.

[18] H. Cowardin, J. Liou, P. Anz-Meador, M. Sorge, J. Opiela, N. Fitz-Coy, T. Huynh, and P. Krisko, "Characterization of orbital debris via hyper-velocity laboratory-based tests," in *7th European Conference on Space Debris*. 2017.

[19] E. Watson, N. Durr, and M. Schimmerohn, "Tracking debris cloud fragments: An experimental method for measuring hypervelocity fragmentation in the context of validating numerical simulations," in *8th European Conference on Space Debris*. 2021.

[20] E. Richardson, A. Jackson, M. Hays, M. Bangham, J. Blackwood, T. Skinner, and B. Richman, "An experimental study of launch vehicle propellant tank fragmentation," in *JANNAF Propulsion Systems Hazards Joint Subcommittee Meeting, Joint Army Navy NASA Air Force Interagency Propulsion Committee, M15-4295, Albuquerque, NM*, 2014.

[21] H. Curtis, *Orbital Mechanics for Engineering Students*. Elsevier Butterworth-Heinemann, 2005, ISBN: 0 7506 6169 0.

[22] D. A. Vallado, *Fundamentals of Astrodynamics and Applications, Fourth Edition*. Microcosm Press, 2013, ISBN: 978-1881883203.

[23] T. Kelso. (Dec. 28, 2019). "Space surveillance," [Online]. Available: https://celestrak.com/columns/v04n01/ (visited on 05/09/2021).

[24] (Jul. 2018). "U.S. strategic command fact sheet," [Online]. Available: https://www.stratcom.mil/Portals/8/Documents/CSpOC_Factsheet_2018.pdf (visited on 05/09/2021).

[25] T. Kelso. (Dec. 28, 2019). "Frequently asked questions: Two-line element set format," [Online]. Available: http://celestrak.com/columns/v04n03/ (visited on 05/09/2021).

[26] E. Olson. (May 13, 2017). "How tracking the international space station works," [Online]. Available: https://insights.globalspec.com/article/5084/how-tracking-the-international-space-station-works (visited on 05/09/2021).

[27] (). "JSC Vimpel - data portal," [Online]. Available: http://spacedata.vimpel.ru/ (visited on 05/09/2021).

[28] O. Montenbruck and E. Gill, *Satellite Orbits*. Springer, 2001, ISBN: 354067280X.

[29] C. Frueh, *Space Traffic Management*. Purdue University, 2019.

[30] F. Hoots, P. Schumacher, and R. Glover, "History of analytical orbit modeling in the U.S. space surveillance system," *Journal of Guidance, Control, and Dynamics*, vol. 27, 2 2004. DOI: https://doi.org/10.2514/1.9161.

[31] F. R. Hoots and R. L. Roehrich, *Spacetrack Report No. 3: Models for propagation of NORAD element sets*. Aerospace Defense Center, Peterson Air Force Base, 1980.

[32] R. Southworth and G. Hawkins, "Statistics of meteor streams," *Smithsonian Contributions to Astrophysics*, vol. 7, pp. 261–285, 1963.

[33] J. Drummond, "A test of comet and meteor shower associations," *Icarus*, vol. 45, pp. 545–553, 1981.

[34] T. Jopek, "Remarks on the meteor orbital similarity d-criterion," *Icarus*, vol. 106, pp. 603–607, 1993.

[35] T. Schildknecht, A. Vananti, and E. Cordelli, "ESA optical surveys to characterize recent fragmentation events in GEO and HEO," in *Advanced Maui Optical and Space Surveillance Technologies Conference (AMOS)*. 2019.

[36] G. Badhwar, A. Tan, and R. Reynolds, "Velocity perturbation distributions in the breakup of artificial satellites," *J. Spacecraft Rockets*, vol. 27, pp. 299–305, 1990.

[37] F. Benz, R. Kays, C. Bishop, and M. Eck, "Explosive fragmentation of orbiting propellant tanks," *American Institute of Aeronautics and Astronautics*, 1989.

[38] N. L. Johnson., E. Stansbery, D. Whitlock, K. Abercromby, and D. Shoots, *History of on-orbit satellite fragmentations 14th edition*. NASA, 2008.

[39] P. D. Anz-Meador, J. N. Opiela, D. Shoots, and J. Liou, "History of on-orbit satellite fragmentations 15th edition," *NASA/TM-2018-220037*, 2018.

[40] N. Johnson, "Preliminary analysis of the Spot 1 Ariane third stage," in *Orbital Debris from Upper Stage Breakup*, J. Loftus, Ed., Washington, DC: AIAA, 1989, pp. 41–100.

[41] B. G. Cour-Palais and J. L. Crews, "Hypervelocity impact and upper-stage breakups," in *Orbital Debris from Upper Stage Breakup*, J. Loftus, Ed., Washington, DC: AIAA, 1989, pp. 25–38.

[42] D. J. Kessler, "Current orbital debris environment," *Orbital Debris from Upper-Stage Breakup*, p. 3, 1989.

[43] P. Ravi, C. Frueh, and T. Schildknecht, "Investigation of three recent Atlas V Centaur upper stage fragmentation events," in *8th European Conference on Space Debris*. 2021.

[44] T. Rudman and K. Austad, "The Centaur upper stage vehicle," *4th IAC on Launcher Technology*, 2002.

[45] V. Agopov, "Major fragmentation of Atlas 5 Centaur upper stage 2014-055b (ssn #40209)," *IAA Space Debris Committee meeting*, 2018.

[46] V. Agopov and N. Savin, "Updated assessments of the fragmentations of Atlas 5 Centaur upper stages," *IAA Space Debris Committee meeting*, 2019.

[47] (Oct. 12, 2012). "Atlas V Centaur upper stage," [Online]. Available: https://www.nasa.gov/mission_pages/landsat/launch/gallery/2012-10-09-8.html (visited on 05/09/2021).

A. APPENDIX

Gabbard diagrams, along with velocity and angular perturbation plots for the Landsat-1 and Nimbus-6 events are provided in this section. They are presented alongside plots from [4], which were used to validate the algorithms implemented over the course of this research. Additionally, 2D velocity plots and the angular perturbations pertaining to 2014-055B (Centaur, Event 2) are shown with respect to a different breakup time.

A.1 Validation results: Landsat-1
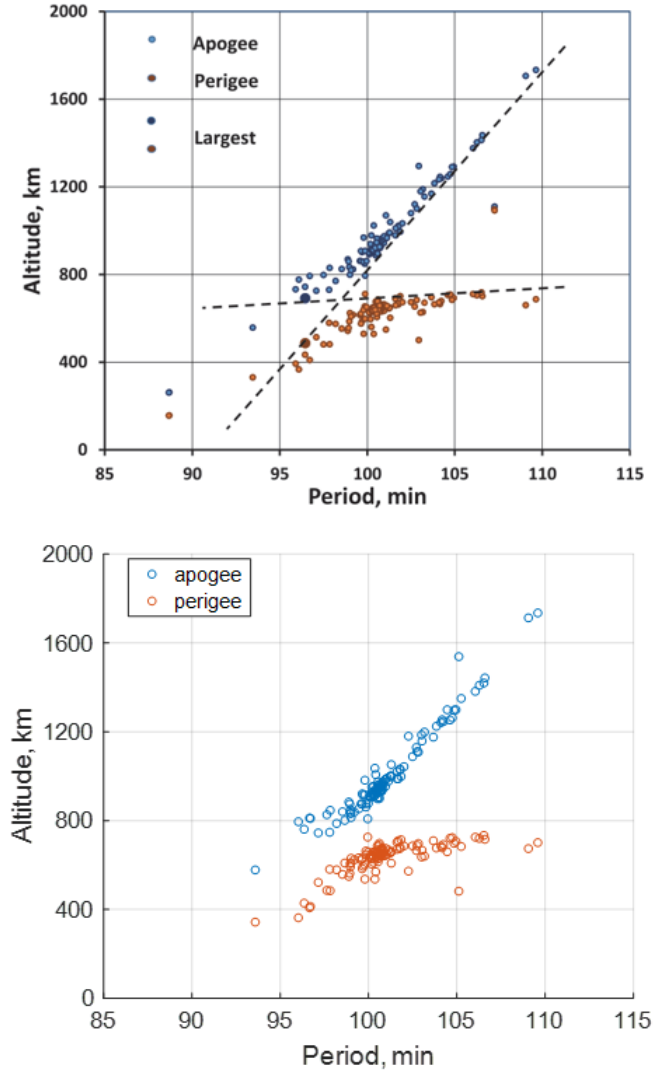
Figure A.1. Landsat-1: Gabbard diagram of fragments compared with [4] (top).
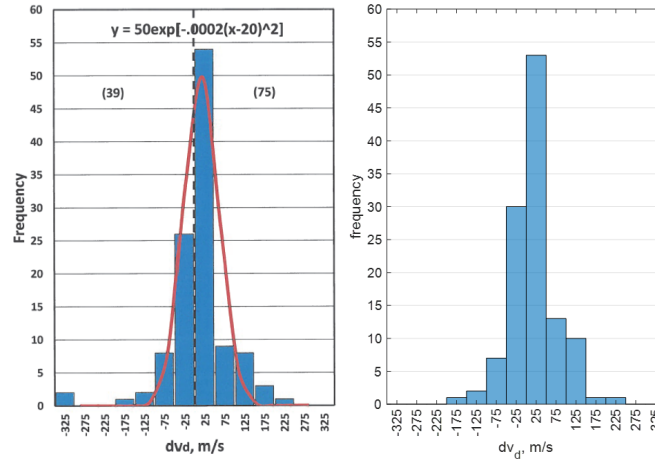
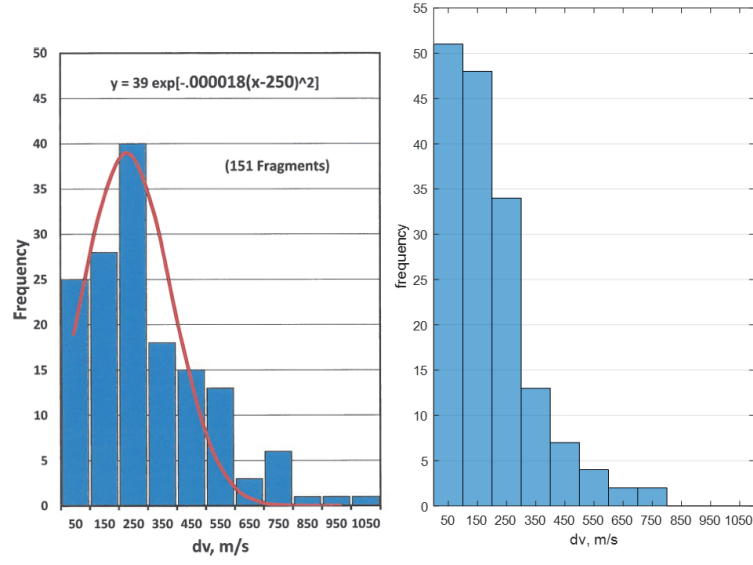(a) Landsat-1: Downrange velocities of fragments.
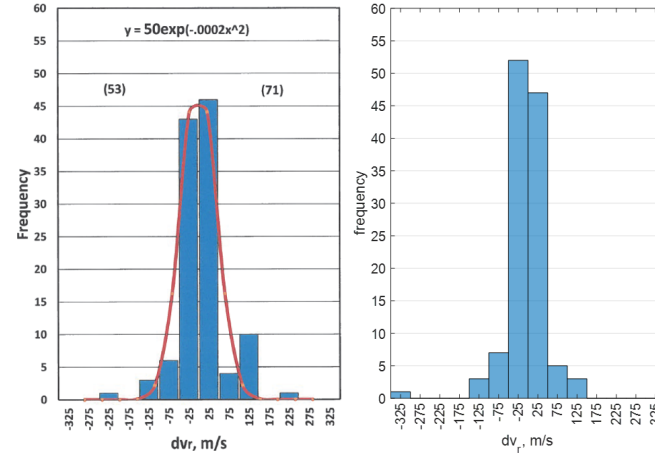
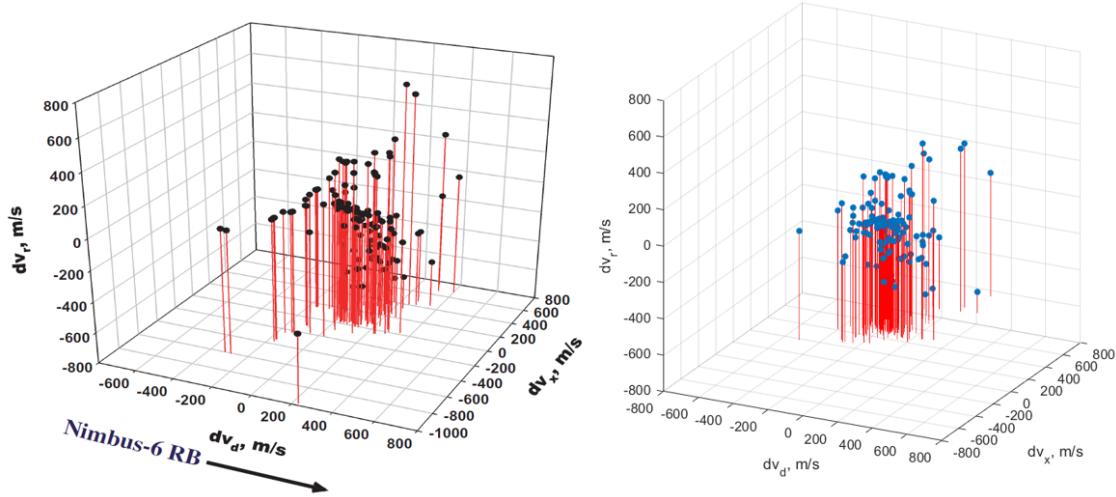

(b) Landsat-1: Radial velocities of fragments.
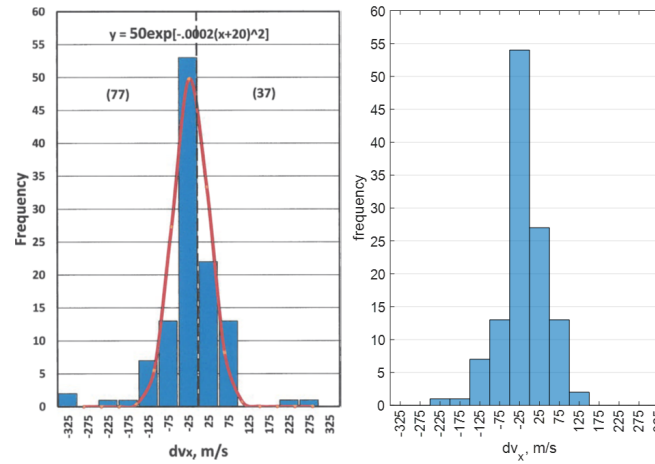
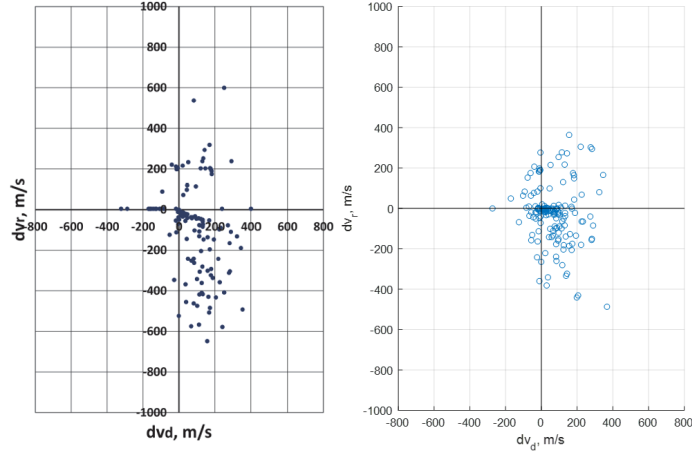(c) Landsat-1: Cross-range velocities of fragments.

Figure A.2. Landsat-1: Velocity frequencies of fragments compared with [4] (left).
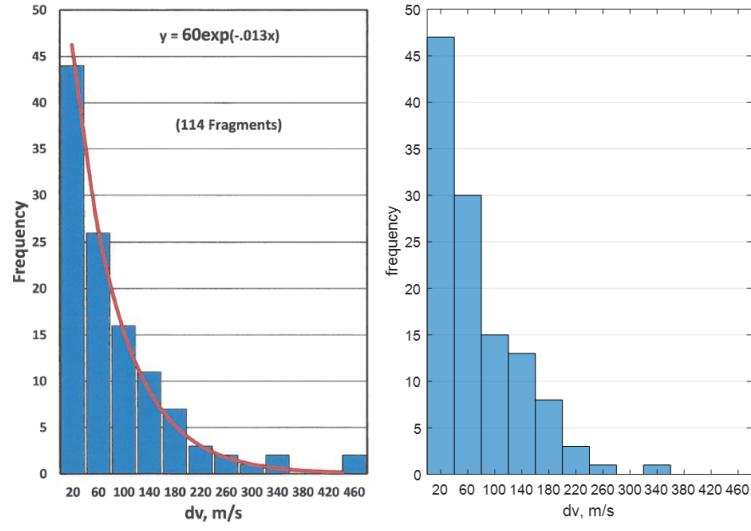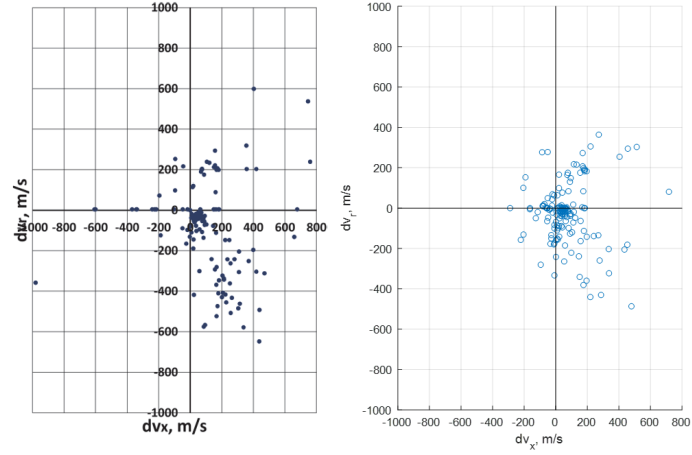
Figure A.3. Landsat-1: Total velocity perturbations of fragments compared with [4] (left).
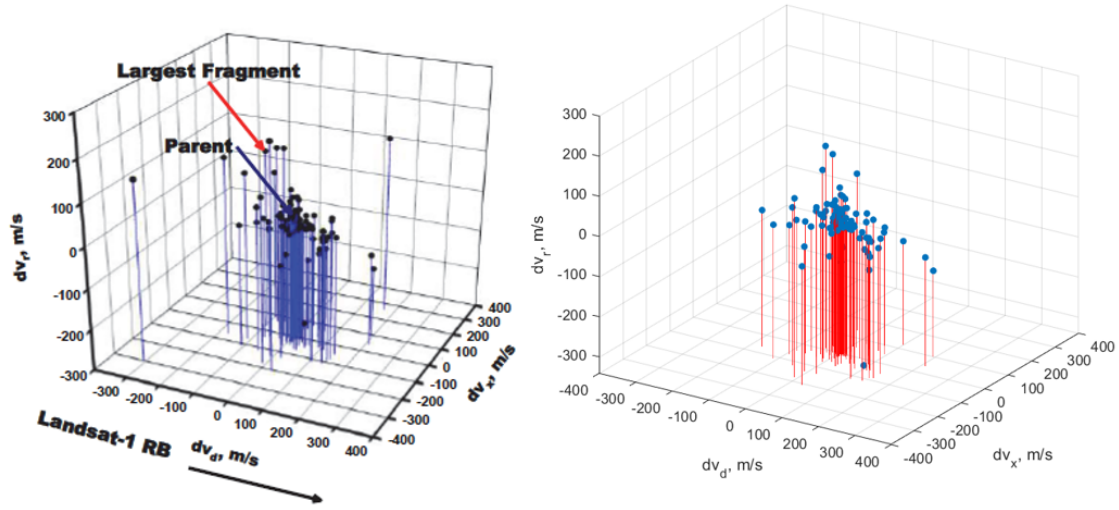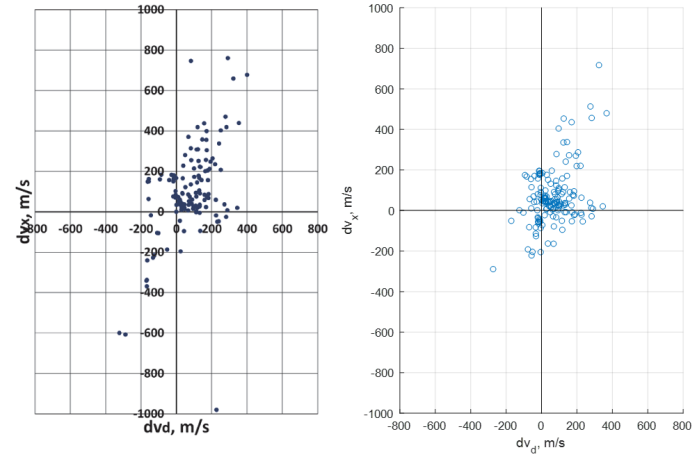

Figure A.4. Landsat-1: 3D velocity distributions of fragments compared with [4] (left).
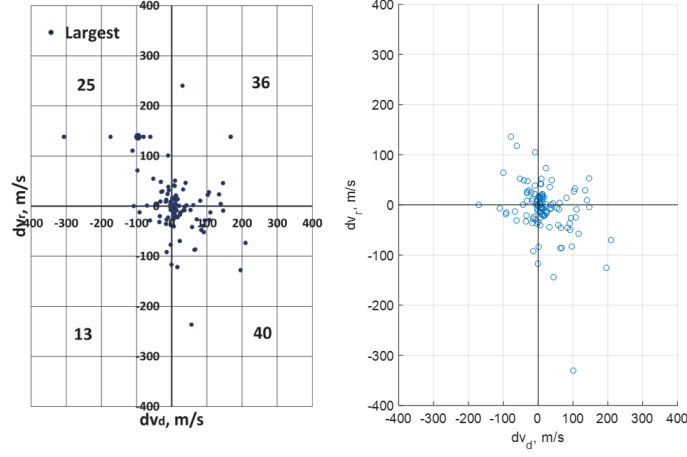
(a) Landsat-1: 2D plot of radial vs. downrange velocities of fragments.
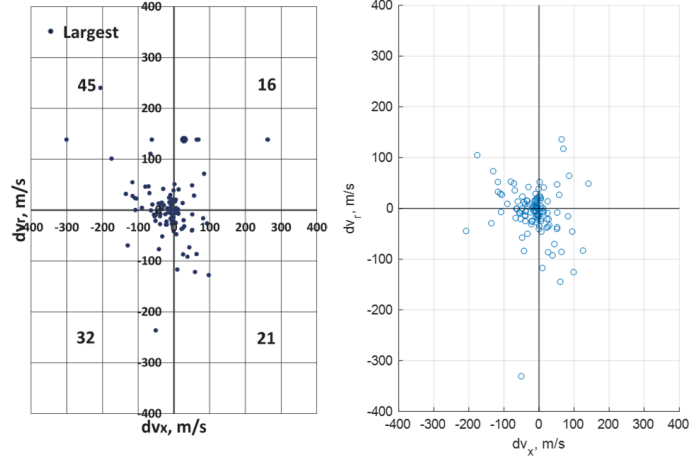
(b) Landsat-1: 2D plot of cross-range vs. radial velocities of fragments.
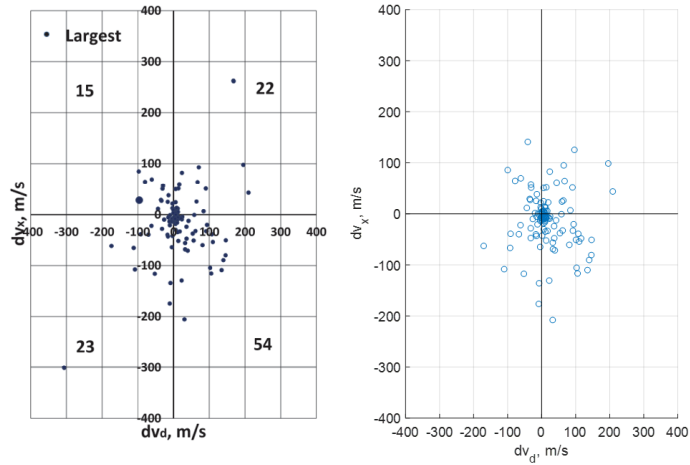
(c) Landsat-1: 2D plot of cross-range vs. downrange velocities of fragments.

Figure A.5. Landsat-1: 2D velocity distributions of fragments compared with [4] (left).

125
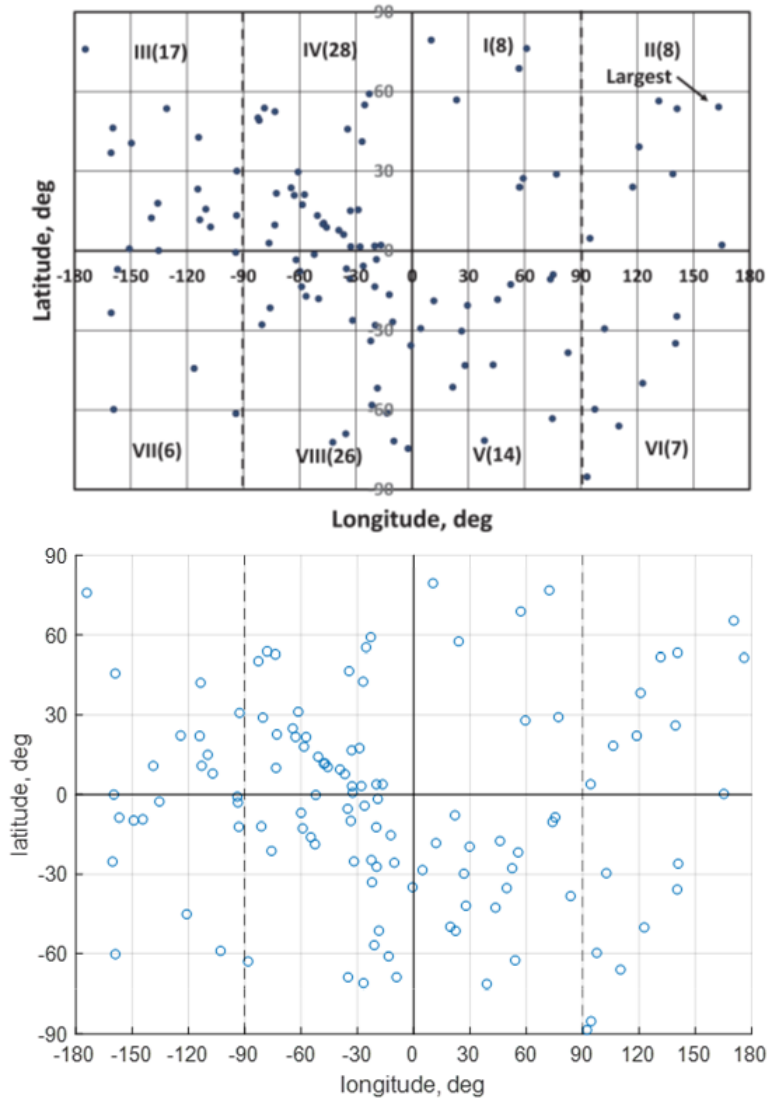
Figure A.6. Landsat-1: Angular distribution of fragments compared to [4] (top).

A.2 Validation results: Nimbus-6
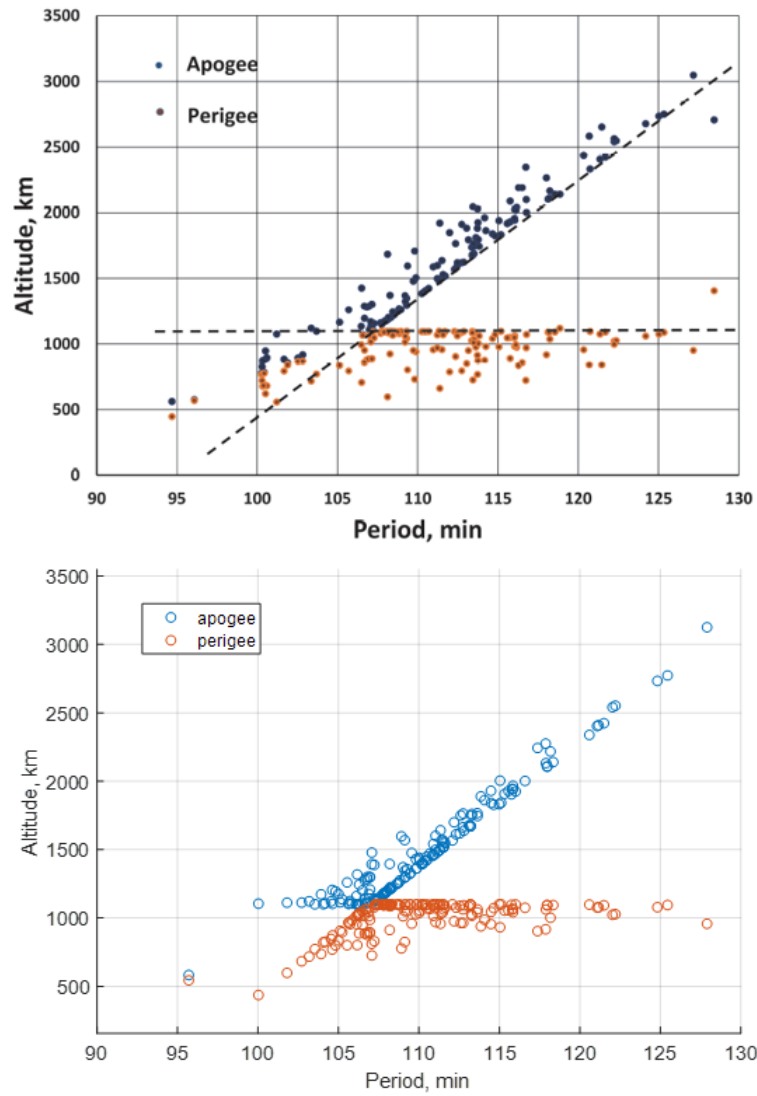
Figure A.7. Nimbus-6: Gabbard diagram of fragments compared with [4] (top).
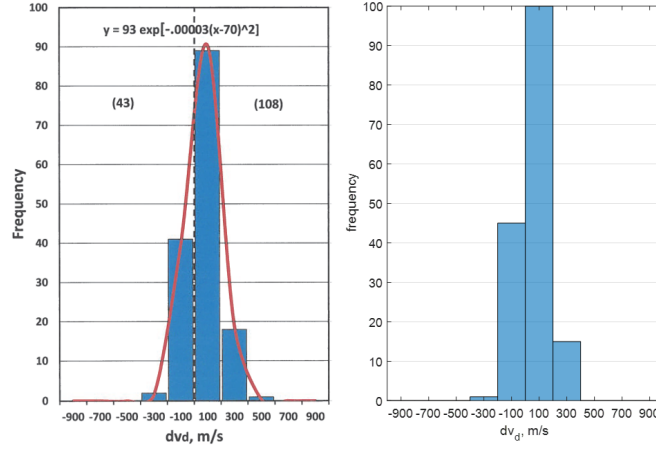
(a) Nimbus-6: Downrange velocities of fragments.
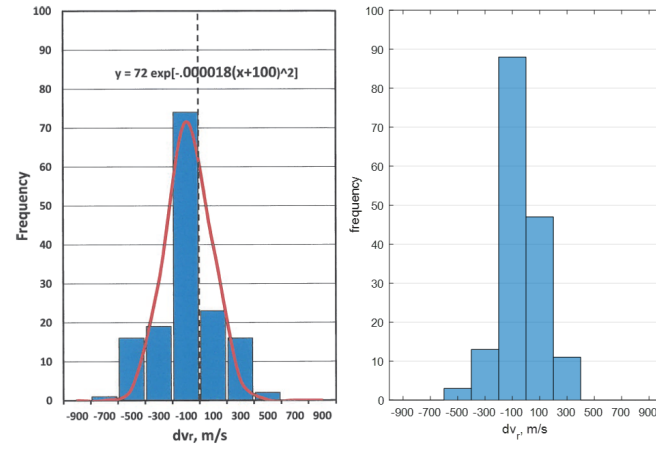
(b) Nimbus-6: Radial velocities of fragments.
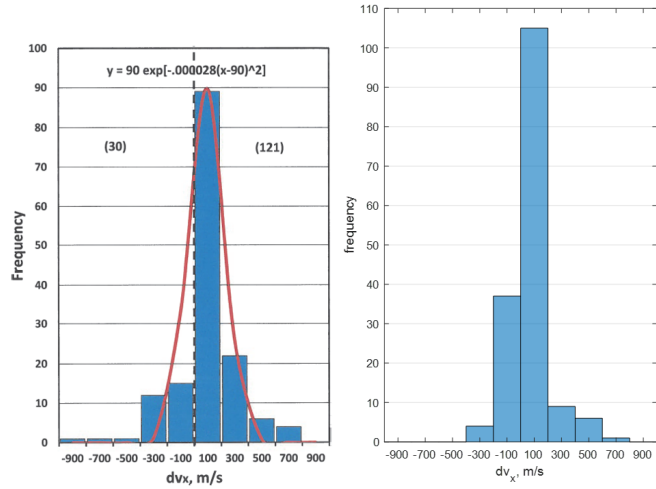
(c) Nimbus-6: Cross-range velocities of fragments.

Figure A.8. Nimbus-6: Velocity frequencies of fragments compared with [4] (left).

Figure A.9. Nimbus-6: Total velocity perturbations of fragments compared with [4] (left).

Figure A.10. Nimbus-6: 3D velocity distributions of fragments compared with [4] (left).

(a) Nimbus-6: 2D plot of radial vs. downrange veloci-
ties of fragments.

(b) Nimbus-6: 2D plot of radial vs. cross-range veloc-
ities of fragments.

(c) Nimbus-6: 2D plot of cross-range vs. downrange
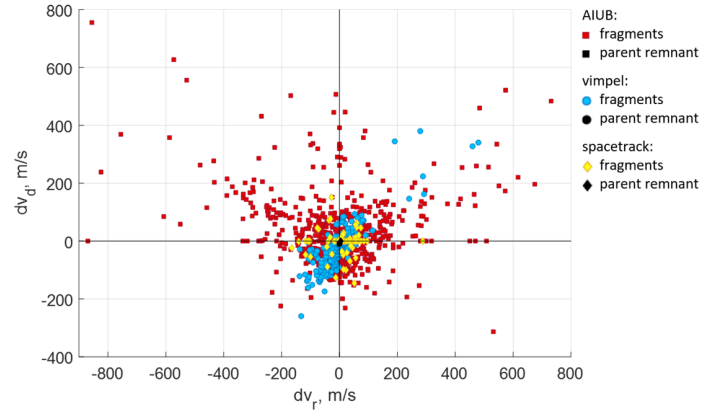velocities of fragments.

Figure A.11. Nimbus-6: 2D velocity distributions of fragments compared with [4] (left).

130
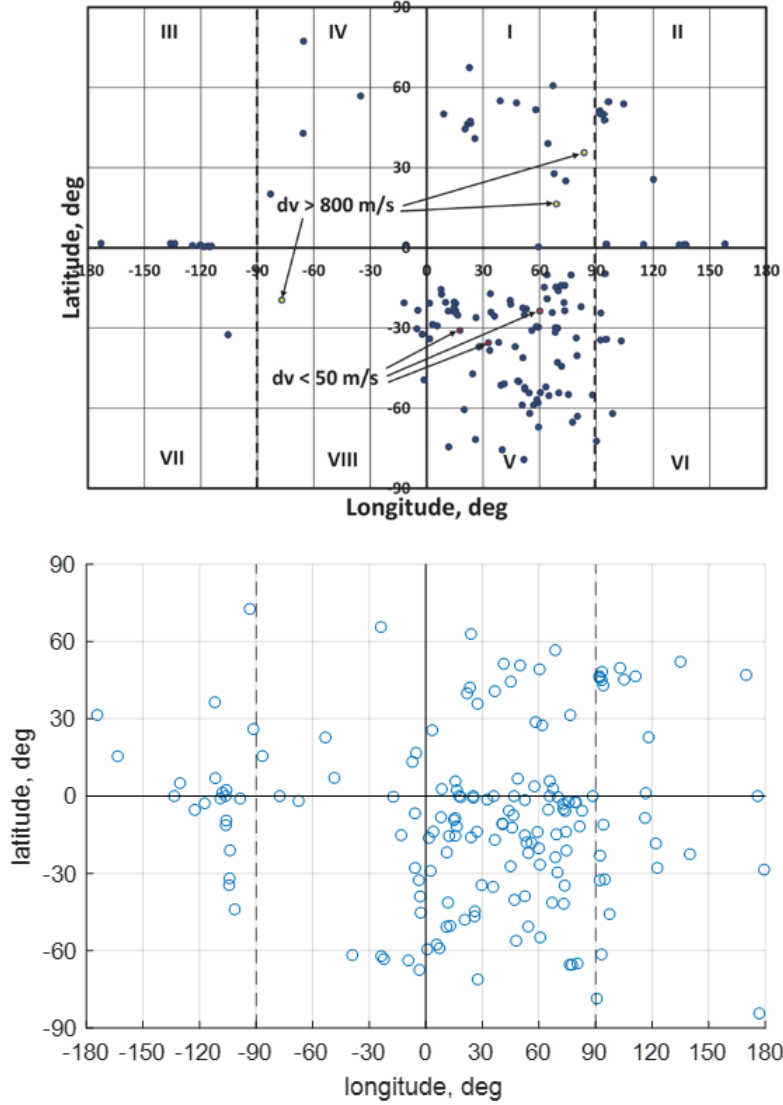
Figure A.12. Nimbus-6: Angular distribution of fragments compared to [4] (top).

A.3   2014-055B Results – Alternate Breakup Epoch

The 2D velocity plots and angular perturbations pertaining to 2014-055B at an hour past its breakup epoch (23:04, 30th Aug 2018) are shown in this section. These can be compared to Figures 6.11 and 6.18. The Vimpel fragments are affected to a greater degree, but still yield the same general patterns as observed for a breakup time of 22:04.

131

(a) Event 2: 2D plot of downrange vs. radial velocities of fragments.
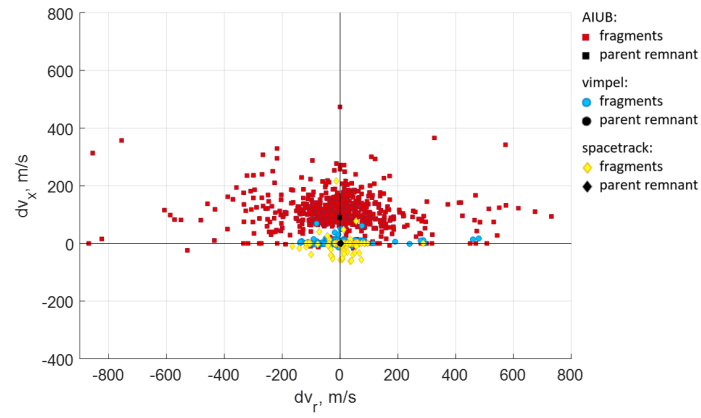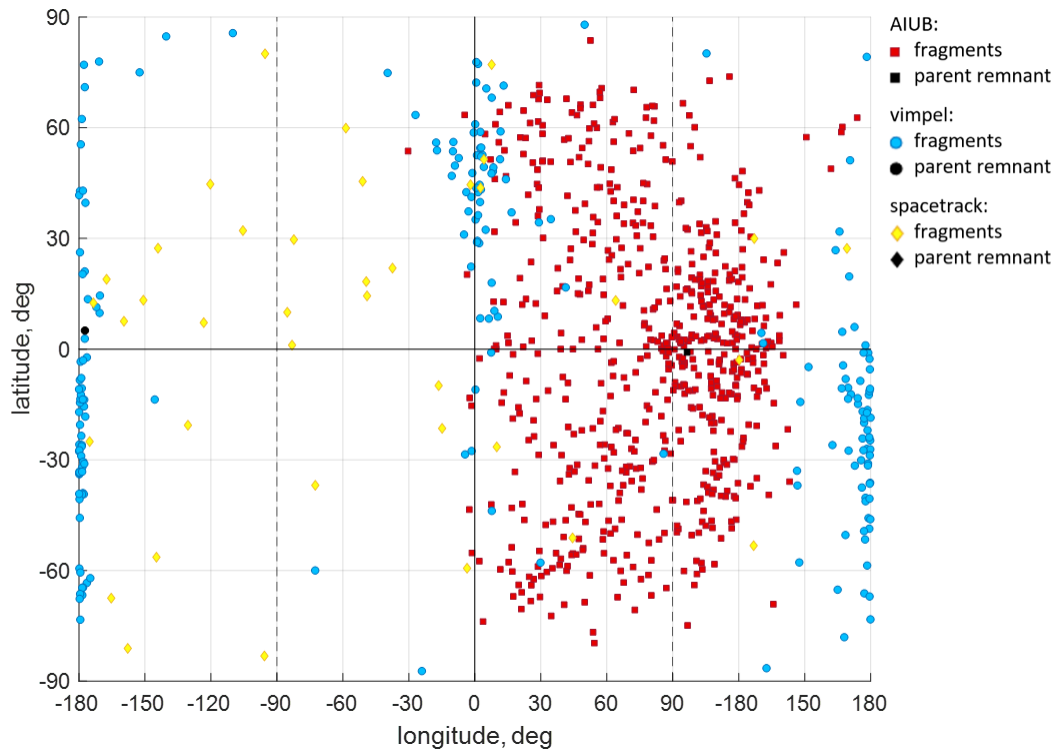

(b) Event 2: 2D plot of cross-range vs. radial velocities of fragments.
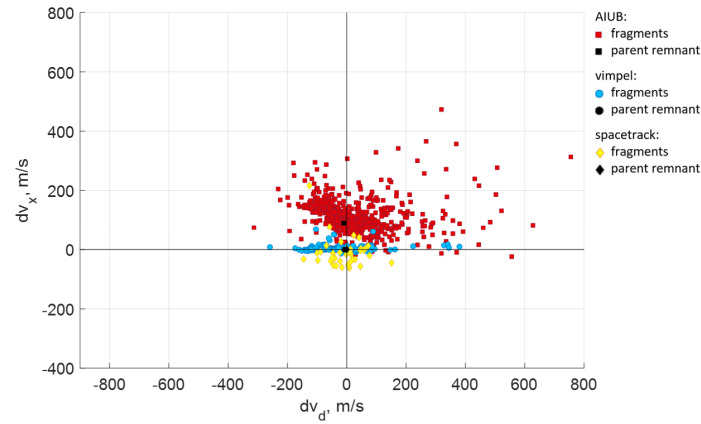
(c) Event 2: 2D plot of cross-range vs. downrange velocities of fragments.

Figure A.13. Event 2: 2D velocity distributions of fragments one hour past breakup epoch.

Figure A.14. Event 2: Angular distribution of fragments one hour past breakup epoch.